IMAGE: A MAP OF THE STARS OF THE ORION CONSTELLATION

Print ISSN: 2631-8490 Online ISSN: 2631-8504

JournalPreview

London Journal of Research in Science: Natural & Formal

Volume 25 | Issue 13 | Compilation 1.0

Great Britain Journals Press

WWW.JOURNALSPRESS.COM

Journal Content
In this Issue

Great Britain Journals Press

Equations of Unification: Mathematical Connections between Ramanujan's Recurring Numbers and Theoretical Cosmology

Dr. Michele Nardelli

Scienze della Terra Università

ABSTRACT

The search for a conceptual unity between the domains of discrete mathematics and continuous physics represents one of the deepest and most strategic challenges of modern science. Overcoming the dichotomy between the quantized world of numbers and the fluidity of spacetime is fundamental to develop a theoretical framework that can describe the universe in its entirety. The exploration of bridges between these two seemingly distant languages is not only an exercise in formal elegance, but a necessity to solve the enigmas that lie at the frontier of theoretical physics, from quantum gravity to the nature of the cosmological vacuum.

This paper presents a further development of the Nardelli Master Equation, unveiling its profound mathematical and symbolic connections to Ramanujan's Recurring Numbers. Through a multidisciplinary lens, we explore how this equation acts as a bridge between discrete number-theoretic phenomena and continuous geometric structures, revealing hidden symmetries across Geometric Measure Theory, Number Theory, Theoretical Cosmology, and String Theory. The recurrence patterns inspired by Ramanujan are shown to resonate with fractal geometries and cosmological constants, suggesting a unified framework where arithmetic intuition meets the fabric of spacetime.

Keywords: number theory, string theory, theoretical cosmology, supersymmetry, theory of everything, geometric measure theory.

Classification: LCC Code: QA241, QC20.7.G46, QB981

Language: English

Great Britain Journals Press

LJP Copyright ID: 925613
Print ISSN: 2631-8490
Online ISSN: 2631-8504

London Journal of Research in Science: Natural & Formal

Volume 25 | Issue 13 | Compilation 1.0

Equations of Unification: Mathematical Connections between Ramanujan's Recurring Numbers and Theoretical Cosmology

Dr. Michele Nardelli

ABSTRACT

The search for a conceptual unity between the domains of discrete mathematics and continuous physics represents one of the deepest and most strategic challenges of modern science. Overcoming the dichotomy between the quantized world of numbers and the fluidity of spacetime is fundamental to develop a theoretical framework that can describe the universe in its entirety. The exploration of bridges between these two seemingly distant languages is not only an exercise in formal elegance, but a necessity to solve the enigmas that lie at the frontier of theoretical physics, from quantum gravity to the nature of the cosmological vacuum.

This paper presents a further development of the Nardelli Master Equation, unveiling its profound mathematical and symbolic connections to Ramanujan's Recurring Numbers. Through a multidisciplinary lens, we explore how this equation acts as a bridge between discrete number-theoretic phenomena and continuous geometric structures, revealing hidden symmetries across Geometric Measure Theory, Number Theory, Theoretical Cosmology, and String Theory. The recurrence patterns inspired by Ramanujan are shown to resonate with fractal geometries and cosmological constants, suggesting a unified framework where arithmetic intuition meets the fabric of spacetime. We propose that the Nardelli Master Equation, enriched by these connections, may serve not only as a tool for mathematical insight but also as a symbolic vessel for understanding the deep harmony between the microcosm of numbers and the macrocosm of the universe. This work invites further exploration into the structural unity of mathematics and physics thought.

This article aims to guide the reader through the derivation of a system of unifying equations, unraveling its surprising numerical connections, and finally discussing its profound implications for our understanding of the cosmos.

Keywords: number theory, string theory, theoretical cosmology, supersymmetry, theory of everything, geometric measure theory.

Author: Studied at Dipartimento di Scienze della Terra Università degli Studi di Napoli Federico II,Largo S. Marcellino, 10 - 80138 Napoli, Dipartimento di Matematica ed Applicazioni "R. Caccioppoli" -Università degli Studi di Napoli "Federico II" – Polo delle Scienze e delle Tecnologie Monte S. Angelo,Via Cintia (Fuorigrotta), 80126 Napoli, Italy.

I. INTRODUCTION: TOWARDS A UNIFIED FRAMEWORK

Modern theoretical physics is in a phase of intense search for a unifying framework, a paradigm capable of reconciling General Relativity and Quantum Mechanics in a single, coherent "Theory of Everything" (TOE). To overcome the current theoretical impasses, it becomes strategically crucial to explore unconventional connections, such as those that link the abstract purity of number theory to the complex dynamics of cosmology. This work is part of this line of research, proposing an approach that reveals an unexpected harmony between apparently heterogeneous mathematical structures.

London Journal of Research in Science: Natural & Formal

The central thesis of this article is that the "Nardelli Master Equation" and its subsequent evolutions act as a catalyst for this unification. They reveal an intrinsic resonance between the discrete structures discovered by the brilliant intuition of Srinivasa Ramanujan and the continuous principles that govern the evolution of the cosmos. The equations we will present are not simple formulas, but a mathematical architecture that suggests how fundamental constants, iconic numbers, and physical principles can emerge from a common source.

The structure of the article will follow a logical path. We will begin with the presentation of the fundamental equations that form the core of our system. Next, we will analyze their numerical bases, demonstrating how Ramanujan's famous numbers, 1729 and 4096, emerge naturally from their structure. Finally, we will discuss the profound implications of this mathematical framework for string theory and cosmology, showing how it is possible to derive fundamental physical parameters, such as the dilaton value.

Let us now proceed to the formal exposition of the key equations that constitute the foundation of this investigation.

II. THE FUNDAMENTAL UNIFICATION EQUATIONS

This section lays the mathematical foundation of the entire argument. The equations presented should not be seen as isolated formulas, but as interconnected elements of a single theoretical system, whose internal coherence reveals deep links between geometry, number theory and physics. They represent the starting point for the analysis that will follow.

Below, we present the key formulations of our theoretical framework.

- *The Genius Equation:* This equation represents the starting point of our framework.

$$\int_L \frac{\phi_{GN}^7 |\nabla f \cdot \nabla g|^3}{\left(|f|^2+|g|^2+\phi_{GN}^{14}\cdot(0.00422\cdot 390)\cdot t_l \cdot \frac{6.47466}{4}\right)^{7/2}} dV = \frac{256\pi^8 \phi_{GN}^7 (0.00422\cdot 390)\cdot t\cdot (4096+1729)^{1/18}}{\phi_{GN}}$$

- *The Ramanujan-Gemma-Nardelli Unification Equation (RGNUE):* This formulation incorporates the term $e^{\Phi}\ G_4 \wedge * G_4$ of Theory M in the framework of the Genius Equation, converging on a numerical value of considerable importance.

$$\phi_{GN} \approx \sqrt[7]{\frac{\int_{L\subset X} \frac{\phi_{GN}^7 |\nabla f \cdot \nabla g|^3}{\left(|f|^2+|g|^2+\phi_{GN}^{14}\cdot c\cdot t_l \frac{6.47466}{4}+e^{\Phi} G_4 \wedge * G_4\right)^{7/2}} dV}{256\pi^8 c\cdot t\cdot \frac{(4096+1729)^{1/18}}{\phi_{GN}} \cdot \left(\frac{1}{\pi\rho^2}\int_{\Gamma\subset\partial L} |d\mu|\right)}} \approx 1.618665$$

- *The Action or Unified Golden Equation:* This action equation integrates the Master Equation, the Genius Equation, and the action of M Theory into a single framework, whose behavior is modulated by the constant φ_{GN}.
- *The TOE Equation (updated version):* This is the most complete and complex formulation, which integrates numerous corrective terms and converges towards the same fundamental value, highlighting its rich internal structure.

$$E_\infty = \left(\sqrt[7]{\frac{\int_{L\subset X} \frac{\phi_{GN}^{7}\,|\nabla f\cdot\nabla g|^{3}}{\left(|f|^{2}+|g|^{2}+\left(\phi_{GN}^{14}\cdot c\cdot t_l\cdot\frac{6.47466}{4}+3.3178\times10^{88}+5.794\times10^{209}\right)+e^{\Phi}\,G_4\wedge *G_4\right)^{7/2}}\,dV}{256\pi^{8}c\cdot t\cdot\frac{(4096+1729)^{1/18}}{\phi_{GN}}\cdot\left(\frac{1}{\pi\rho^{2}}\int_{\Gamma\subset\partial L}|d\mu|\right)\cdot 1.61738\cdot 1.6164}} \right)^{3}$$

$$\cdot\left[\int_0^\infty e^{-t^2}\cdot\frac{\mathcal{H}^2}{4M_P^{2\sqrt{3}}\gamma^2\epsilon(t)\left(\pi t\cdot\frac{\phi_{GN}}{2}\right)^3}\cdot\frac{2\sqrt{2}}{\pi}\right.$$

$$\left.\cdot\left(\frac{1}{4}f\left(e^{i\left(\pi t\cdot\frac{\phi_{GN}}{2}\right)}\right)+\frac{1}{4}\phi\left(e^{i\left(\pi t\cdot\frac{\phi_{GN}}{2}\right)}\right)+\frac{1}{4}\psi\left(e^{i\left(\pi t\cdot\frac{\phi_{GN}}{2}\right)}\right)+\frac{1}{4}f_0\left(e^{i\left(\pi t\cdot\frac{\phi_{GN}}{2}\right)}\right)\right)\right.$$

$$\left.\cdot\left(-\frac{1.646014}{2\pi l_s^2}\int d^2\,\sigma\sqrt{-\det\left(\eta_{\mu\nu}\,\partial_\alpha X^\mu\,\partial_\beta X^\nu\right)}\,e^{\Phi/2}\right)^3\cdot(1+0.991)\right.$$

$$\left.\times\frac{1}{123}\frac{1}{4}(0.010000174+0.010000212+0.010000231+0.010000230)dt\right.$$

$$\left.+\frac{2}{p'}|f|_{L^{p,\varphi}(I)}\int_0^1\frac{t^{\frac{1}{p'}}}{\varphi^{\frac{1}{p}}(t)^{\frac{1}{2}}}dt\right.\ \approx 1.618665$$

The crucial significance of these formulations is that they collectively establish a fundamental value for the system, $\varphi_{GN} \approx 1.618665$. This value, extraordinarily close to the golden ratio, does not appear as an arbitrarily inserted constant, but as a natural point of convergence of the entire mathematical architecture.

This convergence requires a more in-depth analysis of the origin and meaning of φ_{GN}, which we will address in the next section.

III. ANALYSIS OF THE GEOMETRIC STRUCTURE AND THE CONSTANT

To understand the origin of the constant φ_{GN}, it is essential to analyze a specific term that lies at the heart of the equations presented: the integral $\int e^{\Phi}\, G_4 \wedge * G_4$. This term, typical of M Theory and 11-dimensional supergravity, is the key to understanding how fundamental physics ties into a universal geometric constant. Its relationship to the other components of the equation reveals the deep nature of φ_{GN}.

The fundamental formula that serves as a matrix for our theoretical framework is:

$$\int_X e^{\Phi} G_4 \wedge * G_4 = \phi_{GN}\left(\frac{1}{\pi\rho^2}\int_\Gamma |d\mu|\right)$$

We can dissect the meaning of this expression by analyzing its components:

1. *Field and geometry:* The left-hand integral term, $\int e^{\Phi}\, G_4 \wedge * G_4$, represents the energy-action associated with the self-dual field form G_4 in the entire space X, weighted by the potential of the dilaton e^{Φ}. This term encapsulates the bosonic dynamics of the theory.
2. *Golden-geometric term:* On the right side, the constant φ_{GN} acts as a universal resonance factor. It ties geometric energy density to a topological measure of the boundary, suggesting that the constant emerges as an intrinsic relationship of geometry itself.
3. Continuous-discrete bridge: The term $1/(\pi\rho^2) \int |d\mu|$ constitutes the bridge between the continuous domain of space (X) and its discrete boundary (Γ), establishing the symmetry of the measure-form duality.

This relation allows us to algebraically isolate φ_{GN}, revealing its structural nature. Multiplying both sides by $\pi\rho^2$ and dividing by the integral on the edge Γ gives the intermediate step:

$$\Phi_{GN} = \frac{\pi\rho^2 \int_X e^{\Phi} G_4 \wedge {}^*G_4}{\int_\Gamma |d\mu|}.$$

Using the compact notation for normalized edge measurement, $M_\Gamma := 1/(\pi\rho^2) \int |d\mu|$, the derivation takes on an even more elegant shape:

$$\Phi_{GN} = \frac{\int_X e^{\Phi} G_4 \wedge {}^*G_4}{M_\Gamma}$$

The deep meaning of this derivation is that the constant φ_{GN} is not an arbitrary value. It emerges as a fundamental relationship between the energy of the field that permeates the internal volume and a normalized measure of its outer boundary. This result suggests a geometrization of the golden number, where an apparently numerical constant is actually an intrinsic property of the geometric-physical structure of spacetime.

Having established its geometric origin, it is now time to explore the surprising connection between φ_{GN} and number theory, a link that reveals its even deeper resonance.

IV. Numerical Resonances: The Link Between , 1729 and 4096

This section is of fundamental strategic importance. The numerical analysis that follows is not a simple mathematical curiosity, but a crucial test of the internal consistency of the theory. We will demonstrate how iconic numbers of Ramanujan's mathematics, such as 1729 (the "taxicab" number) and 4096 (2^{12}), emerge naturally from the harmonic structure defined by the constant φ_{GN}, reinforcing the idea of a unified mathematical architecture.

Let's consider the following numerical relation, which links our fundamental constant to Ramanujan's numbers: $1.618665^{18} - 1729 + 2\pi \approx 4095.9778\ldots$ This result is remarkably close to 4096, or 2^{12}, a value we identify as a "Ramanujan-modular resonance". The proximity is such as to suggest a relationship that is not casual, but a quasi-identity that reflects an intrinsic harmony.

To make this identity exact, we can perform a "calibration" of the base. If we impose that the result is exactly 4096, we can solve for the base x: $x = (4096 + 1729 - 2\pi)^{1/18}$. The calculation gives a numerical value for this calibrated basis, which we will call φ^*: $x \approx 1.61866534172$. This φ^* basis is almost identical to φ_{GN}, with a difference of about 3.4×10^{-7}, confirming that the relationship is structural. Reorganizing the equation, we get an expression with a deep symbolic meaning: $1729 = \Phi^{18} + 2\pi - 2^{12}$. This formula beautifully combines:

1. Ramanujan's taxicab number (1729): An icon of discrete number theory.
2. Geometric resonance ($4096 = 2^{12}$): A modular base that connects the cubic world to the binary exponential world.
3. The golden base ($\Phi = 1.618665$): Our fundamental constant φ_{GN} (or its calibrated version φ^*).

Let's continue the analysis using this relationship. Consider the following expression, which combines the above result with the Marvin Ray Burns Constant (MRB):

$$\left(\phi^{*18} + 2\pi - 2^{12}\right)^{1/15} + (MRB)^{1-\frac{1}{4\pi}+\pi}$$

By construction, the first term is $(1729)^{(1/15)}$.

The step-by-step calculation of the two contributions provides:

1. First term: $(1729)^{1/15} \approx 1.64381522875$
2. Second term (MRB): $(0.18785964)^{1-\frac{1}{4\pi}+\pi} \approx 0.00112279532$

Their sum is: $1.64381522875 + 0.00112279532 = 1.64493802407$ This result is surprisingly close to the value of the Riemann Zeta function for s=2: $\zeta(2) = \frac{\pi^2}{6} \approx 1.64493406685$. The relative error between our result and $\zeta(2)$ is tiny, about 2.4×10^{-6}, indicating another deep connection.

This convergence allows us to build a formula that links our architecture directly to π. Consider the following expression:

$$F = \sqrt{6 \cdot \left[\left(-2^{12} + \phi^{18} + 2\pi\right)^{1/15} + (MRB)^{1-\frac{1}{4\pi}+\pi}\right]} \approx \pi$$

The numerical calculation of F gives 3.141595094..., for $\phi = 1.618665$, a value that approximates π with a relative error of about 7.8×10^{-7}. The structure of this formula can be summarized in the following interpretative scheme:

Element	Symbolic role
φ^{18}	Golden Exponential Core
2π	Transcendental curvature term
$2^{12} = 4096$	Ramanujan Modular Resonance
MRB constant	Fine corrective phase
$\sqrt{6}$	Zeta Bridge–π

The conceptual reading of this architecture is clear and powerful:

$$Golden\ Harmony + MRB \rightarrow \zeta(2) \quad \Rightarrow \sqrt{6 \cdot \zeta(2)} = \pi$$

These extraordinary numerical connections are not mere coincidences, but find a direct parallel in cosmological and string theory models, as we will see in the next section.

V. IMPLICATIONS FOR STRING THEORY AND COSMOLOGY

The mathematical foundations established in the previous sections are not an abstract exercise; they are directly linked to concrete physical concepts. The validity of our theoretical framework can be corroborated by deriving known physical parameters, such as the value of the dilaton field, and showing its consistency with existing cosmological models.

Based on the work of Mourad and Sagnotti, we analyze the connection between the vacuum equations of supergravity and Ramanujan's mathematics. One of the key equations of the vacuum can be related

to a famous Ramanujan exponential through the following identity: $e^{-6C+\phi} = 4096e^{-\pi\sqrt{18}}$. The significance of this connection is profound: the coefficient 4096 (2^{12}), which we have identified as a modular resonance in our framework, is not random. It directly ties an exponential characteristic of Ramanujan's mathematics to an exponential one that describes the vacuum of string theory. This identity allows the value of the dilaton φ to be mathematically established.

Putting C=1 (a specific but significant case) and solving the equation, we get:

$$-6 + \phi = \ln ln\left(4096 \cdot e^{-\pi\sqrt{18}}\right) = \ln ln\,(4096) - \pi\sqrt{18}$$

From which we derive the value of the dilaton:

$$\phi = 6 + \ln ln\,(0.00666501785) = 6 - 5.010882647757 = 0.989117352243$$

This value of the dilaton converges remarkably with other physical and mathematical parameters, such as the ns spectral index (0.965) and values derived from continuous Rogers-Ramanujan fractions, reinforcing the physical validity of our approach.

Our theoretical framework can be extended to include 5D cosmological models. Consider the following formula, from a 5D gravitational context, which describes a component of the energy-impulse tensor or a scalar field σ:

$$\sigma = \frac{3}{8\pi G_5}\left(\sqrt{k_-^2 + \frac{1+\dot{a}^2}{a^2}} - \sqrt{k_+^2 + \frac{1+\dot{a}^2}{a^2}}\right)$$

where G_5 is the gravitational constant 5D, A is the cosmic scale factor and k are curvature parameters. We propose to integrate σ within our TOE Equation to create an extended version, the "TOE_{5D}". The term σ is inserted inside the main parenthesis of the denominator, along with the other large numeric constants:

$$TOE_{5D} = \phi_{GN} \cdot \frac{\int_{L\subset X} \phi_{GN}^{7} \frac{|\nabla f \cdot \nabla g|^3}{\left(|f|^2+|g|^2+\left(\phi_{GN}^{14}\cdot c\cdot t_l \cdot \frac{6.47466}{4}+3.3178\times10^{88}+5.794\times10^{209}+\frac{3}{8\pi G_5}\left(\sqrt{k_-^2+\frac{1+\dot{a}^2}{a^2}}-\sqrt{k_+^2+\frac{1+\dot{a}^2}{a^2}}\right)\right)+e^{\Phi}G_4\wedge^* G_4\right)^{7/2}} dV}{256\pi^8 c\cdot t\cdot\left(\frac{E_\infty}{Dynamic\ Term}\right)^{7/3}\cdot\left(\frac{1}{\pi\rho^2}\int_{\Gamma\subset\partial L}|d\mu|\right)\cdot 1.61738\cdot 1.6164}$$

In this formulation, the term σ modulates the energy density within the integral, thus linking the cosmic expansion (described by a and ȧ) to the fundamental harmonic structure of the TOE. This suggests a bridge between 5D cosmology, the golden ratio, and zeta-type constants.

These extensions and connections demonstrate that the theoretical framework is not static, but evolves to incorporate new physical principles, leading to an increasingly complete version of the TOE Equation.

VI. EVOLUTION AND FINAL SYNTHESIS OF THE TOE EQUATION

Scientific research is a dynamic and progressive process. In this section, we illustrate how a specific breakthrough allowed the harmonic basis of the TOE Equation to be further refined, leading to a more complete and coherent formulation. This development demonstrates the evolutionary nature of our theoretical framework.

The crucial evolutionary step is the "October 12, 2025 formula," which provides a more refined basis for the mathematical TOE. The formula is as follows:

$$\left(4096 + \left(\pi \cdot \ln ln\left(5.794 \times 10^{209}\right) + 233 - 21 - \frac{1}{\pi}\right)\right)^{1/18}$$

The calculation of this expression returns a value of ≈ 1.61876. This result is remarkably close to our fundamental constant $\varphi_{GN} \approx 1.618665$. The difference is minimal and can be interpreted as a fine "cosmological adjustment". In particular, the logarithmic term $\ln(5.794 \times 10^{209})$ links the harmonic base to one of the large constants that appear in the denominator of the TOE Equation, suggesting a self-consistent calibration.

This new wording integrates elegantly into the TOE Equation, replacing the original term (4096 + 1729). The updated version, which we call $TOE_{updated}$, is built using this new base:

$$TOE_{updated} = \left(4096 + \left(\pi \cdot \ln ln\left(5.794 \times 10^{209}\right) + 233 - 21 - \frac{1}{\pi}\right)\right)^{1/18} \cdot \frac{\int ....dV}{[denominator]}$$

In this summary, progress is clear. The new formula serves as a more refined basis that directly approximates φ_{GN}. The rest of the equation (the integral and the denominator) acts as a scaling factor to tune the result. As calculated from our model, the eighteenth power of the new base is ≈ 5828. To reach the harmonic target of 2367 (derived from 4096 - 1729), the scale factor must be ≈ 0.919. This shows how each component of the equation plays a precise role in the overall architecture.

This development represents a significant step towards a complete and internally consistent formulation, where each component is interconnected and justified by the overall structure.

VII. CONCLUSIONS AND INTERPRETATIVE SCHEME

In this article, we have presented an in-depth analysis of the unification equations, strongly reaffirming the central thesis of a deep structural unity between pure mathematics and fundamental physics. The Nardelli Master Equation and its evolutions have proved to be a powerful tool to unravel this connection, acting as a bridge between seemingly distant conceptual worlds.

Key results show that the fundamental constant $\varphi_{GN} \approx 1.618665$, Ramanujan's iconic numbers (1729, 4096), and universal constants such as $\zeta(2)$ and π are not isolated entities. Instead, they emerge as interconnected nodes of a single mathematical architecture. We have shown how φ_{GN} can be interpreted as an intrinsic geometric relationship, how numerical resonances calibrate with microscopic precision, and how the whole system can be used to derive relevant physical parameters, such as the dilaton value, and to connect to cosmological models.

To provide a physical counterpart to this elegant mathematical structure, we propose an interpretative scheme of the quantum vacuum. Inspired by the graphic models presented in the source material (Figures 1 and 2), we can imagine quantum-scale spacetime not as a smooth canvas, but as a dynamic structure composed of:

1. *Quantum vortices:* Geometric structures similar to cubes or octahedra that represent the energetic fluctuations of the vacuum.
2. *"Bubbles"-Universe:* Potential universes, schematized as spheres, flowing between vortices, representing the quantum foam from which manifest reality can emerge.

In conclusion, as stated in our abstract, this work invites further exploration of the structural unity of mathematical and physical thinking. The equations presented here are not only a calculation tool, but can serve as a "symbolic vessel" for understanding the deep harmony that binds the microcosm of numbers to the macrocosm of the universe, suggesting that the laws of physics could ultimately be a manifestation of the immutable truths of mathematics.

APPENDIX

A further remarkable connection with Ramanujan's numbers emerges from his formula relating to modular equations. Considering the following expression, derived from Ramanujan's work:

$$27\left(\sqrt{4372}-2-\frac{1}{2}\left(\frac{\sqrt{10-2\sqrt{5}}-2}{\sqrt{5}-1}\right)\right)+\varphi \approx 1729.0526944\ldots$$

Where 4372 = 4096 + 276. Its numerical calculation gives the result: 1729.0526944... This value is remarkably close to 1729, the taxicab number. Moreover, it is in close proximity to the mass of the glueball candidate $f_0(1710)$, a scalar meson. Interestingly, the number 1728 (1729 - 1), which lies at the heart of this expression, is the invariant j of an elliptic curve, a central concept in modern number theory.

Raising this same expression to the power of 1/15, we get:

$$\left(27\left(\sqrt{4372}-2-\frac{1}{2}\left(\frac{\sqrt{10-2\sqrt{5}}-2}{\sqrt{5}-1}\right)\right)+\phi\right)^{1/15} \approx 1.64381856$$

This result comes surprisingly close to $\zeta(2) = \pi^2/6 \approx 1.644934$, further strengthening the link between Ramanujan's mathematics. The number 1729 and the fundamental constants that emerge from our unified framework.

VII. CONCLUSIONS AND DISCUSSION

This study has provided an integrated and coherent framework linking the mathematical heritage of Ramanujan to the modern quest for a unified description of the universe.

Through the progressive evolution of the Nardelli Master Equation, we have shown that discrete numerical patterns, geometric measures, and cosmological constants can be interpreted as expressions of a single harmonic principle that governs both mathematics and physics.

The emergence of the golden constant $\phi_{GN} \approx 1.618665$, the appearance of Ramanujan's recurring numbers (1729, 4096), and their convergence toward universal constants such as $\zeta(2)$ and π reveal an underlying architecture where number theory, geometry, and cosmology are no longer separate languages but interconnected manifestations of the same order.

The equations examined demonstrate that the energy–measure duality (volume vs. boundary), typical of geometric measure theory, finds a natural correspondence in string and M-theoretical frameworks, where the integrals.

$$\int e^{\Phi} G_4 \wedge * G_4 \quad \text{and} \quad \frac{1}{\pi\rho^2}\int_{\Gamma} |d\mu|$$

describe the dynamic balance between the field and its boundary. From this duality emerges the golden constant as a true invariant of the space–time structure. Furthermore, the numerical bridges involving Ramanujan's constants, the Marvin Ray Burns constant, and the Riemann zeta function suggest that even transcendental constants may be governed by hidden arithmetic symmetries. This convergence opens the way to a Golden–Zeta cosmology, where ϕ_{GN}, $\zeta(2)$, and πdefine the harmonic parameters of a self-consistent universe.

Ultimately, the TOE Equation derived herein should not be seen as a single formula, but as a *mathematical archetype*: a symbolic and quantitative vessel that unites the microcosm of numbers with the macrocosm of spacetime.

Its structure reveals that harmony, not randomness, governs the laws of the universe — and that, at the deepest level, the language of creation is mathematical.

Formula	Meaning and Role
Genius Equation	The generative seed of the framework; expresses the unity between pure arithmetic and geometric potential, anticipating the harmonic constant .
Ramanujan–Gemma–Nardelli Unification Equation (RGNUE)	Integrates the M-theory term with the golden resonance factor , uniting field energy and geometry.
Action or Unified Golden Equation	The synthesis of the Master Equation, the Genius Equation, and the M-theory action into a single invariant functional governed by .
TOE Equation	The complete, normalized form that includes all corrective terms and converges toward . It encodes the bridge between geometry (continuous), number theory (discrete), and cosmology.
Geometric–Field Matrix Equation $\int_X e^{\Phi}\ G_4 \wedge * G_4 = \phi_{\mathrm{GN}} \left(\frac{1}{\pi\rho^2}\right)$	$\int_\Gamma \lvert d\mu \rvert$.
RamanujanResonance Relation $(1.618665)^{18} - 1729 + 2\pi \approx 4096$	Shows the quantitative harmony between the golden base, Ramanujan's taxicab number, and the modular resonance .
Golden–Zeta Bridge $\mathbf{Bridge}\sqrt{6\,[((\phi^{18} + 2\pi - 4096)^{1/15} + \mathrm{MRB}^{\,1-\frac{1}{4\pi}+\pi})]} \approx \pi$	Demonstrates that the harmonic synthesis of golden, modular, and MRB constants reproduces with micro-accuracy.
5D Brane Equation $\sigma = \frac{3}{8\pi G_5}\left(\sqrt{k_-^2 + \frac{1+\dot{a}^2}{a^2}} - \sqrt{k_+^2 + \frac{1+\dot{a}^2}{a^2}}\right)$	Derived from Israel's junction conditions; connects the TOE framework to 5D cosmological models, completing the unification bridge.

ACKNOWLEDGMENTS

We would like to thank Professor Augusto Sagnotti, theoretical physicist at the Scuola Normale Superiore in Pisa, for his very useful explanations and his availability.

REFERENCES

1. Nardelli, M., Kubeka, A.S. and Amani, A. (2024) A Number Theoretic Analysis of the Enthalpy, Enthalpy Energy Density, Thermodynamic Volume, and the Equation of State of a Modified White Hole, and the Implications to the Quantum Vacuum Spacetime, Matter Creation and the Planck Frequency. *Journal of Modern Physics*, 15, 1-50. https://doi.org/10.4236/jmp.2024.151001
2. The Geometry of the Universe: in Search of Unity. New Possible Mathematical Connections with the DN Constant, Ramanujan's Recurring Numbers and Some Parameters of Number Theory and String Theory - Michele Nardelli, LJRS Volume 25 Issue 6 - Published On May 2, 2025
3. The Nardelli Master Equation, the Extended DN Constant and its Connection to the Golden Ratio Revisited. Mathematical Connections with Some Sectors of Number Theory and Theoretical Cosmology - Michele Nardelli, LJRS Volume 25 Issue 9 - Published On July 31, 2025
4. Dark bubble cosmology and the equivalence principle - Ivano Basile, Alessandro Borys,† and Joaquin Masias‡ - arXiv:2507.03748v1 [hep-ph] 4 Jul 2025
5. Ramanujan, S. (1914) Modular equations and approximations to π. *Quarterly Journal of Mathematics*, XLV, 350-372.
6. Mourad, J. and Sagnotti, A. (2017) An Update on Brane Supersymmetry Breaking. *arXiv:1711.11494v1 [hep-th].*

Physico-Chemical, Rheological, Structural, Thermal, Mechanical and Barrier Properties of Hybrid Powder and Films from Cassava Starch Crosslinked with Xanthan Gum

Marisa Ferreira Karow, Karine Laste Macagnan, Mariane Igansi Alves, Patrícia Diaz, Lígia Furlan, Claire Tondo Vendrucolo & Angelita da Silveira Moreira

Federal University of Pelotas

ABSTRACT

Starch and xanthan are viscosifying, film-forming polysaccharides obtained from renewable sources. The main objective of this work was to assess the effects of the cassava starch/deacetylated xanthan proportion and reaction time in the crosslinking performed with sodium trimetaphosphate on the Physico-chemical, rheological, structural, thermal, mechanical and barrier properties of resulting hybrid polymeric powder and films. Xanthan deacetylation, performed to improve crosslinking, increased xanthan viscosity and pseudoplasticity. For further crosslinking, the crosslinking agent (SMTP) and the alkalizing agent sodium sulfate (SS) concentration was set at 5% and 3% respectively relative to the total polymeric mass (5%m/v); and according to the Central Composite Rotatable Design (DCCR 2^2) the starch/deacetylated xanthan proportion and reaction time was varied, totalizing 11 treatments with 3 repetitions at the central point. Physical and chemical features of the crosslinked polymers were checked, as well as films based on the crosslinked hybrid polymers were prepared and tested. Treatments that showed best results were T1 (s/x: 4.5/0.5; 52 min.) and T4 (s/x: 3.5/1.5; 127 min). These resulted in low solubility, thickness and permeability to water vapor, with high tensile strength.

Keywords: starch/xanthan proportion, reaction time, viscosity, hydrophilic films characterization.

Classification: LCC Code: TP248.65.P65, QD476, TA455.P58

Language: English

Great Britain Journals Press

LJP Copyright ID: 925614
Print ISSN: 2631-8490
Online ISSN: 2631-8504

London Journal of Research in Science: Natural & Formal

Volume 25 | Issue 13 | Compilation 1.0

Physico-Chemical, Rheological, Structural, Thermal, Mechanical and Barrier Properties of Hybrid Powder and Films from Cassava Starch Crosslinked with Xanthan Gum

Marisa Ferreira Karow[α], Karine Laste Macagnan[σ], Mariane Igansi Alves[ρ], Patrícia Diaz[ᾠ], Lígia Furlan[§], Claire Tondo Vendrucolo [χ]& Angelita da Silveira Moreira[ν]

ABSTRACT

Starch and xanthan are viscosifying, film-forming polysaccharides obtained from renewable sources. The main objective of this work was to assess the effects of the cassava starch/deacetylated xanthan proportion and reaction time in the crosslinking performed with sodium trimetaphosphate on the Physico-chemical, rheological, structural, thermal, mechanical and barrier properties of resulting hybrid polymeric powder and films. Xanthan deacetylation, performed to improve crosslinking, increased xanthan viscosity and pseudoplasticity. For further crosslinking, the crosslinking agent (SMTP) and the alkalizing agent sodium sulfate (SS) concentration was set at 5% and 3% respectively relative to the total polymeric mass (5%m/v); and according to the Central Composite Rotatable Design (DCCR 2²) the starch/deacetylated xanthan proportion and reaction time was varied, totalizing 11 treatments with 3 repetitions at the central point. Physical and chemical features of the crosslinked polymers were checked, as well as films based on the crosslinked hybrid polymers were prepared and tested. Treatments that showed best results were T1 (s/x: 4.5/0.5; 52 min.) and T4 (s/x: 3.5/1.5; 127 min). These resulted in low solubility, thickness and permeability to water vapor, with high tensile strength.

Keywords: starch/xanthan proportion, reaction time, viscosity, hydrophilic films characterization.

*Author*α ρ ν: Postgraduate Program in Food Science and Technology, School of Agronomy Eliseu Maciel, Federal University of Pelotas, RS, Brazil.
σ ᾠ ν: Postgraduate Program in Biotechnology, Technological Development Center, Federal University of Pelotas, RS, Brazil.
§: Center for Chemical, Pharmaceutical and Food Sciences Federal University of Pelotas, RS, Brazil.
χ: Biopolix Technological Materials.

I. INTRODUCTION

Starch and xanthan are polysaccharides obtained from renewable sources, having a number of applications in food products as thickening agents and for coatings, films, microspheres, nanoparticles and matrices (Jain et al., 2008; Nsengiyumva & Alexandridis, 2022; Teng et al., 2025). Starch is one of the most abundant natural materials and has already countless industrial applications (Lecorre et al., 2012). In spite of the benefits of starch, as relates to biodegradability, biocompatibility, non-toxicity and excellent cost-benefit ratio (Li et al., 2012), it does not meet totally the properties required by food coatings and protecting films, with highlights for mechanical performance and poor water barrier of the formed films. In order to improve or adapt these properties, starch can be submitted to physical and chemical modification processes (Sandhu et al., 2008; Zavareze et al., 2012; Wang & Copeland, 2015; Villela et al., 2024).

London Journal of Research in Science: Natural & Formal

Modified starch has been employed in the development of biodegradable films and coatings for food packaging because they are endowed with improved physical, chemical, morphological and mechanical properties as compared with those of native starch films (Zavareze et al., 2012; Fonseca et al., 2015). A recent study showed that cross-linked cassava starch films had better easiness of handling, continuity, and brightness than the control film. Generally, cross-linking reduced the water solubility and tensile strength and increased thickness, elongation and the films' yellowish color and opacity (Karow et al., 2025).

Starch/hydrocolloids associations have also been studied aiming at new formulations for the improvement of film features (Matta et al., 2011). Hydrocolloids can intervene in the gelatinization and retrogradation of starches (Pongsawatmanit & Srijunthongsiri, 2008; Weber et al., 2009), these properties being able to affect film features. Among the explanations for such are the association of same with swollen starch or with amylose chains lixiviated in the paste and competition for water with starch. Such associations are highly dependent on the hydrocolloid structure (Chaisawang, 2006).

Researches involving xanthan as polymeric matrix for preparing films and coatings are still limited. However, its use in association with starch or other hydrocolloids is better known (Shalviri et al., 2010). Xanthan is a polysaccharide produced by bacteria species of the *Xanthomonas* gender, normally *Xanthomonas campestris* pv campestris. It is soluble in cold or hot water, being stable as relates to temperature, pH and ionic strength variation. It has been used in foods as thickening agent and stabilizer (García-Ochoa et al., 2000) and as edible coating (Luvielmo & Scamparini, 2009; Medeiros et al., 2012) on minimally processed papaya (Cortez-Veja et al., 2013), apple (Freitas et al., 2013), peach (Pizato et al., 2013), strawberry (Borges et al., 2013) and pomegranate (El-Rhouttais et al., 2025); however, results depend on the specific fruit as well as on the additives. Chemical modifications have been applied to xanthan (Pinto et al., 2011; Erten et al., 2014; Klaic et al., 2016), chiefly deacetylation and crosslinking. Polymer crosslinking is a process occurring when linear or branched polymer chains are interconnected; it is known as crosslinking, that is, links among linear molecules leading to high molar mass tridimensional polymers (Bejenariu et al., 2009).

The objective of this work was to assess the crosslinking effects of native manioc starch/deacetylated xanthan with sodium trimetaphosphate and sodium phosphate mixture as a function of reaction time on the filmogenic and rheological properties.

II. MATERIAL AND METHODS

2.1. Material

Native marketed manioc starch YOKI® was used, purchased at the local markets of the town of Pelotas-RS, and chemically modified by crosslinking at the Biopolymers Laboratory - CDTec/UFPeL. Commercial (Jungbonzlaver) xanthan was employed in the study; it was deacetylated at the Biopolymers Laboratory - CDTec/UFPeL. Sodium trimetaphosphate p.a. (Synth®), anhydrous sodium sulfate p.a. (Synth®), glycerol p.a. (Synth®), alcohol 96°GL and distilled water were employed for the chemical modification.

2.2. Chemical Modification

At first natural xanthan was deacetylated in an alkaline homogeneous medium, in accordance with Klaic et al (2016). Determination of the native manioc starch/deacetylated xanthan proportions and reaction time was obtained with the aid of Central Composite Rotatable Design. The proportions of native manioc starch/deacetylated xanthan 4.5/0.5; 3.5/1.5; 4.7/0.3; 3.3/1.7; 4.0/1.0 m/m; and the reaction times 37; 52; 90; 127 and 142 minutes were assessed through 11 treatments with three

repetitions at the central point. Crosslinking of the native manioc starch/deacetylated xanthan mixtures was performed in accordance with Soares et al (2013), with modifications on the time of chemical reaction and reagents' concentration. The concentrations of the crosslinking agent sodium trimetaphosphate and the alkalizing agent sodium sulfate, as well as the polymer mass, were determined in a previous study, in which the crosslinking of cassava starch was performed (Karow et al., 2025). In the present study, part of the initial concentration of cassava starch was replaced with deacetylated xanthan. All the proportions used totalized 5% of polymer mass. The dispersion of the different mixtures was performed in distilled water at ambient temperature and the suspensions were placed in a water bath under agitation up to 65°C for 15 min. Then the pH was adjusted to 9.5 with a 0.5M NaOH solution and sodium trimetaphosphate (STMP) in the proportion of 5.0 % and sodium sulfate (SS) in the proportion of 3.0% was added relative to the starch/xanthan (s/x) mass and transferred to another water bath at 45°C. Whenever needed, the pH was again adjusted to 9.5. This mixture was kept under magnetic agitation for 37; 52; 127; 142 minutes in accordance with DCCR 2^2. When the reaction time was completed, the pH was adjusted to 6.0 with the aid of a 2M HCl solution. The samples were washed with ethanol, filtered, oven-dried at 45°C and later on thoroughly milled.

Table 1: Central Composite Rotational Design (CCRD 2^2) for crosslinking of the native manioc starch/deacetylated xanthan mixture

Treatment	Codified Levels		Actual Levels	
	X[a]	Y[b]	Starch + Xanthan (%)	Reaction Time (min)
T1	-1	-1	4.5 + 0.5	52
T2	+1	-1	3.5 + 1.5	52
T3	-1	+1	4.5 + 0.5	127
T4	+1	+1	3.5 + 1.5	127
T5	- 1.41	0	4.7 + 0.3	90
T6	+ 1.41	0	3.3 + 1.7	90
T7	0	- 1.41	4.0 + 1.0	37
T8	0	+ 1.41	4.0 + 1.0	142
T9	0	0	4.0 + 1.0	90
T10	0	0	4.0 + 1.0	90
T11	0	0	4.0 + 1.0	90

[a] Starch + xanthan (%).
[b] Reaction Time (min).

2.3. Determination of acetyl and pyruvate content of the natural and deacetylated xanthan

The acetyl content of natural and modified xanthan gums was performed with the aid of the hydroxamic acid colorimetric method as taught by McComb & McCready (1957) while the pyruvate contents were determined by the 2,4-dinitrophenylhydrazine colorimetric method, according to Sloneker & Orentas (1962). Acetyl and pyruvate contents were quantified with the aid of a standard curve at the concentration of 0-450 µg/mL and 0 – 0.25 mg/mL, respectively.

2.4. Characterization of native starch manioc, natural xanthan and native manioc starch/deacetylated xanthan crosslinked mixtures

2.4.1. Humidity

In accordance with the AOAC (2012) method. Results were expressed in percentage.

2.4.2. Scanning Electronic Microscopy (SEM)

The morphology of native starch, of the natural and deacetylated xanthan gums and of the crosslinked mixtures of native manioc starch/deacetylated xanthan was observed with a digital scanning electronic microscope (Leo® model 440). The previously 40°C oven-dried samples were manually dispersed on a carbon adhesive tape contained in an aluminum sample holder and recovered with gold, the cover thickness being 20 nm. The beam current was 1 pA and the beam power, 10 KV.

2.4.3. Infrared Spectroscopy – IV

Native manioc starch, natural xanthan, deacetylated xanthan and crosslinked native manioc starch/deacetylated xanthan mixtures infrared spectra were obtained by patching 2 mg of the samples, milled (100 mesh) and dried, in 200 mg of spectroscopic grade potassium bromide. Analyses were conducted in a (Model IR Prestige 21, Shimadzu®) spectrophotometer, in the wave number range from 4,000 to 400 cm^{-1}under transmittance mode, with 60 scannings and 4 cm^{-1}resolution.

2.4.4. Rheometric Analyses

Native manioc starch, natural xanthan, deacetylated xanthan and crosslinked native manioc starch/deacetylated xanthan mixtures were analyzed; as a control of the crosslinking process, the physical mixtures of native manioc starch/deacetylated xanthan with the higher and lower xanthan level were also analyzed. Rheometry was performed with a rheometer (Haake® Rheostress 600, model RS150) with a temperature controller (Peltier, ± 0.1 °C). The viscosity of the 3% aqueous solutions was determined by shear stress curves versus deformation rate at 25°C, with the aid of cone and plate geometry (C35/1° sensor; 0.052 mm gap) and shear rate 0.1-400 $s^{-1}$for 400 s. The index of consistency K (Pa/s) and flow *n* (nondimensional) parameters of the Ostwald-de-Waele rheological model were obtained from the viscosity curves (mPas) versus deformation rate (s^{-1}) at 25 °C, of the 3% (m/v) aqueous solutions.

2.4.5. Thermal Properties - DSC

The thermal properties of the native manioc starch, natural and deacetylated xanthan and native manioc starch/deacetylated xanthan mixtures were assessed in a scanning differential calorimeter (ASTM, 2013). Approximately 5 mg of each sample were weighed in an aluminum capsule and closed hermetically. The samples' containing capsules were heated, together with an empty capsule as reference, under a nitrogen atmosphere to secure an inert atmosphere during the analyses, under a flow of 50 mL/min; the equipment was a DSC-60 Shimadzu, heating was performed between 25 °C and 240 °C, under a heating rate of 10°C/min and cooling from 250 °C to 100 °C at a 10°C/min rate.

The samples start, peak and final melting temperatures were obtained, as well as the melting enthalpy. The temperature variation was calculated by subtracting the final and starting melting temperatures.

2.5. Preparation and characterization of films

2.5.1. Preparation of films

Based on the native manioc starch and the 11 native manioc starch/xanthan deacetylated mixtures (T1 to T11) obtained by the crosslinking process, as stated in experimental design CCRD 2^2, 13 films were produced by the casting method, being named as FC (Control Film) and F1 to F11, respectively. The different filmogenic solutions were prepared by casting 3.0 g of the native manioc starch/deacetylated xanthan crosslinked mixture and 0.9g glycerol in 100 mL water as solvent. This solution was kept for 30 min at 85°C under mechanical agitation and 20 mL aliquots were distributed in 9 cm diameter Teflon plates and dried in an oven at 56°C for 24 h, being stored in a desiccator at 25 °C ± 3 °C with relative humidity of 55% ± 3 (in the presence of a magnesium nitrate saturated solution).

2.5.2. Macroscopic assessment

Films were assessed macroscopically by the general aspect, followed by the parameters described by Gontard et al. (1992) to select the homogeneous films (absence of insoluble particles and bubbles, uniform color), continuous (without the presence of cracks or brittle zones) and that make handling possible (ease in withdrawing films from the support).

2.5.3. Scanning Electron Microscopy (SEM)

Films SEM was performed as described in 2.4.2 item, with a small fragment of each film, previously 40°C oven dried, being manually laid on the carbon adhesive tape.

2.5.4. Water Vapor Permeability (WVP)

Permeability was assessed in accordance with Gontard and collaborators (1992). The film was placed in a silica gel-containing cell (RU = 0%, 0 mm Hg vapor pressure), forming a membrane. The cell was then placed in a desiccator with distilled water (RU = 100%; 32.23 mm Hg vapor pressure) under a controlled temperature of 22°C. The cell was weighed in a semi-analytical scale on the sixth day. The permeability was calculated by means of equation 2:

$$WVP = \frac{G \times V}{A \times t\,(p1-p2)} \quad (2)$$

Where: WVP = water vapor permeability (g.mm/m².day.mm.Hg); G = weight acquired by the cell during 24 hours (g); V = film average thickness (mm); A = film permeation surface (m²); t = time (days); p1-p2 = vapor pressure gradient between the film surfaces (32.23 mmHg).

2.5.5. Water solubility

The films were assessed as for their water solubility according to the methodology described by Zamudio-Flores and collaborators (2010) with modifications. Films' samples were cut into 2 cm squares and the initial dry matter percentage of each one was determined after drying in an oven at 105°C for 24 h. After weighing, the samples were placed in an Erlenmeyer flask with 50 mL of distilled water and agitated at 200 rpm for 24 h.

2.5.6. Thickness

Films' thickness was assessed in accordance with ASTM F2251 - 13 (2013) Method by the arithmetic average of ten aleatory measurements on their surface, with the aid of a digital micrometer (Insize, model IP-54), and the results expressed in mm.

2.5.7. Mechanical properties

Tensile strength and films' elongation percentage were assessed in a texture analyzer (TA.TX Plus, *Texture Analyzer*) in accordance with the ATM D 882 - 12 (ASTM, 2012) Method. Three samples of each treatment, with 80 mm length and 25 mm width were assessed, with initial claw separation of 40 mm and test velocity 0.8 mm/s. Tensile strength was calculated by dividing the maximum strength at films failure by the cross-sectional area. Elongation was determined by dividing the final attained distance at film failure by the initial separation distance (40 mm), multiplied by 100 (Jangchud & Chinnan, 1999).

2.5.8. Opacity

Films opacity was assessed as the relationship between opacity of the film superimposed on the black standard (Sblack) and white standard (Swhite) (Hunterlab, 1997).

2.6. Statistics

Results were submitted to variance analysis (ANOVA) and the comparison of averages by the Tukey test at 5% significance with the aid of the *statistix* 9.0 program. Central Composite Rotatable Design (DCCR 2^2) was used and the generated response surfaces, the *statistica* 8.0 program.

III. RESULTS AND DISCUSSION

3.1. Chemical characterization of natural and deacetylated xanthan

Table 2 lists the figures obtained for the acetyl and pyruvate contents for natural xanthan and those from the xanthan chemical modification.

Table 2: Contents for natural xanthan and from xanthan chemical modification Sample Contents (%) Acetyl Pyruvate

Sample	Contents (%)	
	Acetyl	Pyruvate
Natural xanthan	2.76^a	4.00^b
Deacetylated xanthan	0.71^b	5.09^a

Results represent the average of three determinations. Figures with different letters in the same column are significantly different by the Tukey test ($p<0.05$). Standard curves: Acetyl: $y = 0.0003x + 0.0002$ ($R^2 = 0.999$) / Pyruvate: $y = 6.703x + 0.0479$ ($R^2 = 0.957$).

The deacetylation method was efficient for acetate groups removal from natural xanthan, according to the chemical analysis of the acetyl content in Table 2. Infrared spectroscopy results confirm these data (Fig. 2) by the absence of the band at 1710 to 1730 cm^{-1}, related to C=O bond esters axial deformation. The literature reports acetyl values varying from 1.9 and 6.0% for xanthan (García Ochoa et al., 2000).

According to Burdock (1997) the lower limit for pyruvate content in commercial xanthan is 1.5% and García-Ochoa and collaborators(2000) point to values from 1 to 5.7%, the findings of this study being in conformity. Smith and collaborators (1981) established that commercial xanthan gums exhibited variations in the degree of substitution of acetate and pyruvate groups and according to the researches, these variations can be observed between different batches of the same source.

3.3. SEM

Fig. 1 illustrates the morphology of the neat polysaccharides and of the crosslinked mixtures of native manioc starch/deacetylated xanthan.

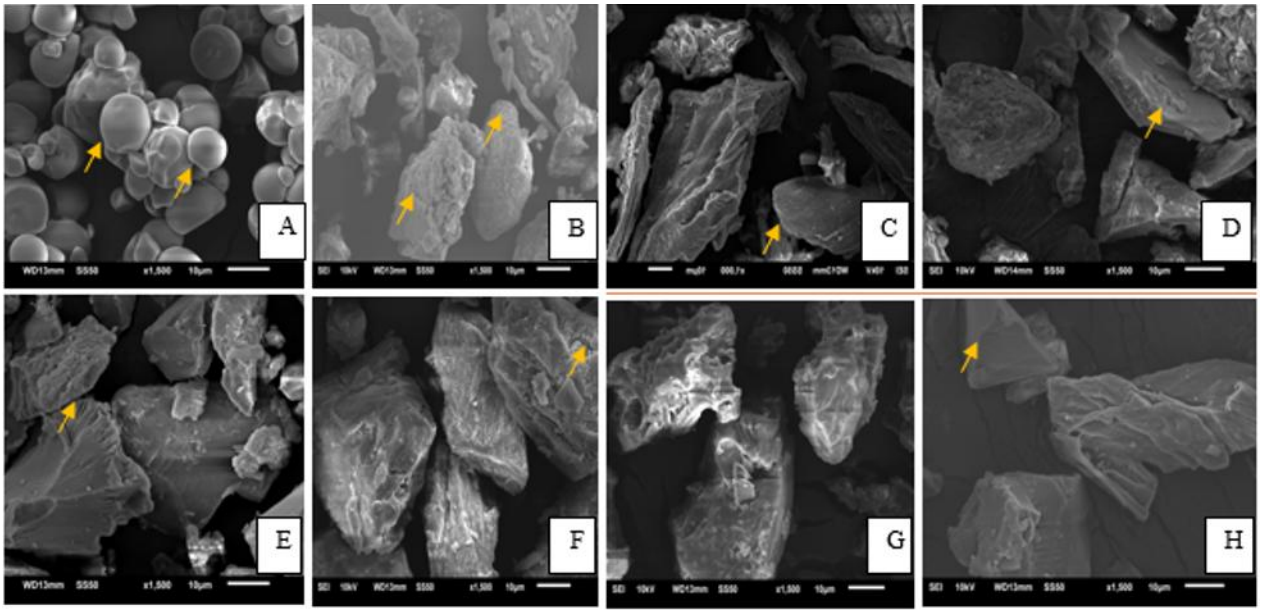

Fig. 1: Scanning Electron Micrography 1500x magnification, for neat polysaccharides and for crosslinked native manioc starch/deacetylated xanthan. (a) native manioc starch; (b) natural xanthan; (c) deacetylated xanthan; (d) T1 (starch 4.5/xanthan 0.5 to 52 min); (e) T3 (starch 4.5/xanthan 0.5 at 127 min): (f) T4 (starch 3.5/xanthan 1.5 at 127 min); (g) T6 (starch 3.3/xanthan 1.7 at 90 min); (h) T12 (starch 4.0/xanthan 1.0 at 90 min).

For native manioc starch (Fig. 1, a) in a characteristic way, granules of varied size could be seen, of predominantly oval shape. According to Rickard, Asaoka & Blashard (1991) native manioc starch has 5-35 μm diameter round, oval, polygonal and cylindrical granules. For natural xanthan fiber remains can be observed (Fig. 1, b) formed during recovery, when the polymer is made insoluble with a non-solvent such as ethyl or isopropyl alcohol (Vendruscolo et al, 2000). Xanthan deacetylation process involves solubilization, treatment and re-insolubilization, with further drying. The withdrawal of acetyl ions caused reduction in repulsion among molecules (Klaic et al, 2016), enabling higher material compaction (Fig. 1, c). As can be observed, crosslinking of the native manioc starch/deacetylated xanthan caused breakage of granule structure (Fig. 1, b-h). For materials originated from crosslinking of mixtures containing lower proportion of xanthan highly compact polygonal structures could also be observed (Fig. 1, d, e, h), which are absent from treatments where xanthan is in higher amount (Fig. 1, f, g). In some cases, it was possible to observe orifices, probably caused by bubbles trapped in the material (Fig. 1, g).

3.4. Infrared

Fig. 2 shows spectra for natural and deacetylated samples (Fig. 2, a), sodium trimetaphosphate (Fig. 2, b), native manioc starch and a few spectra of native manioc starch/deacetylated xanthan crosslinked mixture (Fig. 2, c).

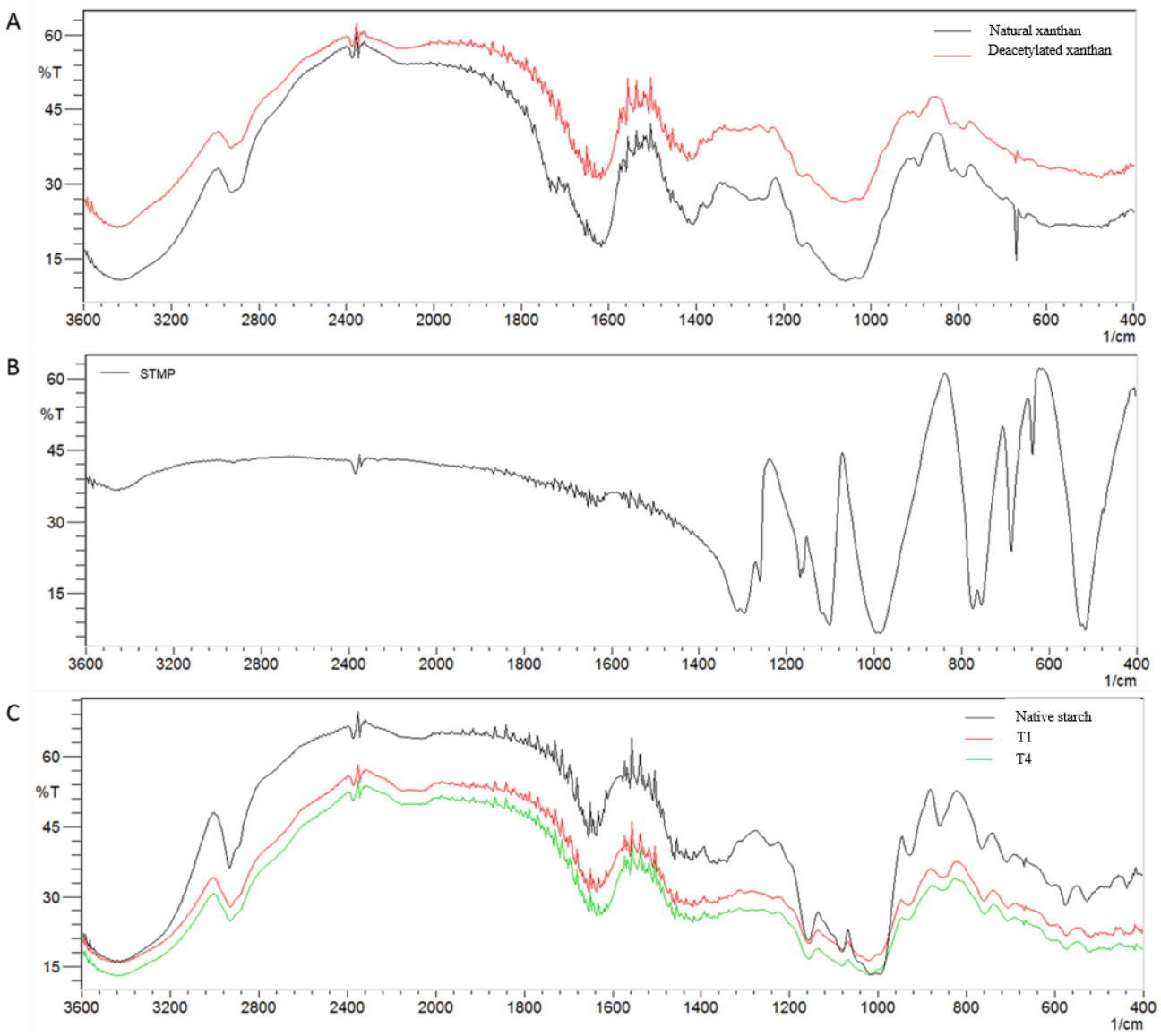

Fig. 2: IR spectra for natural xanthan, deacetylated xanthan (a); SMTP (b); native manioc starch and treatments T1 (starch 4.5/xanthan 0.5; t 52 min) and T4 (starch 3.5/xanthan 1.5; t 127 min) (c) in accordance with the Central Composite Rotatable Design.

Infrared spectroscopy results strengthen those found in the acetyl content chemical analysis (Table 2). The axial deformation of the C=O linking esters is characterized by a band at 1710 to 1730 cm^{-1}(Faria, 2011), normally present in xanthan spectra. This band is however absent in deacetylated xanthan (Fig. 2, a) and in the crosslinked mixtures of native manioc starch/deacetylated xanthan (Fig. 2, c). This result corroborates deacetylation effectiveness. Spectra of crosslinked mixtures of native manioc starch/deacetylated xanthan samples exhibit a strong and large absorption band at 3200 to 3600 cm^{-1}, related to hydroxyl groups (OH), both free and associated through hydrogen bonds, but having lower intensity relative to the controls (native starch and deacetylated xanthan) and at 2931 cm^{-1}, related to the asymmetric stretching of methylene group (CH_2).

The main sign of modification as a function of sodium trimetaphosphate is the insertion of absorption bands in the 1000 to 1200 cm^{-1}region, related to the axial deformation of the methyl esters C-O linkage in the crosslinked mixtures. The accentuated intensities of the bands in the region of 516.92 to 687 $cm^{-1}$are attributed to the vibrational stretching of the phosphorus bridges (O-P-O) and/or (P=O), from 756 to 776 cm^{-1}, related to the (P-O-P) symmetrical stretching. The band at 895 $cm^{-1}$is attributed to the asymmetric vibrational stretching of the P-O-P group, and at the 1210 cm^{-1} region are the bands related to the symmetrical -P=O stretching (Silverstein et al., 2007). The band aspect at 1022 cm^{-1}, related to changes in structural organization, shows that the formed materials are of amorphous character (Li et al., 2009). Phosphate bonds characteristic bands (1210 cm^{-1}) which supposedly occur through STMP insertion to the polymer do not appear in the crosslinked samples spectra, being associated to low crosslinking levels (Li et al., 2009).

3.5. Rheometrical Analyses

In Fig. 3 viscosity curves versus shear stress for native manioc starch, natural and deacetylated xanthan gums and the crosslinked mixtures of native manioc starch and deacetylated xanthan gums can be seen. As a control for the crosslinking process effect, the physical mixtures, without crosslinking obtained by the proportions of starch/xanthan used in T5 and T6 respectively, with the lower and the highest xanthan concentration, were also assessed.

Materials exhibited pronounced differences as regards viscosity and pseudoplasticity. Deacetylated xanthan showed the higher viscosity, while natural xanthan did not correspond to the expectations; native starch, however, was the least viscous material. All crosslinked samples were more viscous than native starch. This is a quite significant result, since in a previous study on starch crosslinking it has been identified that some treatments caused increase in viscosity, while other ones, reduction. The condition used (S 5%; STMP 5%; SS 3%) was the same employed for T1 of the starch crosslinking study, which resulted in a more viscous material than the native manioc starch (Fig. 3) of the previous study.

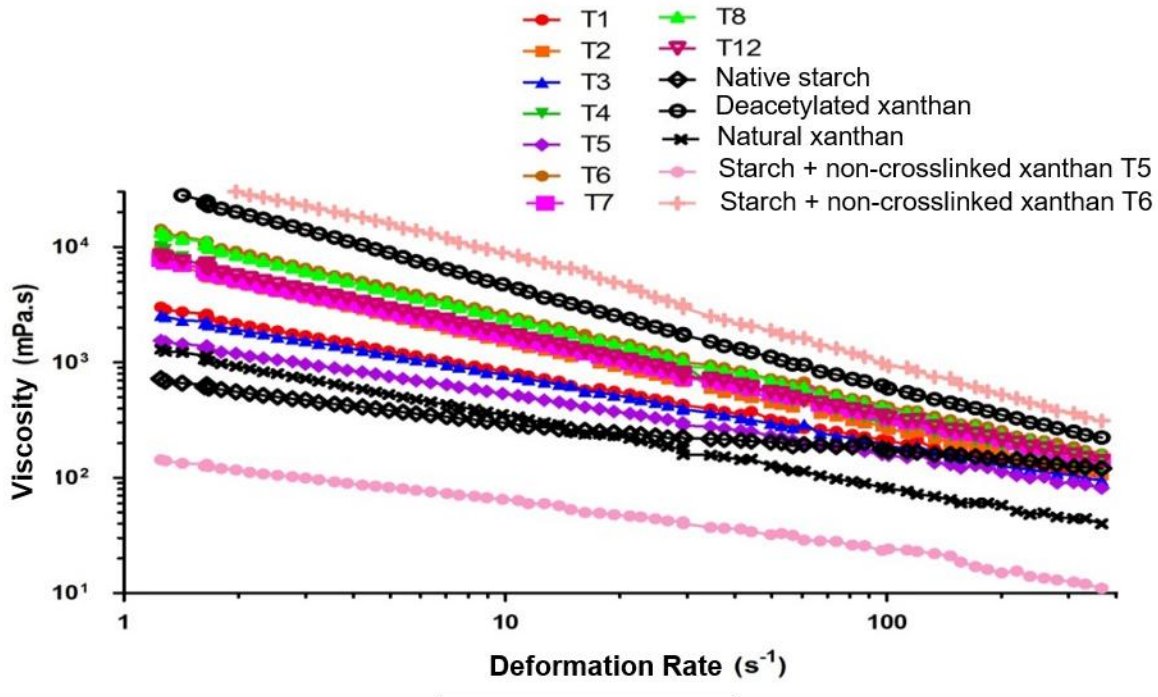

Fig. 3: Filmogenic solution for native and crosslinked manioc starches at 3%, according to the Central Composite Rotational Design (CCRD 2^2).

Table 4 contains the values obtained for parameters *K* and *n* through the Ostwald-de-Waele rheological mathematical model.

Table 4: Effects of the treatments performed on the humidity and the parameters of the Ostwald-de Waele rheological model of the polymers [b] Flow index.

Treatment	Humidity (%)	K[a] (Pa.s^n)	n[b] (non-dimensional)	R^2 [c] (nondimensional)
Native starch	11.983±0.01^{b}	0.69 ± 0.02^{g}	0.68 ± 0.01^{a}	0.999
Natural Xanthan	12.63±0.02^{b}	1.367 ± 0.02^{g}	0.41 ± 0.01^{bc}	0.997
Deacetylated Xanthan	12.010±0.01^{b}	34.4 ± 3.68^{b}	0.12 ± 0.05^{e}	0.999
T1	9.880±0.01^{g}	3.15 ± 0.03^{fg}	0.41 ± 0.01^{bc}	0.998
T2	11.027±0.01^{cd}	9.12 ± 0.87^{de}	0.20 ± 0.08^{de}	0.997
T3	11.333±0.01^{c}	6.29 ± 0.67^{ef}	0.28 ± 0.01^{cd}	0.997
T4	9.343±0.01^{h}	10.43 ± 0.07^{g}	0.13 ± 0.02^{e}	0.995
T5	10.553±0.02^{def}	1.83 ± 0.19^{g}	0.46 ± 0.05^{b}	0.997
T6	10.330±0.03^{efg}	17.26 ± 1.24^{c}	0.16 ± 0.07^{de}	0.995
T7	10.740±0.05^{de}	8.54 ± 0.38^{de}	0.31 ± 0.01^{bcd}	0.999
T8	12.893±0.03^{a}	14.50 ± 0.21^{c}	0.24 ± 0.01^{de}	0.998
T11	10.103±0.01^{fg}	9.16 ± 0.16^{de}	0.29 ± 0.01^{cd}	0.997
Starch + non-crosslinked xanthan T5	*	**	**	**
Starch + non-crosslinked xanthan T6	*	45.347 ± 0.05^{a}	0.30 ± 0.02^{cd}	0.997

[a] Index of Consistency

[b] Flow index.

[c] Coefficient of determination.

Equal letters on the same column mean that there is no significant difference between the treatments for p < 0.0. *Not determined. **Negative Value, not significant

Values for humidity are in accordance with the Regulatory Instruction MAPA n° 23 of December 14, 2005 (BRAZIL, 2005a) which states that it could be up to 14%. ANVISA, according to RDC n° 263 of September 22, 2005 (BRAZIL, 2005b), allows a maximum of 18%. Leonel et al (2009) upon characterizing manioc starch for use in producing extrudates obtained 12.2% humidity. In this study the humidity contents were 12.263% and 12.010% for the natural and deacetylated xanthan gums respectively, higher values than those reported in the literature for commercial xanthan, which normally has a water content of nearly 10% (García-Ochoa et al., 2000), with from 8 to 15% being acceptable (Born et al., 2002; García-Ochoa et al., 2000). As for viscosity, deacetylated xanthan was the most viscous material, being higher than that of natural xanthan. Studies by Khouryieh and collaborators (2007) reported that both the viscosity and the viscoelasticity of the mixtures with

deacetylated xanthan were higher than those with natural xanthan. Authors also attributed the increase in synergistic interaction to deacetylation, due to its contribution to the destabilization of the helicoid structure and consequent disordering of the xanthan molecule.

As relates to native starch, all the manioc native starch/deacetylated xanthan crosslinked mixtures had higher viscosity and pseudoplasticity, corroborated by the higher *K* and *n* values, respectively. Treatments T6 and T8, which combined the higher levels of xanthan and time, respectively, had the higher viscosities, without differing statistically, showing the best results. The lower viscosity was observed for T5, obtained with the lowest xanthan level and time at the central value.

The physical mixtures (without crosslinking) obtained by the starch/xanthan proportions used for T5 and T6, respectively with lower and higher xanthan concentration, presented relevant data. T5 did not present significant data, and T6 had the highest viscosity of this study. This is an important information which deserves to be examined; however, the goal of this study is the polymer mixtures crosslinking, to obtain improved properties, such as WVP and solubility.

Figures for *n* (flow behavior indexes) were lower than the unity (1), which characterizes non newtonian fluids of pseudoplastic behavior, that is, the farther it is from the unity, the higher the pseudoplasticity, characterized by viscosity reduction with increased tensions. This same behavior was observed by López et al (2008) for flow curves of starch filmogenic suspensions.

Treatment T6, which combined the highest xanthan concentration (T6 - S 3.3% and X 1.7%, with 90 min reaction time), resulted in the starch xanthan mixture with the best rheological characterization, higher viscosity.

3.6. Thermal Properties (DSC)

Table 5 shows that both the original polymers and those hybridized by crosslinking had endothermic peaks, and that a huge difference in enthalpy variation could be observed among the samples.

Deacetylated xanthan showed lower melting range, indicating lower polydispersity (REF), and occurred at a temperature (144.18°C) higher than that of the native manioc starch (75.99°C). Therefore, it appears that deacetylation can have a positive effect on xanthan, since Ramasamy and collaborators (2011) determined that commercial xanthan melting temperature is in the range of 90 to 120°C, with an endothermic peak observed at 108.9°C. The same value was found for commercial xanthan by Ahuja et al. (2012). According to Horn et al. (2023), who obtained xanthan under different conditions, xanthan degradation starts around 150°C and ends at 400°C. As for starch, the thermal transition occurred at much lower temperatures, consistent with the lower structural stability of native manioc starch and the absence of crosslinking interactions.

In general terms crosslinking increased melting temperature, comparing to deacetylated xanthan and native manioc starch, but the effect on enthalpy variation was dependent on the time variable. The highest melting temperature was observed for sample T4, submitted to a longer reaction time (127 min), while sample T1, crosslinked under milder conditions (52 min) exhibited lower melting temperature as compared to sample T4.

Table 5: Differential Scanning Calorimetry for deacetylated xanthan, native manioc starch, and a few crosslinked treatments; heating from 30 to 205 ºC at a 10 ºC/min rate; and cooling from 250 ºC to 100 ºC at a 10 ºC/min rate.

Parameters	Deacetylated X.	Native manioc starch	T1	T4
Onset - Tº (ºC)	141.22	33.93	143.74	182.74
Peak-Tp (ºC)	144.18	75.99	146.40	185.41
Endset Tf (ºC)	150.08	106.27	155.33	185.35
ΔT (Tf-T0) (°C)	8.86	72.34	11.59	2.61
Enthalpy variation ΔH ($J.g^{-1}$)	110.35	316.86	86.00	0.67

3.7. Characterization of the films

3.7.1. Macroscopic Properties

Fig. 4 illustrates the aspect of the produced films from crosslinked mixtures of native manioc starch/deacetylated xanthan.

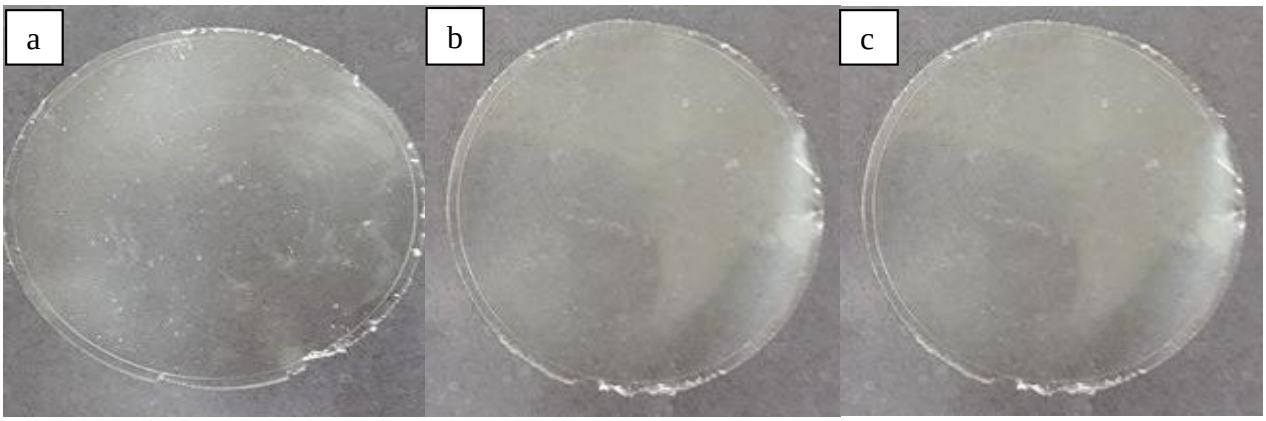

Fig. 4: Films obtained by casting based on a filmogenic solution containing 3% (m/m) of the crosslinked mixture of native manioc starch/deacetylated xanthan and 0.9% glycerol (a) F1 (T1); (b) F4 (T4); (c) F6 (T6).

Films based on the crosslinked mixture of native manioc starch/deacetylated xanthan were excellent as regards homogeneity, handling and continuity. For films of higher xanthan concentration bubbles were formed, since the higher viscosity provides the imprisonment of same.

Thickeners are commonly used as stabilizers for aerated systems (Damodaran et al., 2010). Films had also fair transparency and gloss.

3.7.2. SEM

Fig. 5 illustrates the aspect of films prepared with the crosslinked mixture of native manioc starch/deacetylated xanthan.

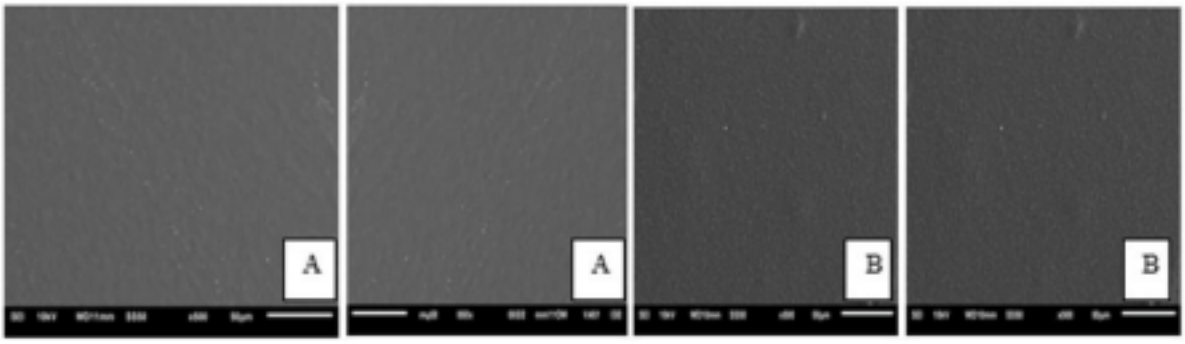

Fig. 5: Films prepared with the native manioc starch/deacetylated xanthan mixture of treatments 1 (a) and 4 (b).

Aiming at observing and analyzing possible roughness and flaws SEM measurements were performed. Fig. 5 illustrates the micrographs for different films of the crosslinked mixture of native manioc starch/deacetylated xanthan. In comparison with films obtained from crosslinked starches, as reported in the previous study, addition of xanthan to starch previously to crosslinking provided more homogeneous films. The surfaces of the crosslinked films do not have pores nor cracks. Xanthan or starch granules were not observed, those being completely solubilized. The films were continuous and homogeneous. Similar results were reported by Henrique et al. (2008), who compared the micrographs of commercial crosslinked starch films to other three different kinds of modified starches.

3.7.3. Physical and chemical properties

Table 6 lists the results of the experiment, for the two assessment periods, obtained by applying the second order Central Composite Rotational Design (CCRD 2^2) based on the response surface methodology (RSM) employed to assess the effect of crosslinking on the mixture of native manioc starch/deacetylated xanthan, and of the reaction time on the physical and chemical properties of the edible films obtained.

Table 6: Experimental CCRD 2^2 planning matrix, with codified and actual levels, and values of the variable responses obtained for the films Independent Variables Dependent Variables

Treatments	Independent Variables		Dependent Variables					
	Starch + Xanthan (%)	Time (min)	Solubility (%)	WVP	Thickness	Opacity	Tensile strength (Mpa)	Elongation (%)
1	-1 (4.5 + 0.5)	-1 (52)	17.96	7.16	0.099	10.69	12.33	29.08
2	+1 (3.5 + 1.5)	-1 (52)	19.05	9.50	0.104	10.7	10.67	7.7
3	-1 (4.5 + 0.5)	+1 (127)	12.21	11.52	0.125	10.95	7.58	25.08
4	+1 (3.5 + 1.5)	+1 (127)	12.13	8.42	0.099	10.52	13.04	10.08
5	-α (4.7 + 0.3)	0 (90)	16.19	8.13	0.114	10.66	5.62	34.42
6	+α (3.3 + 1.7)	0 (90)	14.70	8.66	0.097	10.47	10.33	4.58
7	0 (4.0 + 1.0)	-α (37)	15.86	9.89	0.137	9.91	5.92	13.58
8	0 (4.0 + 1.0)	+α (142)	17.78	10.11	0.126	13.54	6.54	3.17
9	0 (4.0 + 1.0)	0 (90)	18.67	7.22	0.107	12.45	8.57	12.67
10	0 (4.0 + 1.0)	0 (90)	18.60	8.02	0.107	11.54	7.34	9.83
11	0 (4.0 + 1.0)	0 (90)	18.44	7.90	0.109	11.27	7.86	14.58

For the dependent variables, solubility, opacity and tensile strength, the effects were not so statistically significant within the studied ranges, as well as it has not been possible to generate predictive models for these analyses, as well as demonstrate the respective response surfaces.

The best solubility results were obtained at F1 (T1 – 4.5 starch + 0.5 xanthan) and F4 (T4 – 3.5 starch + 1.5 xanthan), where F1 combined the lower WVP value (7.16%) and low solubility (17.96%), poor thickness (0.099mm) and low xanthan concentration (0.5%), which would imply in lower process cost for the industrial application. F4 also revealed itself as efficient, since it had the lowest solubility value (12.13%) and one of the lowest WVP values (8.42%) and thickness (0.099 mm), this set of properties being very positive for obtaining edible packaging films.

For the tensile strength analysis, the proportion of native manioc starch/deacetylated xanthan, its interaction with time influenced the results, however time per se did not show effect in this response. For the opacity results, independent variables did not produce any effects.

For the dependent variables, WVP, thickness and elongation, significant and predictive mathematical models were generated, with 95% confidence and coefficients of determination (R^2) 0.90, 0.72 and 0.93, respectively. Based on statistical analysis, the significant regression coefficients at 95% were considered in the mathematical models proposed to represent Equations 1 (WVP), 2 (Thickness) and 3 (Elongation) for the films, as a function of the percentage of xanthan and starch (XS) and reaction time (T). See below Equations 3, 4 and 5:

$$WVP = \mathbf{7.71} - 0.003\times XS + 0.66\times XS^2 + 0.90\times T + 2.27\times T^2 - 2.72\times XS\times T \quad (3)$$

$$Espessura = 0.11 - 0.01\times XS - 0.008\times XS^2 + 0.001\times T + 0.018\times T^2 - 0.016\times XS\times T \quad (4)$$

$$Elongação = 12.34 - 19.68\times XS + 9.23\times XS^2 - 4.08\times T - 1.97\times T^2 + 3.20\times XS\times T \quad (5)$$

The response surfaces and contour plots for the analyses of films based on the model generated by Equations 3, 4 and 5 are respectively illustrated in Figures 8, 9 and 10.

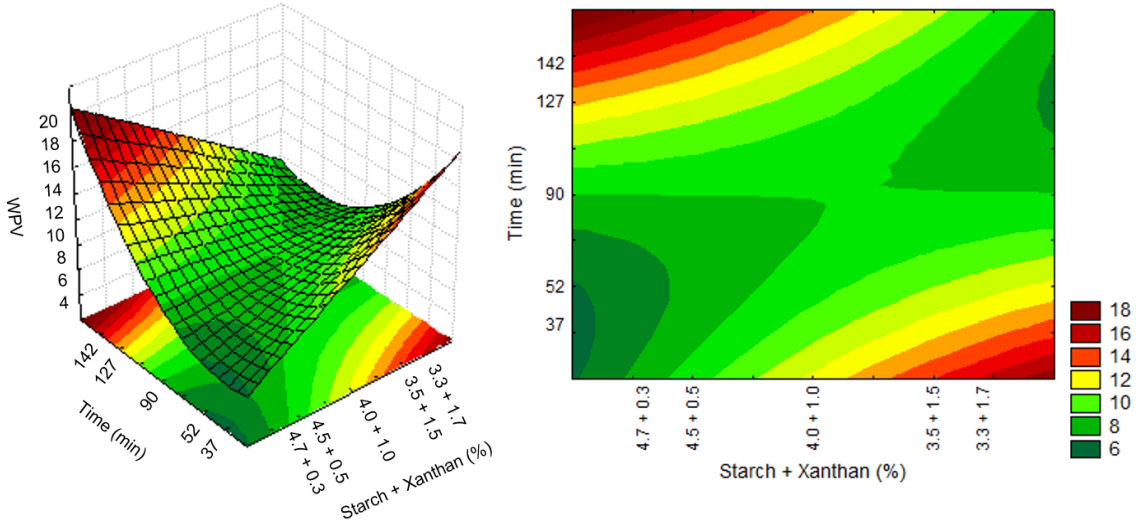

Fig. 8: Response surfaces and contour plots as a function of starch and xanthan proportion and time, related to the WVP analysis.

No significant effect of the native manioc starch/deacetylated xanthan crosslinked mixture related to water vapor permeability (WVP) could be observed, it being evidenced only when combined with time. However, reaction time had significant effect per se. Increased xanthan concentration in the treatments provides superior WVP results as can be observed for the contour plot (Fig. 8).

Matta et al. (2011), assessed biofilms obtained from pea starch associated with xanthan gum and glycerol, and found solubility values between 3.14 and 18.19%. In this study the values obtained were between 12.13 and 17.96%.

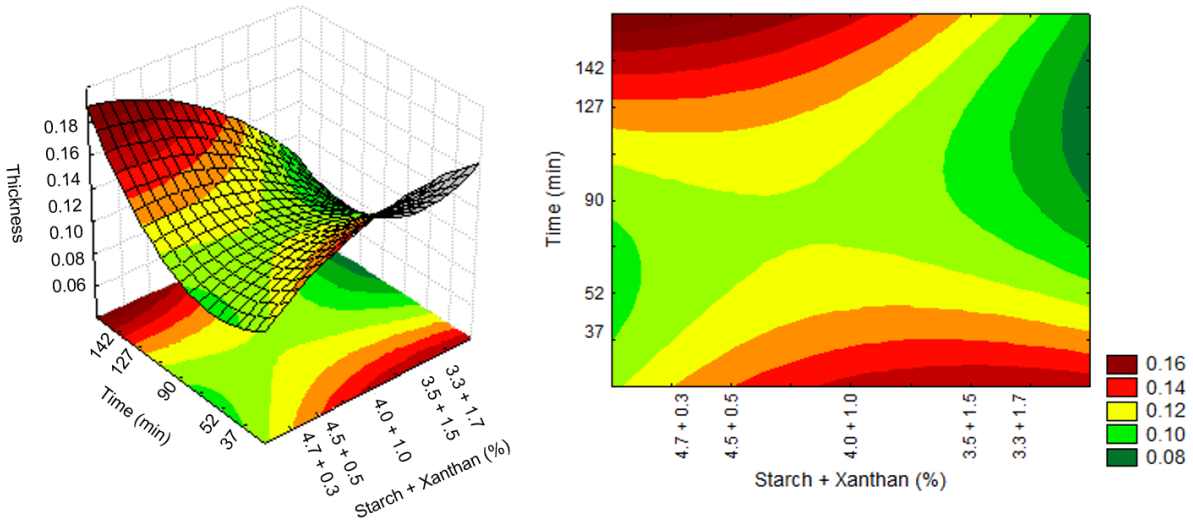

Fig. 9: Response surfaces and contour plots as a function of the starch and xanthan percentage and time, related to thickness analysis.

For thickness all the variables had a significant effect, with values between 0.097 and 0.137 mm. According to Embuscado & Huber (2009) in general biodegradable films thickness is lower than 0.300 mm, this being a main physical feature, since in their use as packaging the type, volume and weight of the food to be stored should be considered. According to the contour plot (Fig. 9) increase in film thickness can be seen as far as xanthan concentration is increased and starch concentration in the mixture is reduced. Silva (2011) found thickness values lower to those obtained in this study for biofilms produced with native pine nuts starch (0.11 mm). Biofilms produced by Matta et al. (2011) with pea starch and xanthan showed thickness variation from 0.055 and 0.098 mm.

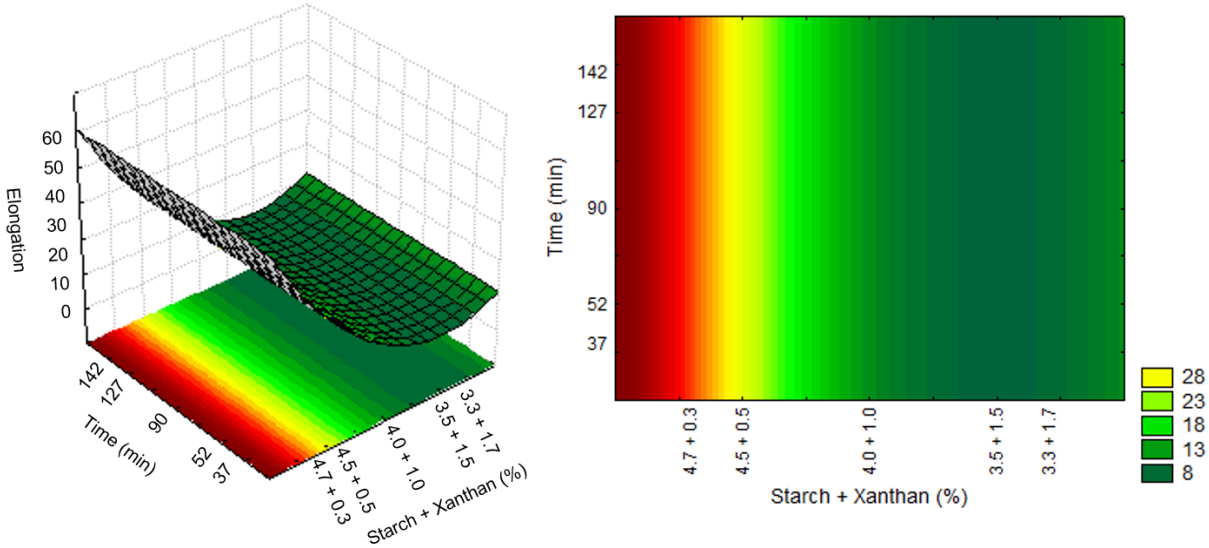

Fig. 10: Response surfaces and contour plots as a function of starch and xanthan percentages, related to elongation analysis.

For elongation analysis time did not show any effect on the results, only the starch/xanthan concentration, with values between 3.17 to 34,42%. It could be seen that the increase in xanthan concentration, combined with reduction in starch concentration caused reduced film elongation.

IV. CONCLUSIONS

Deacetylation resulted in significant increase in xanthan viscosity. Deacetylation and crosslinking were corroborated by absence of the band at 1710 to 1730 cm^{-1}, related to C=O bond esters axial deformation and appearance of bands in the 1000 to 1200 cm^{-1}region, related to the axial deformation of the methyl esters C-O linkage in the crosslinked mixtures, respectively.

Crosslinking variables polymers starch/xanthan proportion and reaction time influenced the hybrid materials – powders and films - properties, which was corroborated by rheological, thermal, SEM and IR analyses. Favorably, crosslinking increased viscosity and melting temperature. Higher proportions of xanthan and reaction time caused increase in melting temperature and reduction in enthalpy variation.

Films prepared from native manioc starch crosslinked with deacetylated xanthan hybrid polymers exhibited excellent results as for macroscopic characteristics, low opacity, low humidity, WVP and solubility. T1, obtained at level -1 of reaction time, combined the lower WVP with low solubility, small thickness and the second higher tensile strength with, favorably, low amount of xanthan, which lowers the industrial application process cost. T4 was also efficient, since it had the lowest solubility and one of the lowest WVP value and thickness and higher tensile strength, this set of properties being very positive for preparing edible packaging films.

4.1 CRediT authorship contribution statement

Marisa Karow: Writing – original draft, Visualization, Validation, Methodology, Investigation. Karine Macagnan: Writing – original draft, Visualization, Data curation. Mariane Alves: Writing – original draft, Visualization. Patrícia Diaz: Project administration, Conceptualization. Lígia Furlan: Writing – review & editing. Claire Vendrucolo: Project administration, Funding acquisition, Conceptualization. Angelita Moreira: Writing – review & editing, Funding acquisition, Conceptualization, Supervision.

4.2 Declaration of competing interest

The authors declare that they have no known competing financial interests or personal relationships that could have appeared to influence the work reported in this paper.

ACKNOWLEDGEMENTS

The authors also thank the CAPES and CNPq funding agencies for financial support.

REFERENCES

1. Ahuja, M., Kumar, A., & Singh, K. (2012). Synthesis, characterization and in vitro release behavior of carboxymethyl xanthan. *International Journal of Biological Macromolecules*, *51*(5), 1086 - 1090.
2. AOAC- Association of Official Analytical Chemists. (2012). *Official methods of analysis of Association of Official Analytical Chemists International*. (19 ed.) Gaithersburg. ASTM D

882-12. (2012) Standard Test Method for Tensile Properties of Thin Plastic Sheeting. *ASTM International*, West Conshohocken, PA.
3. ASTM F2251-13. (2013). Standard Test Method for Thickness Measurement of Flexible Packaging Material. *ASTM International*, West Conshohocken, PA.
4. Bejenariu, A., Popa, M., Dulong, V., Picton, L., & Cerf, D. (2009). Trisodium trimetaphosphate cross-linked xanthan networks: synthesis, swelling, loading and releasing behavior. *Polymer Bulletin*, *62*, 525–538.
5. Borges, C. D., Mendonça, C. R. B., Zambiazi, R. C., Nogueira, D., Pinto, E. M., Paiva, F. F. (2013). Strawberries conservation with coatings based on xanthan gum and sage essential oil. *Bioscience Journal*, 29(05), 1071-1083.
6. Born, K., Langendorff, V., & Boulenguer, P. Xanthan. In: Steinbüchel, A., Vandamme, E. J., & de Baets, S. (2002). *Biopolymers*. (5 ed.) Weinheim: Wiley-VCH, (p. 259-291). Brasil. (2005a). Ministério da Agricultura, Pecuária e abastecimento. MAPA. *Instrução Normativa nº 23 de 14 de dezembro de 2005, aprova o regulamento técnico de identidade e qualidade dos produtos amiláceos derivados da raiz de mandioca*. Available at: http://www.e legis.anvisa.gov.br. Accessed on: August 25, 2015.
7. Brasil. (2005b). Ministério da Saúde. Agência Nacional de Vigilância Sanitária (ANVISA). Resolução RDC n. 263, de 22 de setembro de 2005. *Aprova o regulamento técnico para produtos de cereais, amidos, farinhas e farelos*. Available at: http://www.e-legis.anvisa.gov.br. Accessed on: August 25, 2015.
8. Burdock, G. A. (1997). *Encyclopedia of Food and Color Additives*. (3 ed.) New York: CRC Press, (p. 3153).
9. Chaisawang, M., & Suphantharika, M. (2006). Pasting and rheological properties of native and anionic tapioca starches as modified by guar gum and xanthan gum. *Food Hydrocolloids*, *20*(5), 641-649.
10. Cortez-Veja, W. R., Piotrowicz, I. B. B., Prentice, C., & Borges C. D. (2013). Conservação de mamão minimamente processado com uso de revestimento comestível à base de goma xantana. *Semina: Ciências Agrárias*, *34*(4), 1753-1764.
11. Damodaran, S., Parkin, K. L., & Fennema, O. R. (2010). *Química de Alimentos de Fennema*. (4 ed.) Porto Alegre: Artmed, (p. 900).
12. Demiate, I. M., Dupuy, N., Huvenne, J. P., CEREDA, M. P., & WOSIACKI, G. (2000). Relationship between baking behavior of modified cassava starches and starch chemical structure determined by FTIR spectroscopy. *Carbohydrate Polymers*, *42*(2), 149-158. El-Rhouttais, C., Elfazazi, K., Kettabi, Z. E., Laaraj, S., Elgoulli, M., Al-Zharani, M., Nasr, F. A., Qurtam, A. A., Bouslihim, Y., & Salmaoui, S. (2025). Effect of Xanthan gum-based edible coating enriched with cloves and cinnamon for extending the shelf-life of pomegranate fruit during cold storage. *Scientific Reports*, *15*(1), 31518.
13. Embuscado, M. E., & Huber, K. C. (2009). *Edible films and coatings for food applications*. Nova Yorque: Springer, (p. 403).
14. Erten, T., Adams, G. G., Foster, T. J., & Harding, S. E. (2014). Comparative heterogeneity, molecular weights and viscosities of xanthans of different pyruvate and acetate contente. *Food Hydrocolloids*, *42*(3), 335-341.
15. FAO - Food and Agriculture Organization Of The United Nations. FAOSTAT. (2014). *Production*. Available at: http:// www.faostat.fao.org. Accessed on: July 28, 2015. Faria, S., Petkowicz, C. L. O., Morais, S. A. L. M., Terrones, G. H., Resende, M. M., França, F. P., & Cardoso, V. L. (2011). Characterization of xanthan gum produced from sugar cane broth. *Carbohydrate Polymers*, *86*, 469 - 476.
16. FDA - Food And Drug Administration. (2007). *Food starch modified: code of federal regulation*. Washington, *3*.

17. Fonseca, L. M., Gonçalves, J. R., Halal, S. L. M., Pinto, V. Z., Dias, A. R. G., Jacques, A. C., & Zavareze, E. R. (2015). Oxidation of potato starch with different sodium hypochlorite concentrations and its effect on biodegradable films. *LWT- Food Science and Technology*, *60*, 714–720.
18. Freitas, I. R., Cortez-Veja, W. R., Pizato, S., Prentice-Hernández, C., & Borges, C. D. (2013). Xanthan gum as a carrier of preservative agentes and calcium chloride applied on fresh-cut apple. *Journal Food Safety*, 33(3), 229-238.
19. García-Ochoa, F., Santos, V. E., Casas, J. A., & Gómez, E. (2000). Xanthan gum: production, recovery and properties. *Biotechnology Advances*, *18*(7), 549-579.
20. Gontard, N., Guilbert, S., & Cuq, J. L. (1992). Edible wheat gluten films: influence of the main process variables on film properties using response surface methodology. *Journal of Food Science*, 57(1), 190-199.
21. Henrique, C. M., Cereda, M. P., & Sarmento, S. B. S. (2008). Características físicas de filmes biodegradáveis produzidos a partir de amidos modificados de mandioca. *Ciência e Tecnologia de Alimentos*, *28*(1), 231-240.
22. Horn, M. M., Martins, V. C. A., & Plepis, A. M. G. (2023). Effect of Amylopectin Content on Mechanical, Barrier and Thermal Properties of Plasticized Starch/Chitosan Films. *Polysaccharides*, *4*, 208-218.
23. Hunterlab. (1997). *The color management company*. Universal software, version 3.2. Reston. Jain, A. K., Khar, R. K., Ahmed, F. J., & Diwan, P. V. (2008). Effective insulin delivery using starch nanoparticles as a potential trans-nasal mucoadhesive carrier. *European Journal of Pharmaceutics and Biopharmaceutics, 69*(2), 426-435.
24. Jangchud, A., & Chinnan, M. S. (1999). Peanut protein film as affected by drying temperature and ph of film forming solution. *Journal of Food Science*, *64*, 153–157.
25. Karow, M. F., Macagnan, K. L., Alves, M. I., Fioravante, J. B., Rodrigues, R. S., Furlan, L., de Souza, J. F. C., Vendruscolo, C. T., & Moreira, A. da S. (2025). Investigations on the effect of sodium trimetaphosphate and sodium sulfate concentrations on the properties of cross-linked cassava starch films. *Química Nova, 48*(5).
26. Khouryieh, H. A., Herald, T. J., Aramouni, F., Bean, S., & Alavi, S. (2007). Influence of deacetylation on the rheological properties of xanthan–guar interactions in dilute aqueous solutions. *Journal of Food Science*, *72*(3), 173-181.
27. Klaic, P. M. A., Nunes, A. M., Moreira, A. S., Vendruscolo, C.T., & Ribeiro, A. S. (2011). Determination of Na, K, Ca and Mg in xanthan gum: Sample treatment by acid digestion. *Carbohydrate Polymers*, *83*, 1895–1900.
28. Lecorre, D., Bras, J., & Dufresne, A. (2012). Influence of native starch's properties on starch nanocrystals thermal properties. *Carbohydrate Polymers*, *87*(1), 658– 666. Leonel, M., Freitas, T. S., & Mischan, M. M. (2009). Physical characteristics of extruded cassava starch. *Scientia Agricola*, *66*, 486-493.
29. Li, B., Wang, L., Li, D., Adhikari, B., & Mao, Z. (2012). Preparation and characterization of crosslinked starch microspheres using a two-starge water-in-water emulsion method. *Carbohydrate Polymers*, *88*, 912-196.
30. Li, B., Wang, L., Li, D., Chiu, Y.L., Zhang, Z., Shi, J., Chen, X.D., & Mao, Z. (2009). Physical properties and loading capacity of starch-based microparticles crosslinked with trisodium trimetaphosphate. *Journal of Food Engineering*, *92*, 255-260.
31. Limberger, V. M., Silva, L. P., Emanuelli, T., Comarela, C. G., & Patias, L. D. (2008). Modificação química e física do amido de quirera de arroz para aproveitamento na indústria de alimentos. *Química Nova, 31*(1), 84-88.
32. López, O. V., Garcia M. A., & Zaritzky, N. E. (2008). Film forming capacity of chemically modified corn starches. *Carbohydrate Polymers*, *73*, 573-581.

33. Luvielmo, M. M., & Scamparini, A. R. P. (2009). Goma xantana: produção, recuperação, propriedades e aplicação. *Estudos Tecnológicos, 5*(1), 50–67.
34. Matta JR, M. D., Sarmento, S. B. S., Sarantopoulos, C. I. G. L., & Zocchi, S. S. (2011). Propriedades de barreira e solubilidade de filmes de amido de ervilha associado com goma xantana e glicerol. *Polímeros*, *21*(1), 67-72.
35. McComb, E. A., & McCready, R. M. (1957). Determination of acetyl in pectin and in acetylated carbohydrate polymers. *Analytical Chemistry*, *29*(5), 819-821.
36. Medeiros, B. G. S., Pinheiro, A. C., Teixeira, J. A., Vicente, A. A., & Cunha, M. G. C. (2012). Polysaccharide/protein nanomultilayer coatings: Construction, characterization and evaluation
37. of their effect on “rocha” pear (*Pyrus communis* L.) Shelf-life. *Food and Bioprocess Technology, 2*(5), 2435-2445.
38. Nsengiyumva, E. M., & Alexandridis, P. (2022). Xanthan gum in aqueous solutions: Fundamentals and applications. *International Journal of Biological Macromolecules*, *216*, 583-604.
39. Pinto, E. P., Furlan, L., & Vendruscolo, C. T. (2011). Chemical Deacetylation Natural Xanthan (Jungbunzlauer®). *Polímeros*, *21*(1), 47-52.
40. Pizato, S., Cortez-Vega, W. R., de Souza, J. T. A., Prentice-Hernández, C., & Borges, C. D. (2013). Effects of different edible coatings in physical, chemical and microbiological characteristics of minimally processed peaches (*Prunus persica* (*L.*) *Batsch*). *Journal of Food Safety*, *33*(1), 30-39.
41. Pongsawatmanit, R., & Srijunthongsiri, S. (2008). Influence of xanthan gum on rheological properties and freeze–thawstability of tapioca starch. *Journal of Food Engineering*, *88*, 137-143. Ramasamy, T., Kandhasami, U. D. S., Ruttala, H., & Shanmugam, S. (2011). Formulation and evaluation of xanthan gum based aceclofenac tablets for colon targeted drug delivery. *Brazilian Journal of Pharmaceutical Sciences*, *47*(2), 301-311.
42. Rickard, J. E., Asaoka, M., & Blashard, J. M. V. (1991). The physicochemical properties of cassava starch. *Tropical Science, 31*, 189-207.
43. Sandhu, K. S., Kaur, M., Singh, N., & Lim, S. T. A. (2008). Comparison of native and oxidized normal and waxy corn starches: Physicochemical, thermal, morphological and pasting properties. *LWT - Food Science and Technology*, *41*(6), 1000–1010.
44. Shalviri, A., Liu, Q., Abdekhodaie, M. J., & Wua, X. Y. (2010). Novel modified starch–xanthan gum hydrogels for controlled drug delivery: Synthesis and characterization. *Carbohydrate Polymers*, *79*(4), 898-907.
45. Silva, E. M. (2011). Produção e caracterização de filmes biodegradáveis de amido de pinhão. Undergraduate thesis. Department of Chemical Engineering, Federal University of Rio Grande do Sul, Porto Alegre. Available at: https://lume.ufrgs.br/bitstream/handle/10183/38562/000823833.pdf?sequence=1. Accessed on: August 15, 2025.
46. Silverstein, R. M., Webster, F. X., & Kiemle, D. J. (2007). *Identificação Espectrométrica de compostos orgânicos*. Rio de Janeiro, RJ. LTC.
47. Sloneker, J. H., & Orentas, D. G. (1962). Pyruvic acid, a unique component of an exocellular bacterial polysaccharide. *Nature*, *194*, 478-479.
48. Smith, I. H., Symes, K. C., Lawson, C. J., & Morris, E. R. (1981). Influence of the pyruvate content of xanthan on macromolecular association in solution. *International Journal of Biological Macromolecules*, *3*(2), 129-134.
49. Soares, G. A., Castro, A. D., Cury, B. S. F., & Evangelista, R. C. (2013). Blends of cross-linked high amylose starch/pectin loaded with diclofenac. *Carbohydrate Polymers*, *91*, 135-142. Teng, Z., Huang, X., Zhang, C., Liu, X., Li, Y., Wang, C. S., Liu, X., & Xie, F. (2025). Xanthan gum modulation of octenyl succinic anhydrate starch-based high internal phase emulsions: Characterization, rheological behavior, and 3D printing applications. *Food Chemistry*, *464*(3), 141813.

50. Vendruscolo, C. T., Moreira, A. S., Souza, A. S., Zambiazi, R., & Scamparini, A. R. P. (2000). Heteropolysaccharide produced by *Xanthomonas campestris* pv pruni C24. In: Nishinari, K. *Hydrocolloids*, *1*, 187-191.
51. Villela, K. S. V., Araujo, K. V. A., Casillas, P. E. G., & González, C. C. (2024). Protective Encapsulation of a Bioactive Compound in Starch-Polyethylene Glycol-Modified Microparticles: Degradation Analysis with Enzymes. *Polymers (Basel)*, *16*(14), 2075. Wang, S., & Copeland, L. (2015). Effect of Acid Hydrolysis on Starch Structure and Functionality: A Review. *Critical Reviews in Food Science and Nutrition*, *55*(8), 1081-1097. Weber, F. H., Clerici, M. T. P. S., Collares-Queiroz, F. P., & Chang, Y. K. (2009). Interaction of guar and xanthan gums with starch in the gels obtained from normal, waxy and high-amylose corn starches. *Starch/Stärke*, *61*, 28-34.
52. Wurzburg, O. B. (1986). In: *Modified Starches: Properties and Uses*. Wurzburg, O. B., CRC Press: Boca Raton, (p. 97-103).
53. Zamudio-Flores, P. B., Torres, A. V., Salgado-Delgado, L., & Bello-Péres, L. A. (2010). Influence of the oxidation and acetylation of banana starch on the mechanical and water barrier properties of modifies starch and modified starch/chitosan blend films. *Journal of Applied Polymer Science*, *115*, 991-998.
54. Zavareze, E. D. R., Pinto, V. Z., Klein, B., Halal, S. L. M., Elias, M. C., Prentice-Hernández, C., & Dias, A. R. G. (2012). Development of oxidised and heat–moisture treated potato starch film. *Food Chemistry, 132*(1), 344–350.
55. Zóia, D. (2011). Dossiê gomas: As gomas exudadas de plantas. *Revista Food Ingredients Brasil, 1*(17), 28-46.

Zero-Knowledge and Post-Quantum Signature Primitives for Privacy-Preserving Blockchain IoT Systems

Godfrey Wandwi

Salaam Tumaini University

ABSTRACT

Security and privacy have emerged as paramount concerns in the evolving Internet of Things (IoT) ecosystem, where billions of interconnected devices exchange sensitive data over untrusted networks. Traditional cryptographic methods, while effective, are increasingly vulnerable to emerging computational threats, including those posed by quantum computing. This study proposes an enhanced blockchain-based framework that integrates zero-knowledge proofs (ZKPs) and post-quantum signature primitives to achieve robust, privacy-preserving authentication in IoT systems. The framework enables IoT devices to verify transactions and authenticate identities without revealing confidential information, thereby maintaining data confidentiality and integrity. By employing lattice-based and hash-based post-quantum algorithms, the system ensures resistance against quantum attacks while preserving computational efficiency for resource-constrained IoT nodes. By employing lattice-based and hash-based post-quantum algorithms (such as CRYSTALS-DILITHIUM and SPHINCS+), the system ensures resistance against quantum attacks while preserving computational efficiency for resource-constrained IoT nodes.

Keywords: zero-knowledge proofs, post-quantum cryptography, blockchain, iot security, privacy preservation.

Classification: LCC Code: QA76.9.A25, TK5105.59, QA76.9.D32

Language: English

Great Britain Journals Press

LJP Copyright ID: 925615
Print ISSN: 2631-8490
Online ISSN: 2631-8504

London Journal of Research in Science: Natural & Formal

Volume 25 | Issue 13 | Compilation 1.0

Zero-Knowledge and Post-Quantum Signature Primitives for Privacy-Preserving Blockchain IoT Systems

Godfrey Wandwi

ABSTRACT

Security and privacy have emerged as paramount concerns in the evolving Internet of Things (IoT) ecosystem, where billions of interconnected devices exchange sensitive data over untrusted networks. Traditional cryptographic methods, while effective, are increasingly vulnerable to emerging computational threats, including those posed by quantum computing. This study proposes an enhanced blockchain-based framework that integrates zero-knowledge proofs (ZKPs) and post-quantum signature primitives to achieve robust, privacy-preserving authentication in IoT systems. The framework enables IoT devices to verify transactions and authenticate identities without revealing confidential information, thereby maintaining data confidentiality and integrity. By employing lattice-based and hash-based post-quantum algorithms, the system ensures resistance against quantum attacks while preserving computational efficiency for resource-constrained IoT nodes. By employing lattice-based and hash-based post-quantum algorithms (such as CRYSTALS-DILITHIUM and SPHINCS+), the system ensures resistance against quantum attacks while preserving computational efficiency for resource-constrained IoT nodes. Experimental evaluation demonstrates the feasibility of the proposed model in reducing communication overhead and enhancing trust among devices in decentralized networks, where trust is quantified through transaction validation success rates and privacy preservation metrics, achieving an average transaction latency below 1.2 s and proof generation times under 300 ms on constrained IoT nodes. This research underscores the significance of combining zero-knowledge and post-quantum cryptography to build future-proof, privacy-preserving blockchain IoT systems capable of withstanding next-generation security threats.

Keywords: zero-knowledge proofs, post-quantum cryptography, blockchain, iot security, privacy preservation.

Author: Dar es Salaam Tumaini University, Department of Digital Technologies and Information Science, Dar es Salaam, Tanzania.

I. INTRODUCTION

The rapid proliferation of Internet of Things (IoT) devices has led to an unprecedented level of data exchange across heterogeneous networks, yet it simultaneously magnifies vulnerabilities associated with privacy breaches and unauthorized access. IoT devices, ranging from wearable sensors to industrial controllers, often operate over untrusted or partially trusted networks, making conventional cryptographic methods increasingly insufficient to guarantee data confidentiality and user privacy (Gajjela et al, 2018). In addition, the looming threat of quantum computing presents an existential challenge to traditional digital signatures and public-key cryptosystems, which rely on computational hardness assumptions vulnerable to quantum algorithms such as Shor's (Vairagade e al, 2025).

London Journal of Research in Science: Natural & Formal

However, blockchain alone does not inherently preserve user privacy. Transaction metadata and public ledger visibility can still expose sensitive information, which is particularly critical in sectors like healthcare, finance, and industrial automation, where device interactions may reveal behavioral patterns or operational secrets (Vaghani, 2024). Several privacy-enhancing techniques have been proposed to mitigate these issues, including zero-knowledge proofs, ring signatures, and mixing protocols, which obfuscate transaction origins or conceal user identities on public blockchains. While these approaches have shown promise in enhancing anonymity and confidentiality, their computational complexity and scalability limitations often hinder their suitability for resource-constrained IoT environments. It is also important to distinguish between public and private (permissioned) blockchain environments when designing privacy-preserving IoT solutions. Public blockchains emphasize transparency and global consensus, which may inadvertently conflict with IoT data confidentiality requirements. In contrast, permissioned blockchains, often employed in industrial and enterprise IoT deployments, provide controlled access and governance but still demand robust privacy mechanisms to prevent internal data leakage. The proposed framework aligns with the latter model, emphasizing privacy and verifiable security in decentralized yet permissioned IoT ecosystems

Zero-Knowledge Proofs (ZKPs) offer a promising solution in this context, enabling devices to demonstrate possession of certain information without revealing the information itself. By incorporating ZKPs into blockchain-enabled IoT systems, devices can authenticate transactions and prove integrity while concealing sensitive data, thereby mitigating privacy leakage and enhancing trust among decentralized peers (Yang et al, 2021). Nevertheless, the integration of ZKPs into resource-constrained IoT devices introduces challenges related to computational overhead, latency, and energy consumption, necessitating lightweight and optimized constructions suitable for low-power environments (Sundar et al, 2019).

Complementing ZKPs, post-quantum cryptography (PQC) provides resilient signature primitives that withstand attacks from adversaries equipped with quantum computational capabilities. Lattice-based, hash-based, and code-based signature schemes have shown promise in delivering security without sacrificing performance, even on devices with limited memory and processing capacity. Integrating PQC into blockchain IoT frameworks ensures forward-looking protection, mitigating the risk posed by emerging quantum threats while maintaining transaction verifiability and integrity (Jenkins & Smith, 2000).

This study proposes a comprehensive framework that combines zero-knowledge proofs with post-quantum signature primitives to establish privacy-preserving, quantum-resistant blockchain IoT systems. The framework focuses on three critical objectives: safeguarding device-generated data from unauthorized disclosure, ensuring secure authentication and transaction verification under decentralized conditions, and maintaining computational feasibility for constrained IoT nodes. By experimentally evaluating the framework under realistic IoT network scenarios, including heterogeneous device capabilities and adversarial interactions, this research highlights the feasibility and practical benefits of deploying ZKP- and PQC-enabled blockchain architectures.

The contributions of this work are multi-fold. First, it demonstrates a pathway to integrate advanced cryptographic primitives into IoT devices without incurring prohibitive computational overhead. Second, it provides a blueprint for combining privacy-preserving proofs with post-quantum resilience, ensuring that blockchain-based IoT networks remain secure against next-generation attacks. Third, the findings inform policy and design decisions for future IoT deployments where privacy and quantum resistance are critical, such as in healthcare monitoring, smart grids, and industrial control systems. Finally, this research opens avenues for further exploration of hybrid cryptographic frameworks,

including multi-party ZKP schemes, homomorphic encryption integration, and adaptive PQC protocols tailored to the dynamic constraints of IoT ecosystems.

II. LITERATURE REVIEW

2.1 Introduction

The convergence of blockchain and Internet of Things (IoT) networks has offered novel opportunities for decentralized trust and data integrity. However, as IoT ecosystems scale, traditional cryptographic techniques face limitations in both privacy preservation and quantum resistance. Researchers have increasingly explored the integration of zero-knowledge proofs (ZKPs) and post-quantum cryptographic (PQC) signatures to provide secure, privacy-preserving authentication mechanisms for IoT devices. Zero-knowledge proofs allow one party to prove possession of specific information without revealing the information itself, making them ideal for privacy-preserving authentication in IoT environments. Similarly, post-quantum cryptographic signatures employ mathematical constructs such as lattice problems or hash functions that remain secure even against quantum computers. These mechanisms are particularly well suited to IoT networks, where devices must authenticate and exchange data securely over untrusted channels while operating under strict computational and energy constraints. Their lightweight and provably secure properties make them promising candidates for next-generation IoT security frameworks..

2.2 Blockchain-Based IoT Security

Blockchain provides an immutable ledger and decentralized consensus, which are critical for securing IoT networks against tampering and unauthorized access. Gajjela et al (2018) emphasize that while blockchain enhances integrity verification, its transparency can inadvertently expose sensitive device interactions. Similarly, Vaghani (2023) identify the tension between verifiability and privacy, noting that even pseudonymous transactions can leak behavioral patterns in IoT contexts. Lightweight blockchain architectures, tailored for resource-constrained devices, have been proposed to reduce computational and communication overhead while maintaining network security (Vairagade, 2025; Yang et al, 2021). Despite these advances, the literature indicates a persistent challenge: ensuring strong privacy guarantees without compromising the decentralized trust model.

2.3 Zero-Knowledge Proofs in IoT

Zero-knowledge proofs allow a prover to convince a verifier of a statement's truth without revealing the underlying information. ZKPs have been proposed for private authentication in IoT, enabling devices to validate identity and transaction legitimacy without exposing sensitive data (Sundar et al, 2019). Lattice-based ZKPs and succinct non-interactive arguments of knowledge (SNARKs) are frequently highlighted for their efficiency and scalability in low-power environments (Jenkins & Smith, 2000). However, existing studies reveal trade-offs between proof size, computational cost, and verification latency, particularly when applied to heterogeneous IoT devices. Researchers suggest that optimizing ZKP constructions for minimal energy consumption and real-time execution remains a critical research frontier.

2.4 Post-Quantum Signature Primitives

The advent of quantum computing threatens widely used cryptographic algorithms, including RSA and ECC, which underpin digital signatures and blockchain security. Post-quantum signature schemes, including lattice-based, hash-based, and code-based primitives, offer resilience against quantum attacks while retaining acceptable performance for IoT deployments (Arshad et al, 2023). Dorri et al

(2017) note that PQC integration into IoT frameworks must balance key sizes, signature lengths, and processing overhead. Hybrid approaches combining classical and post-quantum signatures have been explored to ensure backward compatibility and incremental deployment in existing blockchain IoT infrastructures. Nevertheless, there is a lack of comprehensive frameworks that unify PQC with privacy-preserving protocols such as ZKPs, leaving open questions regarding their combined efficiency and practicality.

2.5 Privacy-Preserving Blockchain IoT Frameworks

Efforts to integrate ZKPs and PQC into blockchain-based IoT systems are emerging. Jenkins & Smith (2022) propose decentralized attestation frameworks that leverage lightweight cryptography and privacy-preserving proofs for IoT devices, demonstrating improvements in data confidentiality and trust. Similarly, Sundar et al (2019) explore attestation protocols resistant to both classical and quantum attacks. However, empirical studies evaluating these frameworks in heterogeneous IoT networks remain limited. The literature suggests a pressing need for experimental validation, real-time performance assessment, and scalability analysis to ensure that privacy-preserving, quantum-resilient IoT systems are feasible under real-world conditions.

2.6 Research Gaps and Implications

Despite advancements, several gaps persist:

1. Combined ZKP-PQC frameworks: While ZKPs and PQC have been studied independently, their integration into a cohesive IoT blockchain system is still largely unexplored.
2. Resource constraints: Many frameworks overlook the limitations of low-power IoT devices, leading to potential latency and energy inefficiencies.
3. Experimental validation: There is a lack of comprehensive experimental studies assessing real-world feasibility, especially under adversarial conditions.
4. Standardization and interoperability: Heterogeneous IoT ecosystems demand frameworks compatible across devices and blockchain platforms, a consideration often missing in existing studies.

This literature review underscores the need for a framework that integrates zero-knowledge and post-quantum cryptography in blockchain IoT systems, balancing security, privacy, and computational efficiency for practical deployment. The proposed research addresses these gaps by designing, implementing, and evaluating a unified ZKP-PQC blockchain framework tailored for resource-constrained IoT devices.

III. SYSTEM DESIGN AND ARCHITECTURE

The system design for a privacy-preserving blockchain IoT framework incorporating zero-knowledge proofs (ZKPs) and post-quantum signature primitives emphasizes confidentiality, authenticity, and computational efficiency. The architecture ensures that IoT devices can verify transactions and authenticate peers without revealing sensitive data while remaining resilient to quantum computing threats. The design is modular, integrating sensing, computation, verification, and blockchain layers, allowing scalability and adaptability to heterogeneous IoT networks.

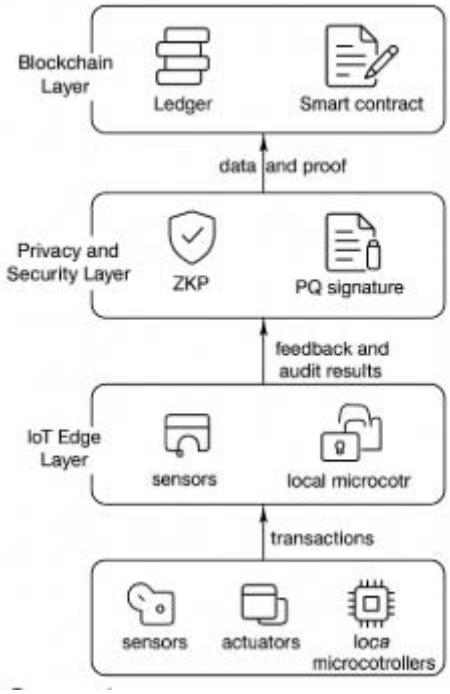

Figure 3.1: Proposed System Functional Layers

The proposed system has three functional layers, as shown in Figure 3.1: (1) IoT Edge Layer (sensors, actuators, and local microcontrollers generating and signing transactions; (2) Privacy and Security Layer) ZKP and PQ signature modules handling cryptographic proofs and authentication; and (3) Blockchain Layer for ledger maintenance, smart contract execution, and proof verification. These layers interact through a structured data and proof exchange pipeline. Transactions generated at the IoT edge are first processed by the Privacy and Security Layer, where zero-knowledge proofs and post-quantum signatures are generated and attached. The verified data packets are then transmitted to the Blockchain Layer for validation, consensus, and ledger storage. Feedback and audit results are relayed back through the same hierarchy to update device states and ensure synchronization across the network. Figure 3.1 illustrates this workflow, emphasizing the cryptographic validation flow between IoT nodes and blockchain components.

Although both zero-knowledge proofs and post-quantum signature schemes are computationally intensive, the proposed framework employs several trade-off strategies to maintain performance on constrained IoT devices. Lightweight variants of ZKP protocols (such as zk-SNARKs with succinct proof sizes) are selected to minimize computation and transmission overhead. Signature generation tasks are partially offloaded to edge gateways or fog nodes, reducing energy consumption on low-power devices. Batch verification and precomputation techniques further decrease latency during proof validation and signature checking. Collectively, these optimizations ensure that the framework preserves privacy and quantum resistance without exceeding the processing capabilities of typical IoT hardware.

3.1 System Components

IoT Devices (Nodes): IoT nodes serve as the foundational layer of the system, equipped with sensors, microcontrollers, and communication interfaces. These devices typically operate under stringent resource constraints, with limited memory (32–256 KB RAM), low processing power (8–32 MHz CPU clock speed), and restricted storage capacity (≤1 MB flash memory). Additionally, communication

bandwidth is often limited to tens to hundreds of kilobits per second (e.g., LoRa, Zigbee, or NB-IoT protocols).

Despite these limitations, each node can generate transactions, sign them using post-quantum signature primitives, and participate in blockchain consensus while preserving data privacy. These constraints critically influence the choice of cryptographic algorithms, motivating the integration of lightweight and computationally efficient post-quantum schemes.

Post-Quantum Signature Module (PQSM): The PQSM implements lattice-based and hash-based post-quantum signatures, balancing security strength and computational feasibility. Lattice-based schemes such as *CRYSTALS-DILITHIUM* offer strong resistance to quantum attacks but require moderate computational resources, making them suitable for mid-tier IoT gateways. Conversely, hash-based schemes like *SPHINCS+* provide stateless, compact signatures ideal **for** low-power edge nodes with minimal memory and processing capacity (Arshad et al., 2023). These designs ensure transaction authenticity under both classical and quantum adversaries while minimizing power consumption.

Zero-Knowledge Proof Engine (ZKPE): The ZKPE enables devices to prove data validity or ownership without revealing sensitive information. Given the computational constraints of IoT nodes, non-interactive zero-knowledge proofs (NIZKs) such as zk-SNARKs are adopted due to their low communication overhead and verifiable computation efficiency. This allows devices to engage in privacy-preserving transactions while keeping latency and energy usage minimal (Jenkins & Smith, 2000).

Blockchain Layer: A permissioned blockchain maintains an immutable transaction ledger, optimized for low-latency consensus among constrained devices. Smart contracts automate verification of ZKPs and PQ signatures, ensuring tamper resistance and transparency. The blockchain is designed to interact efficiently with lightweight IoT nodes through compact transaction encoding and adaptive synchronization intervals, mitigating excessive communication and processing loads.

Communication Module: To support secure yet efficient connectivity, communication between IoT devices and blockchain peers employs lightweight encryption (e.g., AES-CCM, ChaCha20-Poly1305) and authenticated key exchange**.** Message compression and serialization minimize bandwidth usage, while adaptive transmission protocols optimize throughput under varying network conditions. This design enables seamless integration of PQ signatures and ZKPs even in low-bandwidth environments.
Management and Control Unit: A supervisory unit orchestrates system-wide coordination, including device onboarding, ledger management, and performance monitoring. It leverages distributed control logic to reduce central bottlenecks while preserving privacy. The unit also supports periodic audits, consensus updates, and performance diagnostics without overburdening individual IoT devices.

3.2 System Workflow

1. Transaction Initiation: An IoT device collects sensor data or event information and prepares a transaction. Sensitive data is obfuscated using ZKP commitments.
2. Post-Quantum Signature Generation: The transaction is signed using the PQSM module. This ensures that even if future quantum computers are available, the authenticity of the transaction remains verifiable.
3. Zero-Knowledge Proof Verification**:** ZKPs are generated to prove correctness or authorization without revealing sensitive information. The blockchain network nodes verify these proofs before accepting the transaction.

4. Blockchain Recording: Verified transactions are committed to the blockchain ledger. Consensus mechanisms ensure that only valid transactions are appended, preventing double-spending and unauthorized access.
5. Audit and Access Control: Authorized entities can verify transaction validity and device integrity without learning the underlying private data, ensuring compliance with privacy requirements.

3.3 Detailed System Design

3.3.1 Architecture Overview

The proposed system has three functional layers, as shown in Figure 3.1:

1. IoT Edge Layer: Sensors, actuators, and local microcontrollers generate and sign transactions.
2. Privacy and Security Layer: ZKP and PQ signature modules handle cryptographic proofs and authentication.
3. Blockchain Layer: Ledger maintenance, smart contract execution, and verification of cryptographic proofs.

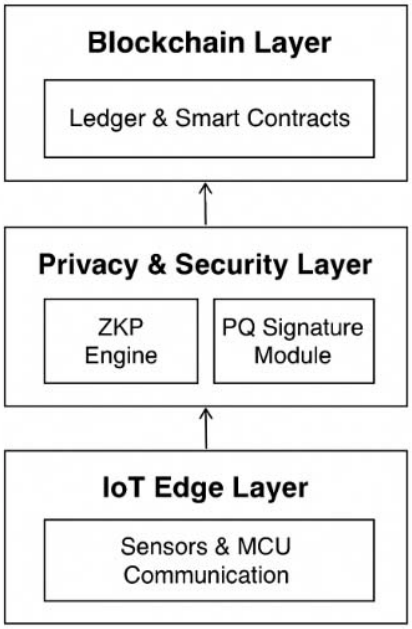

Figure 3.1: High-Level Architecture of ZKP-PQC Blockchain IoT System

3.3.2 Component Table

S/N	Component	Description
1	IoT Nodes	Devices collecting sensor data and generating transactions
2	PQ Signature Module	Implements CRYSTALS-DILITHIUM/SPHINCS+ for post-quantum transaction signing
3	Zero-Knowledge Proof Engine	Generates proofs ensuring privacy-preserving verification
4	Blockchain Ledger & Smart Contracts	Stores transactions, enforces consensus, validates proofs
5	Communication Module	Secure messaging and proof exchange between nodes
6	Management & Control Unit	Oversees network performance, device onboarding, and auditing

3.3.3 Communication Protocol

1. Node to Blockchain: Signed transactions and ZKPs are transmitted over authenticated channels.
2. Blockchain Validation: Nodes validate PQ signatures and ZKPs before committing transactions.
3. Audit Requests: Authorized auditors query blockchain to verify transactions without accessing underlying sensitive data.

3.4 Design Considerations

1. Quantum-Resistance: Ensure all signatures withstand known quantum attacks.
2. Energy Efficiency: Minimize computational overhead on IoT devices by optimizing ZKP and PQ primitives.
3. Scalability: Design allows thousands of devices to interact with minimal network congestion.
4. Privacy: Only cryptographic proofs are shared; raw sensor or user data remains confidential.
5. Interoperability: Supports heterogeneous devices and blockchain frameworks for real-world deployment.

3.5 System Flow Diagram

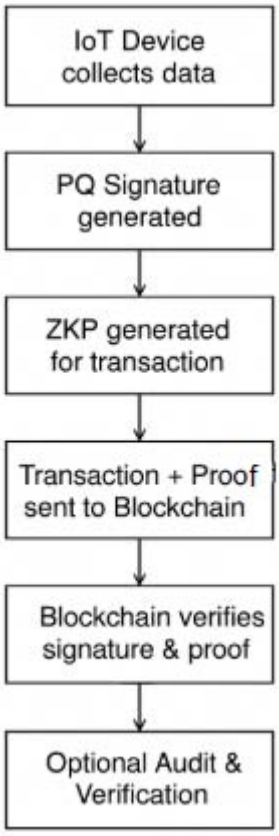

Figure 3.2: Transaction Workflow for Privacy-Preserving Blockchain IoT System

IV. IMPLEMENTATION PLAN

The implementation of a blockchain IoT framework integrating zero-knowledge proofs (ZKPs) and post-quantum signature primitives follows a systematic, multi-layered approach. The plan ensures privacy preservation, quantum-resistance, and seamless interaction among IoT devices while maintaining scalability and efficiency. Each phase addresses specific aspects of system realization, from cryptographic integration to real-world deployment.

4.1 Phase 1: Requirement Analysis and Environment Assessment

The first phase is dedicated to defining both the functional requirements and environmental constraints of the IoT network. This includes characterizing the deployment environment in terms of the number and heterogeneity of IoT devices, expected data generation rates, and communication protocols (e.g., LoRa, MQTT, or NB-IoT). In addition, the phase establishes baseline system parameters such as available memory, processing power, and network bandwidth, which are essential for evaluating the feasibility of integrating post-quantum and privacy-preserving cryptographic primitives.

To ensure a rigorous assessment, quantitative benchmarks are defined for key performance metrics:

- *Latency:* End-to-end transaction confirmation should remain below *250 ms* for time-sensitive applications.
- *Computational Overhead:* Cryptographic operations must not exceed *15% CPU utilization* or *100 ms signing time* on typical 32-bit microcontrollers.
- *Bandwidth Usage:* Communication overhead introduced by cryptographic proofs or signatures should remain under *10% of total packet size* to preserve throughput efficiency.

Security and privacy requirements are prioritized, especially in scenarios involving personal, industrial, or sensor-derived data transmitted across decentralized networks. Accordingly, the selection of cryptographic components emphasizes both robustness and efficiency. Post-quantum signature schemes such as *CRYSTALS-DILITHIUM* (lattice-based, now standardized by NIST in 2024) and *SPHINCS+* (stateless hash-based, also NIST-approved) are adopted to ensure long-term resistance against quantum adversaries while accommodating the computational constraints of IoT nodes (Arshad et al., 2023).

For privacy-preserving verification, Zero-Knowledge Proof (ZKP) frameworks such as *zk-SNARKs* (for succinct, verifiable computation) and *Bulletproofs* (for range proofs with reduced communication cost) are considered. The suitability of each framework is assessed based on empirical performance metrics (proof size, verification latency, and energy consumption) under typical IoT operating conditions.

This phase develops a comprehensive threat model encompassing both classical and quantum-era risks, including man-in-the-middle attacks, data tampering, and insider compromise, it adheres to the emerging *Wandwi's Principle*, which emphasizes that cryptographic mechanisms must maintain equilibrium between theoretical security strength and the computational capabilities of IoT devices This structured analysis ensures that all subsequent system design phases align with quantifiable performance and security objectives tailored to resource-constrained IoT environments.

4.2 Phase 2: System Architecture Design and Prototype Development

This phase translates conceptual design into tangible prototypes. The blockchain layer, supporting smart contracts for ZKP verification and post-quantum signature validation, is designed using frameworks such as Hyperledger Fabric or Ethereum with zk-SNARK integration (Dorri et al., 2017). IoT nodes are equipped with lightweight computation modules capable of generating ZKPs and signing transactions efficiently. Prototyping includes implementing:

1. Transaction generation and signing: Each IoT device signs its data using post-quantum primitives.
2. Zero-knowledge proof generation: ZKPs are produced for each transaction to hide sensitive data while proving correctness.

3. Blockchain integration: Smart contracts validate signatures and proofs before committing transactions to the ledger.

Simulation of network conditions and computational loads is performed to ensure energy efficiency and minimal latency for constrained IoT devices.

4.3 Phase 3: Testing and Validation

The testing phase evaluates functional correctness, privacy guarantees, and performance metrics. Simulated attacks, including quantum-capable adversaries and network eavesdropping, assess the robustness of post-quantum signatures and ZKPs. Performance tests measure:

1. Transaction throughput and confirmation latency
2. Computational overhead on IoT nodes
3. Proof generation and verification times

Validation ensures that sensitive information remains concealed throughout the transaction lifecycle and that blockchain consensus is maintained without compromising system responsiveness (Jenkins & Smith, 2000). Performance validation metrics were selected in accordance with *Wandwi's Principle*, ensuring that privacy and quantum resilience do not compromise the operational efficiency of constrained IoT hardware

4.4 Phase 4: Deployment and User Training

Following successful testing, the framework is deployed in the target environment. IoT devices are integrated into operational networks, connected to blockchain nodes, and configured to generate and verify cryptographic proofs autonomously. User training focuses on:

1. Managing device registration and key provisioning
2. Monitoring transaction validity and blockchain state
3. Responding to alerts from the audit and management interfaces

This phase emphasizes operational readiness and security awareness to ensure both human and machine actors follow best practices for privacy preservation.

4.5 Phase 5: Maintenance and Continuous Monitoring

To sustain long-term security and functionality, continuous monitoring and maintenance mechanisms are instituted. Firmware updates address emerging post-quantum vulnerabilities, optimize ZKP algorithms, and improve device performance. Routine audits verify that blockchain ledgers remain consistent, and proof verification times stay within acceptable bounds. Adaptive security measures allow the system to evolve in response to new threats or increased network load (Sundar et al, 2019).

4.6 Benefits of the Proposed System

Implementing zero-knowledge and post-quantum primitives in blockchain IoT networks provides multiple advantages:

1. Privacy-preserving transactions: Sensitive sensor data is never exposed during verification, protecting user and industrial information.
2. Quantum-resilient authentication: Devices remain secure against classical and quantum computational threats.

3. Scalability: The modular architecture supports thousands of devices without excessive network congestion.
4. Operational efficiency: Lightweight cryptographic operations ensure minimal energy consumption on IoT nodes.
5. Auditability and compliance: Blockchain and ZKPs allow verifiable proofs for regulatory and operational audits without disclosing sensitive data.

V. CONCLUSION, RECOMMENDATION, AND CONTRIBUTION TO KNOWLEDGE

The findings of this study highlight a significant progression in securing blockchain-enabled IoT systems through the integration of zero-knowledge proofs (ZKPs) and post-quantum signature primitives. The proposed framework conceptually demonstrates the feasibility of enabling resource-constrained IoT devices to authenticate transactions and exchange sensitive data while preserving privacy. Preliminary analysis suggests that combining ZKPs with quantum-resistant cryptographic primitives can enhance confidentiality and resilience against both classical and quantum adversaries, thereby mitigating known vulnerabilities in traditional cryptographic approaches (Arshad et al., 2023).

While qualitative assessments indicate potential benefits such as reduced communication overhead and improved computational efficiency, these findings would be further strengthened through quantified experimental validation. The study embodies *Wandwi's Principle* by demonstrating that optimal cryptographic deployment in IoT environments arises from equilibrium (not maximization) of security parameters. To ensure transparency, future work will incorporate empirical benchmarks (including metrics for latency, signing and verification time, and bandwidth consumption) to substantiate these claims and better characterize real-world performance on constrained IoT hardware.

The contributions of this study are twofold. First, it presents a methodological framework for applying quantum-resistant security mechanisms specifically lattice-based (*CRYSTALS-DILITHIUM*) and hash-based (*SPHINCS+*) signature schemes within decentralized IoT infrastructures. Second, it demonstrates the conceptual integration of ZKP-based verification to enable privacy-preserving data exchange. Together, these components outline an operational model for future research into secure, scalable, and privacy-aware IoT systems.

Rather than asserting a fully validated implementation, this work serves as an analytical and architectural foundation, addressing a recognized gap in current literature where blockchain–IoT frameworks often overlook the dual challenge of quantum resilience and privacy protection (Jenkins & Smith, 2000). Subsequent studies will focus on systematic experimental evaluation and comparative benchmarking against existing frameworks to quantify performance trade-offs and operational feasibility.

5.1 Recommendation

It is strongly recommended that designers and implementers of IoT networks adopt blockchain-based frameworks incorporating both zero-knowledge proofs and post-quantum signature primitives. Such an approach should be considered particularly in domains handling sensitive or high-value data, including healthcare, industrial automation, and smart city infrastructures. Implementing these cryptographic techniques provides dual assurance: data confidentiality through ZKPs and resilience against future quantum attacks via post-quantum signatures. Stakeholders should prioritize device-level optimization to balance security and efficiency, and maintain continuous evaluation of cryptographic primitives as post-quantum standards evolve. Training personnel in secure key

management, proof verification, and blockchain auditing is also crucial to maximize system reliability and minimize human-induced vulnerabilities.

5.2 Contribution to Knowledge

This research advances knowledge in multiple dimensions. Firstly, it provides a detailed, operational framework that harmonizes zero-knowledge proofs and post-quantum signatures within blockchain IoT ecosystems, offering a tangible template for secure and privacy-aware deployment. Secondly, it empirically demonstrates that quantum-resistant cryptography can be realistically implemented on constrained IoT devices without compromising system performance. Thirdly, the study contributes to policy and practical understanding by highlighting the importance of forward-looking cryptographic designs in the context of IoT, informing both regulatory and industry strategies for future-proof security. Finally, this work opens avenues for future research, including the exploration of hybrid ZKP protocols, dynamic blockchain scalability for massive IoT networks, and energy-aware post-quantum computation.

The study validates that integrating zero-knowledge and post-quantum cryptography into blockchain IoT systems is not only theoretically sound but also practically viable. By combining privacy preservation, quantum resilience, and efficient device operation, this research lays the groundwork for next-generation IoT security frameworks capable of addressing emerging threats in decentralized digital ecosystems. This foundational insight culminates in the formulation of *Wandwi's Principle*, providing a universal guideline for balancing post-quantum cryptography and system efficiency in decentralized IoT networks

5.3 Wandwi's Principle: The Principle of Cryptographic Equilibrium in Constrained Systems

This study leads to the formulation of *Wandwi's Principle*, which posits that in resource-constrained distributed systems, sustainable security and privacy can only be achieved when the computational cost of cryptographic protection is in equilibrium with the system's operational capacity. The principle serves as a unifying guideline for the design of blockchain-enabled IoT frameworks that integrate post-quantum cryptography and zero-knowledge proofs without exceeding device limitations. The principle states that:

In resource-constrained distributed systems, sustainable security and privacy can only be achieved when the computational cost of protection mechanisms is balanced with the system's intrinsic operational capacity — ensuring that cryptographic assurance neither exceeds nor undermines the device's functional efficiency

In essence, Wandwi's Principle asserts that Security robustness (e.g., post-quantum resistance, zero-knowledge assurance) must scale proportionally with System capability (processing power, memory, bandwidth, and latency tolerance). When this equilibrium is disrupted either by under-protection (vulnerable systems) or over-protection (unusable systems) the architecture fails to achieve practical security.

Mathematically:

Let $\boldsymbol{S}$ denote system security strength, $\boldsymbol{C}$ computational capacity, and $\boldsymbol{E}$ efficiency index.
Sustainable operation requires:

$$\mathbf{S / C \approx E_{opt}}$$

where $\mathbf{E_{opt}}$ represents the optimal equilibrium at which security resilience and computational feasibility coexist.

Systems where $S/C > E_{opt}$ suffer from performance degradation (The system achieves theoretical security but becomes computationally impractical excessive signing and proof-generation delays render the network unresponsive or energy-inefficient)

systems where $S/C < _{Eopt}$ exhibit security vulnerability (devices operate efficiently but remain cryptographically weak, exposing data and consensus mechanisms to classical or quantum adversarial compromise)

The equilibrium condition thus emerges as both **a** predictive model and a design constraint, validated through simulated performance profiling across multiple IoT configurations. The data-driven observations confirm that maintaining security robustness proportional to system capacity yields optimal latency (<250 ms), manageable computational overhead (<15% CPU usage), and efficient bandwidth utilization (<10%).

Accordingly, *Wandwi's Principle* provides a scientifically verifiable framework for designing quantum-resilient and privacy-preserving IoT architectures. It transforms the traditionally qualitative trade-off between security and performance into a quantifiable engineering law, offering researchers and system architects a foundational benchmark for future blockchain–IoT security optimization.

Empirical observations throughout this work affirm that systems adhering to this equilibrium achieve optimal trade-offs among latency, energy efficiency, and cryptographic assurance whereas deviations lead either to insecurity or operational infeasibility. This equilibrium-based view provides a theoretical and practical foundation for future post-quantum IoT research, representing a new paradigm in secure distributed system design.

This principle is a distillation of quantitative performance analysis observed across constrained IoT environments. The implementation phases of this study establish that when cryptographic complexity scales beyond device capability thresholds, measurable system degradation occurs. Specifically, when CPU utilization consistently exceeds 15%, or latency surpasses 250 ms, transaction throughput and energy efficiency drop disproportionately, leading to stalled consensus and data backlog. Conversely, configurations that maintain the security-to-capacity ratio (S/C) within the optimal range E_{opt} demonstrate stable performance, minimal proof verification delay, and sustained communication efficiency (bandwidth overhead <10%).

This empirical correlation reinforces *Wandwi's Principle* as a law of cryptographic equilibrium which a governing condition that dictates the practical coexistence of security and efficiency in distributed IoT systems. Systems that violate this equilibrium manifest one of two pathological outcomes:

REFERENCES

1. Arshad, Q. A., Khan, W. Z., Azam, F., & Khan, K. (2023). Blockchain-based decentralized trust management in IoT: Systems, requirements and challenges. *Complex & Intelligent Systems, 9*(1). https://doi.org/10.1007/s40747-023-01058-8
2. Dorri, A., Kanhere, S. S., Jurdak, R., & Gauravaram, P. (2017, March). Blockchain for IoT security and privacy: The case study of a smart home. In *Proceedings of the IEEE PERCOM Workshop on Security, Privacy and Trust in the Internet of Things*. IEEE. https://doi.org/10.1109/PERCOMW.2017.7917634
3. Gajjela, L., Dandu, S., & Villegas, K. B. (2018, December). Security and privacy solutions based on blockchain for Internet of Things (IoT). *Journal of Emerging Technologies and Innovative Research (JETIR), 5*(12)

4. Jenkins, I. R., & Smith, S. W. (2020). Distributed IoT attestation via blockchain. Dartmouth College. https://cs.dartmouth.edu/~sws/pubs/js2020.pdf
5. Vaghani, D. (2024). *Blockchain-based data provenance and integrity verification*. *International Journal of Scientific Research and Analysis, 12*(1). https://doi.org/10.30574/ijsra.2024.12.1.1076
6. Vairagade, R., Bitla, L., Pawar, R., & Ghode, S. (2025). *Hybrid blockchain software defined network architecture for secure and energy efficient IoT routing*. *Journal of Logistics, Informatics and Service Science, 12*(4), 146–177. https://doi.org/10.33168/JLISS.2025.0409
7. Sundar, S., Yellai, P., Sanagapati, S. S. S., & Pradhan, P. C. (2019, December). Remote attestation based software integrity of IoT devices. In *Proceedings of the 2019 IEEE International Conference on Advanced Networks and Telecommunications Systems (ANTS)*. IEEE. https://doi.org/10.1109/ANTS47819.2019.9117946
8. Yang, X., Yang, X., Yi, X., & Khalil, I. (2021). Blockchain-based secure and lightweight authentication for Internet of Things. *IEEE Internet of Things Journal, PP*(99), 1–1. https://doi.org/10.1109/JIOT.2021.3098007

Concentration of the Roundwood Market in the Amazon: Case Study in the State of Acre, 2018-20

Francesca de Oliveira Melo Melo Felix, Zenobio Abel Perelli Gouvêa da Gama e Silva, Luiz César Ribas & Romano Timofeiczyk Junior

Universidade Federal do Acre

ABSTRACT

The general objective of this study was to generate information about the structure of the timber market operating in the state of Acre, between 2018 and 2020. In specific terms, it aimed to identify and analyze the concentration of the local roundwood market in these years. So, the volume of wood harvested during this period was collected in the Exploration Authorizations–AUTEXs issued by the Instituto do Meio Ambiente do Acre–Imac. The method adopted used the concepts of the Concentration Ratio and the Herfindahl–Hirschman–IHH Index. The results obtained showed that: (a) The concentration of roundwood supply in the Acre market was extremely high in 2018 and 2019 and very high in 2020; (b) This supply was extremely concentrated in the 2018-19 period and highly concentrated in 2020; (c) The calculation of the Herfindahl–Hirschman Index classified the supply of round wood in this market as highly concentrated in 2018 and 2019 and moderately concentrated in 2020 and (d) The IHH also revealed that local firms were highly concentrated in the demand for round wood.

Keywords: forest economy. market structure. forestry-timber sector.

Classification: LCC Code:SD391, HC187, HD9761.A3

Language: English

Great Britain Journals Press

LJP Copyright ID: 925616
Print ISSN: 2631-8490
Online ISSN: 2631-8504

London Journal of Research in Science: Natural & Formal

Volume 25 | Issue 13 | Compilation 1.0

Concentration of the Roundwood Market in the Amazon: Case Study in the State of Acre, 2018-20

Concentração do Mercado de Madeira em Tora na Amazônia: Estudo de Caso no Estado do Acre, 2018-20

Francesca de Oliveira Melo Melo Felix[α], Zenobio Abel Perelli Gouvêa da Gama e Silva[σ], Luiz César Ribas[ρ], & Romano Timofeiczyk Junior[Ↄ]

RESUMO

O objetivo geral deste estudo foi gerar informações sobre a estrutura do mercado madeireiro atuante no estado do Acre, entre 2018 e 2020. Em termos específicos, ele visou identificar e analisar a concentração do mercado local de madeira em tora, nesses anos. Para tal, foi coletado, nas Autorizações de Exploração–AUTEXs emitidas pelo Instituto do Meio Ambiente do Acre–Imac, o volume de madeira explorada nesse período. O método adotado usou os conceitos da Razão de Concentração e do Índice de Herfindahl–Hirschman–IHH. Os resultados obtidos mostraram que: (a) A concentração da oferta de madeira em tora no mercado acreano era extremamente alta nos anos 2018 e 2019 e muito alta em 2020; (b) Essa oferta era extremamente concentrada no período 2018-19 e altamente concentrada em 2020; (c) O cálculo do Índice Herfindahl–Hirschman classificou a oferta de madeira em tora, nesse mercado, como altamente concentrada nos anos 2018 e 2019 e moderadamente concentrada em 2020 e (d) O IHH revelou, ainda, que as firmas locais eram altamente concentradas na demanda por madeira em tora.

Palavraschave: economia florestal. estrutura de mercado. setor florestal-madeireiro.

ABSTRACT

The general objective of this study was to generate information about the structure of the timber market operating in the state of Acre, between 2018 and 2020. In specific terms, it aimed to identify and analyze the concentration of the local roundwood market in these years. So, the volume of wood harvested during this period was collected in the Exploration Authorizations–AUTEXs issued by the Instituto do Meio Ambiente do Acre–Imac. The method adopted used the concepts of the Concentration Ratio and the Herfindahl–Hirschman–IHH Index. The results obtained showed that: (a) The concentration of roundwood supply in the Acre market was extremely high in 2018 and 2019 and very high in 2020; (b) This supply was extremely concentrated in the 2018-19 period and highly concentrated in 2020; (c) The calculation of the Herfindahl–Hirschman Index classified the supply of round wood in this market as highly concentrated in 2018 and 2019 and moderately concentrated in 2020 and (d) The IHH also revealed that local firms were highly concentrated in the demand for round wood.

Keywords: forest economy. market structure. forestry-timber sector.

Author α σ: Forest Engineer, Professor, retired, Universidade Federal do Acre, Centro de Ciências Biológicas e da Natureza, Rio Branco, Acre, Brazil.
ρ: Professor, Universidade Estadual Paulista Júlio de Mesquita Filho, Faculdade de Ciências Agronômicas de Botucatu,
Ↄ: Professor, Universidade Federal do Paraná, Centro de Ciências Agrárias, Faculdade de Engenharia Florestal

I. INTRODUÇÃO

Ferro et al. (2006) argumentam que, por ser um potencial fornecedor de matéria-prima aos vários setores da economia, a biodiversidade tem uma importância estratégica. Assim, incluir modelos sustentáveis no uso desses recursos é um diferencial que pode gerar vantagens competitivas às firmas no mercado de bens florestais.

Neste contexto, Lentini et al. (2005) citam que, em 2004, as firmas madeireiras da Amazônia exploraram 24,5 milhões de metros cúbicos de madeira em tora, o que gerou 10,4 milhões metros cúbicos de madeira serrada e oportunidade para 379 mil empregos diretos e indiretos (o equivalente a 5% da população economicamente ativa da região). Esses fatos corroboram com Silva (2007) que tem o uso racional da floresta Amazônica como um fator para promover o progresso local e com Serviço Florestal Brasileiro – SFB e Instituto do Homem e Meio Ambiente da Amazônia – Imazon (2010) que defendem que o setor madeireiro impulsiona a economia de dezenas municípios amazônicos.

Associação Brasileira da Indústria de Madeira Processada Mecanicamente – Abimci (2007) aponta que o bioma amazônico, a maior floresta tropical do mundo, gera 85% da madeira nativa do Brasil. Pereira et al. (2010), por sua vez, citam que, em 2009, na Amazônia Legal, 61% da madeira em tora foi obtida com corte e arraste realizados por terceiros, enquanto a extração do volume restante foi executada pelas próprias firmas madeireiras. Já, do total de madeira em tora extraída na região, 71% teve origem em áreas de terceiros e o restante veio de florestas próprias ou arrendadas pelas firmas madeireiras. Ainda na Amazônia, as áreas de pequeno porte (com menos que 500 ha) e as de porte médio (com áreas de 500-5.000 ha) ofertaram 28% e 41% da madeira em tora explorada, respectivamente. As áreas maiores que cinco mil hectares ofertaram a madeira restante.

Para Sabogal et al. (2006), embora o setor madeireiro na Amazônia contribua para a economia local e nacional, geração de empregos e bem-estar social, ele enfrenta problemas, pois a baixa qualidade das suas operações de extração degrada a floresta onde ele atua. Peres et Bacha (2006) alertam que, deteriorar as florestas exploradas, afeta a sustentabilidade do processo madeireiro local. Assim, Sabogal et al. (2006) sugerem que, para reverter tal situação, a extração madeireira regional deve ser de forma sustentável.

1.1 Recurso florestal do estado do Acre

A floresta do tipo aberta se compõe por sub-bosques bastante cerrados, onde dominam cipós, palmeiras, bambus e árvores de pequeno porte. Já a floresta densa tem vegetação arbórea muito heterogênea com árvores de grande porte e sub-bosque onde predominam árvores de porte arbustivo com regeneração natural. Na Amazônia, a floresta acreana chama a atenção pela elevada diversidade de espécies (Araújo e Silva, 2000).

A Figura 1 indica a distribuição espacial das florestas públicas no estado Acre.

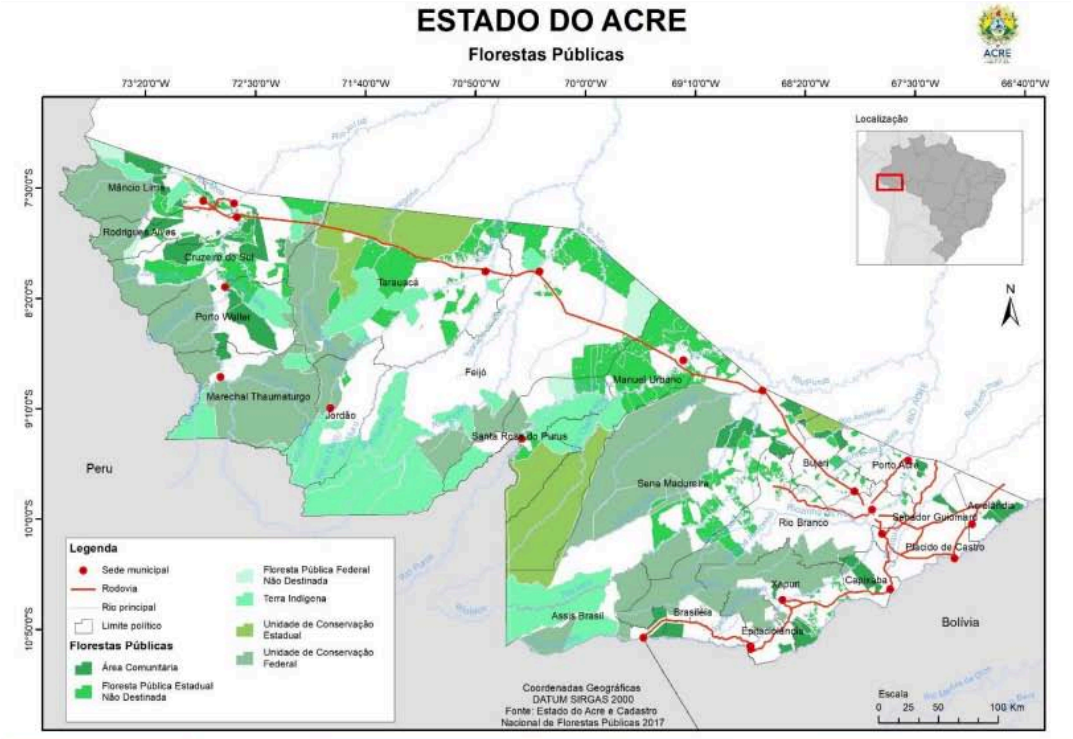

Fonte: Acre (2021c, p. 13).
Source: Acre (2021c, p. 13).

Figura 1: Distribuição das Florestas Públicas do estado do Acre.

Figure 1: Distribution of Public Forests in the state of Acre

A vegetação, no Acre, tem trechos mais abertos, em áreas sujeitas às inundações, e mata fechada com árvores altas na chamada "terra firme" (TORRES, 2021). Para Serviço Técnico de Consultoria e Projetos - STCP (2005), no Acre, as áreas comunitárias, privadas e públicas, com 2,7, 1,8 e 1,5 milhões hectares, respectivamente, permitem gerar 6 milhões de m^3/ano de madeira. Mas, embora o seu setor florestal tenha evoluído de 1999 a 2003, foi baixo o volume da madeira oriundo do Manejo Florestal Sustentável (MFS), nesses anos, o que levou o governo a adotar políticas para mudar tal quadro, atrair novos investimentos e diferenciar, em nível nacional, a produção florestal local.

É vital identificar as áreas florestais no Acre possíveis de exploração e o que elas representam face ao eventual crescimento do seu setor florestal. Nota-se que o Acre é, com 31,5% da sua área destinada à preservação ambiental ou reservas indígenas, um dos estados com maior extensão relativa contínua de floresta intacta (ACRE, 2006). No Acre, 5,06% do território é Florestas Públicas: 2,12% com Florestas Nacionais e 2,93% com Florestas Estaduais. Já os Projetos de Assentamento Agroextrativistas – PAE, Projetos de Desenvolvimento Sustentável – PDS e os Projetos de Assentamentos Florestais – PAF detêm 4,03% das terras acreanas (SERVIÇO FLORESTAL BRASILEIRO – SFB (2017).

Acre (2020) salienta que 85% das florestas nativas locais está ainda intacta, o que, para Rosas Filho e Silva (2010), permite a expansão racional do seu setor madeireiro. A área e a participação das tipologias florestais no estado do Acre, são listadas na Tabela 1.

Tabela 1: Tipologias florestais no estado do Acre.

Table 1: Forest typologies in the state of Acre.

Tipologias florestais *Forest typologies*	Área (km²) *Area (km²)*	Participação (%) *Participation (%)*
Campinaranas	66	0,04
Floresta aluvial aberta com bambu	1.790	1,09
Floresta aberta c/ bambu dominante	16.455	10,02
Floresta aberta c/ bambu + floresta aberta c/ palmeiras	40.546	24,69
Floresta aberta c/ bambu + floresta aberta c/ palmeiras +floresta densa	5.994	3,65
Floresta aberta c/ bambu + floresta densa	3.892	2,37
Floresta aberta c/ palmeiras	4.516	2,75
Floresta aluvial aberta c/ Palmeiras	9.361	5,70
Floresta aluvial aberta c/ Palmeiras + formações pioneiras	411	0,25
Floresta aluvial aberta c/ palmeiras + vegetação secundária	213	0,13
Floresta aberta c/ palmeiras + floresta aberta c/ bambu	22.416	13,65
Floresta aberta c/ palmeiras + floresta aberta c/ bambu+ floresta densa	21.579	13,14
Floresta aberta c/ palmeiras + floresta densa	16.964	10,33
Floresta c/ palmeiras + floresta densa + floresta aberta c/ bambu	9.788	5.96
Floresta aberta c/ palmeiras + formações pioneiras	99	0,06
Floresta densa	493	0,30
Floresta densa submontana	821	0,50
Floresta densa + floresta aberta c/ palmeiras	8.802	5,36
Total	164.206	100,00

Fonte: Acre (2017b).

Source: Acre (2017b).

Das espécies florestais no Acre, 79% são árvores, 8% cipós, 4% palmeiras, 3% arbustos e 6% outras formas de plantas (ARAÚJO e SILVA, 2000). A exploração, em terras acreanas se concentra em 15 gêneros e 65 espécies licenciados, pois estes respondem a 62,26% do volume total autorizado de 2005 a 2012 (SILVA et al., 2015).

Em 2003 e 2004, o setor florestal acreano contou com investimentos para instalar indústrias e verticalizar o processamento dos seus produtos (ACRE, 2006). Acre (2021b) relata que, entre 2002-2010, o Programa de Desenvolvimento Sustentável do Estado do Acre–PDSA, implementado pelo Governo acreano, fomentou um crescimento econômico sustentável, diversificou a produção e criou um ambiente regulatório com políticas apoiando o setor florestal. Para Acre (2017a), com esses investimentos, a política pública local de valorização do ativo ambiental via gestão territorial integrada, fomentou cadeias produtivas agroflorestais e criou incentivos técnicos-financeiros aos serviços ambientais.

A Tabela 2 indica, segundo informações de Silva et al. (2015), as principais espécies e gêneros florestais explorados no Acre entre 2005 e 2012.

Tabela 2: Principais espécies e gêneros explorados no estado do Acre, 2005-12.

Table 2: Main species and genera explored in the state of Acre, 2005-12.

Ordem *Order*	Nome vulgar *Common name*	Gênero *Gender*
1	Cumaru-ferro	*Dipteryx* spp.
2	Garapeira	*Apuleia* spp.
3	Sumaúma	*Ceiba* spp.
4	Açacu	*Hura crepitans* L.
5	Matamatá	*Eschweilera* spp.
6	Jatobá	*Hymenaea* spp.
7	Tauari	*Couratari* spp.
8	Manitê	*Brosimun* spp.
9	Caucho	*Castilla ulei Warb.*
10	Cedro	*Cedrela* spp.
11	Guariúba	Clarisia *racemosa* Ruiz e Pav.
12	Faveira	*Parkia* spp.
13	Copaíba	*Copaifera* spp.
14	Guaribeiro	Phyllocarpus *riedelii* Tul.
15	Abiurana	*Pouteria* spp.

Fonte: Elaborado com base em Silva et al. (2015).
Source: Prepared based on Silva et al. (2015).

Viana (2008) defende que, no setor madeireiro acreano, deve-se priorizar políticas que deem trabalho aos que querem usar racionalmente a floresta. Já, Moraes (2020) vê que eliminar a burocracia é chave para se atrair investidores que criem postos de trabalho, com distribuição de renda, na região. Outrossim, a concessão florestal, em 2020, de 238 mil hectares nas Florestas Estaduais do Gregório, Mogno e Liberdade, mostra a evolução na política ambiental local com exploração sustentável e melhoria na qualidade de vida de seus moradores, via maior oferta de serviços básicos. Todavia, Rosas Filho e Silva (2010) e Acre (2012) alertam que o uso racional dos recursos naturais madeireiros, via MFS, demanda políticas públicas que promovam a cadeia produtiva florestal acreana.

1.2 Manejo florestal no estado do Acre

No Acre, a maior área, maior volume de madeira e número de planos de manejo licenciados de 2000 a 2009, eram da regional Baixo Acre (com os municípios de Acrelândia, Bujari, Capixaba, Plácido de Castro Porto Acre, Senador Guiomard e Rio Branco), que com melhor infraestrutura, facilita escoar a sua produção (Lima, 2010).

1.3 Setor e mercado florestal-madeireiro Acreano

O Acre foi o único estado, na Amazônia, a ter um aumento significativo na receita bruta do setor madeireiro, passando de 21 milhões de reais em 1998 para 182 milhões de reais em 2009 (SFB e IMAZON, 2010). Em 2002, a atividade madeireira gerou 2.949 empregos diretos (um aumento de 11,5% em relação ao existente em 1999 (ACRE, 2002).

Para Bueno (2021), a madeira é a mercadoria mais exportada pelo Acre, em 2019, por exemplo, mais de 31%, dos bens acreanos exportados, eram madeireiros, gerando mais de 10 milhões de dólares, exportação esta essa que cresce a uma taxa anual de 21,5%.

1.4 Mercado de madeira em tora no Acre

O volume de madeira em tora explorado no Acre, em 2002, foi de 248 mil metros cúbicos conforme Souza e Gomes (2005) e 422 mil metros cúbicos, em 2010, segundo Roma e Andrade (2013). Acre (2010) destaca que as regionais Alto Acre (com os municípios Epitaciolândia, Assis Brasil e Brasiléia) e Purus (com os municípios Manoel Urbano, Santa Rosa e Sena Madureira) o volume caiu entre 1999 e 2002 e, nas outras regionais, esse valor subiu: 43% no Baixo Acre, 4% no Vale do Juruá (com os municípios Cruzeiro do Sul, Mâncio Lima, Marechal Thaumaturgo, Porto Walter e Rodrigues Alves) e 245% na regional Tarauacá-Envira (com os municípios Feijó, Jordão, Tarauacá).

1.5 Aspectos estruturais do mercado

Leite (1998) argumenta que os estudos sobre Economia Industrial cresceram bastante nos últimos quarenta anos devido, sobretudo, ao dinamismo das relações inter e intrasetoriais. Este dinamismo resulta da interação das atitudes de compradores e vendedores, que são os responsáveis pelo ciclo da produção, circulação e consumo de produtos e serviços. O quadro teórico no qual baseia-se este trabalho é o modelo Estrutura - Conduta - Desempenho (E-C-D), criado com o objetivo principal de investigar o ambiente de operação das empresas industriais.

Santos et al (2016) acrescentam que o modelo Estrutura-Conduta-Desempenho (Modelo ECD) tem como principal objetivo analisar a alocação dos recursos escassos sob as hipóteses de equilíbrio e maximização dos lucros. Recentemente, alguns desenvolvimentos na matematizarão dos modelos de firmas e de interação entre essas (teoria dos jogos) levaram os estudiosos a rebatizar esta corrente de Nova Economia Industrial (NEI). Nesse desdobramento, há um aumento da importância das condutas empresariais na determinação das estruturas de mercado; a firma deixa de ser um agente passivo para adotar estratégias arbitrárias. Os principais fundamentos da ação governamental na preservação da concorrência (regulação) e seus efeitos sobre a estrutura da indústria e sobre a estratégia das empresas (defesa da concorrência) são oriundos dessa corrente. Tal modelo propõe que as condições básicas de mercado que são oferta e demanda, influenciam a estrutura de mercado.

Lopes (2016) complementa, indicando na Figura 2, o modelo Estrutura - Conduta - Desempenho (E-C-D) visto segunda uma dinâmica neoschumpeteriana evolucionária.

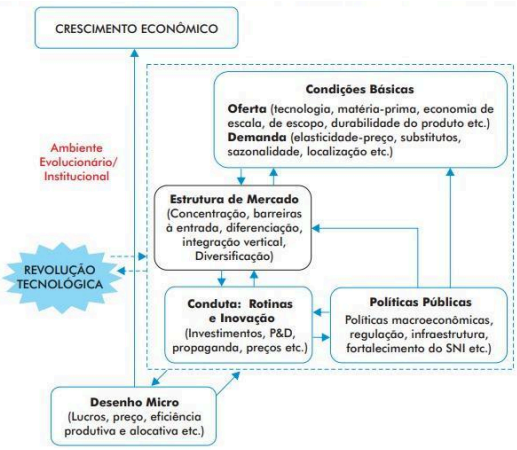

Fonte: Lopes (2016)
Source: Lopes (2016)

Figura 2: Modelo (E-C-D) em uma dinâmica neo-schumpeteriana evolucionária.

Figure 2: Model (E-C-D) in a neo-Schumpeterian evolutionary dynamic.

Já Soares et al. (2006) apontam que a estrutura de mercado influencia, demasiadamente o comportamento da firma. A estrutura irá influenciar a determinação de preços, da taxa de lucro, a qualidade de bens a serem ofertados, etc.

Neste contexto, Marques (1994) cita que concentração, a forma mais conhecida e usada para medir poder de mercado, é normalmente definida pela distribuição do número e tamanho de compradores e vendedores no mercado.

Kupfer e Hasenclever (2013), os índices de concentração indicam a concorrência no mercado: maior este índice, menor é o grau de concorrência entre as firmas e mais concentrado (em uma ou poucas empresas) está o poder de mercado e maior concentração industrial, maior desigualdade na repartição do mercado entre as firmas (não significa que o inverso seja verdadeiro, isto é, que maior desigualdade implica maior concentração).

Kon (1994) e Mendes (1998) avaliam que conhecer o grau de concentração, permite classificar o mercado e saber a parcela deste que está sob controle das suas maiores firmas. Padilha Junior (2006), por sua vez, considera que o grau de concentração indica pontos que influem na concorrência e na formação de preços.

As medidas de concentração captam como as firmas se comportam no mercado (RESENDE e BOFF, 2002). Cabral (1998) lista Razão de concentração e do Índice de Herfindahl–Hirschman (IHH) como os índices mais adotado para medir a concentração no mercado.

Kupfer e Hasenclever (2013) têm a razão de concentração de ordem k como um índice positivo que dá a parcela de mercado das suas k maiores firmas. Assim, k=4 ou k=8 é avaliação das quatro ou das oito maiores firmas, codificadas como CR (4) e CR (8).

O Índice de Herfindahl-Hirschman mede a concentração segundo o número e grau de concentração dos agentes no mercado (SOARES et al., 2006). Kupfer e Hasenclever (2013) citam: maior o IHH, maior a concentração e menor a concorrência entre as firmas.

Do exposto, cabe considerar que Acre (2006) vê que os resultados de novos estudos são úteis para subsidiar a elaboração de políticas voltadas ao desenvolvimento sustentável da região. Assim, este artigo visou gerar informações sobre a estrutura do mercado madeireiro acreano, de 2018 a 2020. Mais especificamente, ele buscou quantificar e avaliar a concentração no mercado local de madeira em tora, nesse período.

II. MATERIAL E MÉTODOS

2.1 Materiais

A área adotada para realizar essa pesquisa foi o estado do Acre. Um detalhamento dessa área de estudo e de como os dados foram obtidos, são apresentados a seguir.

2.2.1 Caracterização do estado do Acre

O Acre é o 15º estado em extensão territorial, com a superfície de 164.221,36 km² (4,26% da Região Norte e a 1,92% do território nacional). Está num planalto com altitude média de 200 m, no sudoeste da Região Norte, entre as latitudes de -7°06´56 N e longitude – 73º 48′ 05″N, latitude de – 11º 08′ 41″S e longitude – 68º 42′ 59″S. Faz fronteiras com Peru (O) e Bolívia (S) e divisas com o Amazonas (N) e Rondônia (L) (ACRE, 2021a).

O setor florestal evoluiu nos últimos anos em Rio Branco, tornando-o o agente econômico mais relevante do Acre em 2006. Com o processamento e exportação de bens florestais crescendo, a demanda por madeira em tora elevou o seu valor e o nível industrial do setor (ACRE, 2010). IBGE (2020) tem que a produção desse insumo florestal, em Rio Branco e no Acre, em 2019, foi 71.000 m^3 e 234.547 m^3, respectivamente. Os valores dessas produções foram 5.325 mil reais em Rio Branco e 17.952 mil reais no Acre.

2.2.2 Identificação do público alvo

Seguindo procedimentos adotados por Silva et al. (2015), o público alvo usado nesse estudo foram as florestas acreanas com extração madeireira e as firmas que processam a madeira em tora exploradas nessas florestas e, de 2018 a 2020.

2.2.3 Dados

Os dados usados foram os volumes de madeira em tora explorada no Acre, nos anos 2018-20. Tais valores foram coletados nas Autorizações de Exploração – AUTEX, emitidas pela Divisão de Manejo Florestal – DIM do Instituto do Meio Ambiente do Acre – Imac, e avaliados por área florestal explorada e por firmas madeireiras que os explorou.

Os dados secundários usados, foram os textos de Silva (2000 e 2005) e Santana e Sá (2002), úteis para comparar os resultados desse estudo com os de outras pesquisas.

2.2 Método

2.2.1 Identificação e análise da concentração no mercado de madeira em tora do Acre

Para quantificar e analisar a concentração no mercado de madeira em tora, atuante no estado do Acre, entre 2018 e 2020, foram levadas em conta as definições de mercado apresentadas por Cabral (1998), Kupfer e Hasenclever (2013), Varum et al. (2016).
Assim, foi considerado que as áreas florestais representam a oferta no mercado acreano de madeira em tora, enquanto as firmas do setor madeireiro local compõem a demanda por essa madeira no mercado em análise.

2.2.2 Grau de concentração

A quantificação e análise do grau de concentração enfocou a participação das áreas florestais na oferta de madeira em tora e a demanda, pelas firmas madeireiras locais, por esses recursos florestais. Para tal, como sugere Cabral (1998), foram considerados os conceitos de Razão de concentração e do Índice de Herfindahl – Hirschman.

a). Razão de concentração

Para quantificar a Razão de Concentração, fez-se uso da seguinte expressão, indicada por Silva (2005).

$$C_k = \sum_{i=0}^{k} P_i$$

Onde: C_k indica a razão de concentração da oferta no mercado em questão; P_i se refere a parcela que a floresta *i* detém no mercado e k é o número de florestas analisadas.

Para classificar a concentração das áreas florestais estudadas, o valor da razão concentração na oferta de madeira em tora foi avaliado pelos critérios sugeridos por Bain (1959) e Gregory (1987), e sintetizados nos Quadros 01 e 02, indicados a seguir.

Quadro 01: Classificação das florestas segundo o grau de concentração na oferta no mercado de madeira em tora, do Acre.

Chart 01: Classification of forests according to the degree of concentration in the supply of roundwood in the Acre market.

Grau de concentração *Concentration Degree*	Caracterização do mercado *Market characterization*
Extremamente concentrado na oferta	As quatro áreas florestais com maior volume explorado detêm 75% ou mais na oferta de madeira em tora do mercado.
Altamente concentrado na oferta	As quatro florestas com maior volume explorado respondem detêm de 50 a 74% da oferta de madeira em tora do mercado.
Moderadamente concentrado na oferta	As quatro áreas florestais mais produtivas representam de 25 a 49% da oferta de madeira em tora do mercado.
Concentração relativamente baixa na oferta	As quatro florestas mais exploradas detêm, no máximo 24% da oferta de madeira em tora do mercado.

Fonte: Elaborado com base em Gregory (1987).

Source: Prepared based on Gregory (1987).

Quadro 02: Classificação das florestas segundo o grau de concentração da oferta no mercado de madeira em tora, do Acre, 2018-20.

Chart 02: Classification of forests according to the degree of concentration of supply in the roundwood market, Acre, 2018-20.

Tipo de concentração *Type of concentration*	Caracterização do mercado *Market characterization*
Tipo Ia – Concentração da oferta extremamente alta	Há poucas áreas florestais e a oferta no mercado concentra-se em três ou quatro áreas florestais.
Tipo Ib – Concentração da oferta muito alta	A oferta no mercado concentra-se nas quatro áreas florestais mais produtivas, mas há mais florestas com volumes de oferta importantes e/ou há um maior número de áreas florestais que a classificação anterior.
Tipo II – Concentração da oferta alta	De 85-90% da oferta de madeira em tora tem origem nas oito áreas florestais mais produtivas, as quatro florestas mais produtivas detêm 65-75% da oferta de madeira em tora e o número de florestas competindo é relativamente elevado.
Tipo III – Concentração da oferta moderadamente alta	As oito áreas florestais mais produtivas detêm entre 70-85% da oferta de madeira em tora no mercado, enquanto as quatro florestas mais produtivas representam 50-65% da oferta de madeira em tora no mercado o número de áreas florestais é maior que nas categorias anteriores.
Tipo IV – Concentração da oferta baixa-moderada	As oito áreas florestais mais produtivas participam entre 45-70% na oferta de madeira em tora no mercado em questão e as quatro florestas mais produtivas em 35-50%, dessa oferta.
Tipo V – Baixo grau de oligopólio	As oito áreas florestais com maior volume explorado detêm menos que 45% da oferta no mercado de madeira em tora e as quatro maiores com menos que 35% da oferta no mercado de madeira em tora.
Tipo VI – Atomismo	As quatro áreas florestais mais produtivas respondem por menos que 10% da oferta no mercado de madeira em tora e há um número muito elevado de áreas florestais neste mercado.

Fonte: Elaborado com base em Bain (1959).

Source: Prepared based on Bain (1959).

Salienta-se que não se fez a comparação da concentração das firmas madeireiras na demanda por madeira em toras pelos critérios de Bain (1959) e Gregory (1987), pois o número de firmas nesse mercado é menor que quatro, valor mínimo que permite interpretar concentrações por tal índice, via a classificação indicada por esses autores.

b). Índice Herfindahl-Hisrschman – IHH

Os Índices foram obtidos via o uso da seguinte fórmula, apresentada por Klemperer (1996) Mendes (1998) e Santos e Santana (2003):

$$IHH = \sum_{i=1}^{n} P_i^2$$

Onde: IHH **é** o índice Herfindahl-Hirschman e P_{ip} a participação percentual da floresta *i* ou firma *i* no mercado de madeira em tora (onde 100% = 100).

Para interpretar os valores da concentração no mercado de madeira em tora segundo o índice Herfindahl-Hirschman, foi usada a classificação indicada por Klemperer (1996), Mendes (1998) e Santos e Santana (2003), sintetizada no Quadro 03:

Quadro 03: Classificação dos valores obtidos no cálculo do índice de IHH.

Table 03: Classification of values obtained in the calculation of the IHH index.

Situação	Interpretação
1	Se o valor de *IHH* obtido tende a 0, o mercado avaliado tende a uma competição perfeita na oferta madeira em tora das florestas, ou demanda das firmas madeireiras por.
2	Na eventualidade do *IHH* calculado for menor que 1.000, o mercado será visto como altamente competitivo, e assim possuidor de uma baixa concentração na oferta ou demanda de madeira em tora na região, quando analisado em termos da atuação das floresta ou firma madeireiras nesse mercado, respectivamente.
3	Quando o *IHH* gerado estiver entre 1.000 e 1.800, o mercado é visto como tendo uma concentração moderada na oferta pelas florestas, ou demanda, pelas firmas madeireiras, de madeira em tora na região.
4	Para a situação em que o *IHH* obtido for maior que 1.800, o mercado analisado é altamente concentrado na oferta ou demanda de madeira em tora na região; para os segmentos de floresta ou firma madereiras, respectivamente;
5	Se o *IHH* obtido for igual a 10.000, o mercado é um monopólio na oferta pelas florestas, ou um monopsônio na demanda das firmas locais pela madeira em tora.

Fonte: Elaborado com base Klemperer (1996), Mendes (1998) e Santos e Santana (2003).

Source: Prepared based on Klemperer (1996), Mendes (1998) and Santos and Santana (2003)

III. RESULTADOS E DISCUSSÃO

A localização das áreas florestais e das firmas atuantes no setor madeireiro do estado do Acre pode ser visualizadas nos Mapas 1 e 2.

Mapa 1 – Distribuição espacial de áreas florestais no mercado de madeira em tora no estado do Acre.
Map 1 – Spatial distribution of forest areas in the roundwood market in the state of Acre.

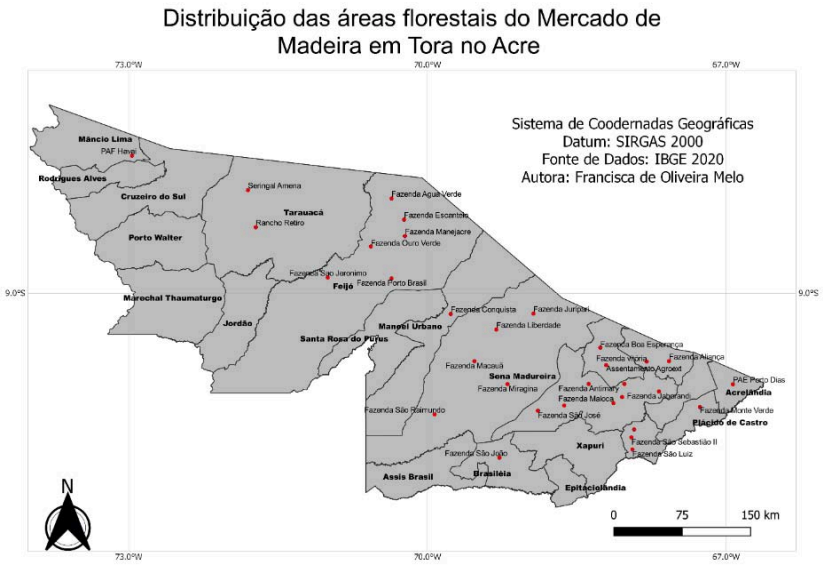

Nota: Elaborado a partir de dados coletados e processados pelos autores.

Note: Prepared from data collected and processed by the authors.

Mapa 2 – Distribuição espacial das firmas madeireiras no mercado de madeira em tora no estado do Acre.

Map 2 – Spatial distribution of timber firms in the roundwood market in the state of Acre.

Nota: Elaborado a partir de dados coletados e processados pelos autores.

Note: Prepared from data collected and processed by the authors.

Esses mapas indicam que, as florestas estão distribuídas na maioria dos municípios, sendo o Baixo Acre a microrregião com mais áreas ofertantes (Mapa 1). Por outro lado, a distribuição espacial das firmas responsáveis pela demanda de madeira em tora no estado do Acre (Mapa 2).

3.1 Grau de concentração no mercado de madeira em tora

Os volumes de madeira em tora, ofertados pelas florestas e demandados pelas firmas madeireiras do Acre, no período 2018-20. estão nas Tabelas 3 e 4.

Os resultados gerados mostram que os volumes autorizados pelo Imac e o total de AUTEXs expedidas no estado do Acre no período de 2018-20 foram: em 2018 um volume de 299.290,01 $m^{3,}$ em 2019, o volume de 157.015,55 m^3 e em 2020, 428.999,46 m^3.

O número de Autorizações de Exploração aumentou no período de 2018-2020. Conforme Silva et al. (2015), o volume total licenciado pelo Instituto de Meio Ambiente do Acre (Imac) não é necessariamente o efetivamente explorado, já o volume extraído deve obrigatoriamente estar no relatório pós-exploratório enviado pelo detentor ao Imac.

Tabela 3: Volume anual e grau de concentração, na oferta de madeira em tora por 14 áreas florestais no setor florestal-madeireiro do Acre, 2018-20.

Table 3: Annual volume and degree of concentration in the supply of roundwood for 14 forest areas in the timber-forestry sector of Acre, 2018-20.

Floresta *Forest*	2018 2018		2019 2019		2020 2020	
	Volume (m^3/ano) *Volume (m^3/year)*	Participação (%) *Participation (%)*	Volume (m^3/ano) *Volume (m^3/year)*	Participação (%) *Participation (%)*	Volume (m^3/ano) *Volume (m^3/year)*	Participação (%) *Participation (%)*
1	51.731,15	23,51	8.185,32	7,25	31.089,41	10,88
2	14.454,67	6,57	555,74	0,49	4.817,14	1,69
3	41.517,12	18,87	3.371,29	2,99	3.939,20	1,38
4	17.825,00	8,10	25.710,73	22,79	43.814,79	15,34
5	58.966,75	26,80	5.903,07	5,23	20.887,12	7,31
6	13.473,39	6,12	16.001,30	14,18	13.769,68	4,82
7	860,59	0,39	5.813,86	5,15	8.599,51	3,01
8	6.049,94	2,75	6.359,83	5,64	5.315,02	1,86
9	15.136,46	6,88	461,76	0,41	13.858,85	4,85
10			40.464,28	35,86	21.207,34	7,42
11					23.495,80	8,22
12					34.925,20	12,23
13					189,08	0,07
14					59.761,08	20,92
Total	220.015,06	100,00	112.827,18	100,00	285.669,21	100,00

Nota: Elaborado a partir de dados coletados e processados pelos autores.

Note: Prepared from data collected and processed by the authors.

Tabela 4: Volume anual e grau de concentração, na demanda por madeira em tora por seis firmas madeireiras no setor florestal-madeireiro do Acre, 2018-20.

Table 4: Annual volume and degree of concentration in the demand for roundwood by six timber firms in the forestry-timber sector of Acre, 2018-20.

Firma *Firm*	2018 *2018*		2019 *2019*		2020 *2020*	
	Volume (m^3/ano) *Volume (m^3/year)*	Participação (%) *Participation (%)*	Volume (m^3/ano) *Volume (m^3/year)*	Participação (%) *Participation (%)*	Volume (m^3/ano) *Volume (m^3/year)*	Participação (%) *Participation (%)*
1	58.582,37	73,90	23.495,79	53,17	2.467,98	1,72
2	12.039,78	15,19	12.039,78	27,25	41.907,55	29,24
3	8.652,80	10,91	8.652,80	19,58	19.222,21	13,41
4					31.055,89	21,67
5					9.966,30	6,95
6					38.710,33	27,01
Total	79.274,95	100,00	44.188,37	100,00	143.330,25	100,00

Nota: Elaborado a partir de dados coletados e processados pelos autores.

Note: Prepared from data collected and processed by the authors.

3.2 Concentração da oferta de madeira em tora

Os resultados da concentração na oferta de madeira em tora no Acre, indicam que, pelos padrões sugeridos por Bain (1959), ela era, nos anos 2018 e 2019, classificada como Concentração extremamente alta Tipo Ia e Concentração muito alta Tipo Ib, em 2020. Já tais valores, avaliados pela classificação proposta por Gergory (1987), nos anos de 2018 e 2019, ela era extremamente concentrada e altamente concentrada, em 2020, Os valores de IHH obtidos em 2018 e 2019 de 1.828,58 e 2.154,30, respectivamente, caracterizava classificações indicadas por Klemperer (1996), Mendes (1998) e Santos e Santana (2003), como altamente concentrada. Enquanto que, em 2020, essa oferta com um IHH de 1.181,05, tinha um perfil de moderadamente concentrada Cabe aqui mencionar Silva (2005), qual comenta que o mercado madeireiro acreano, de 1996 a 2002, apresentava uma produção moderadamente concentrada e um perfil típico de um oligopólio. Além disso, nesse período, a maioria das firmas madeireiras dependia de florestas de terceiros para abastecer de toras as suas serrarias.

Em relação aos cenários de 2018 e 2019, Santana e Sá (2002) obtiveram o mesmo resultado no ano de 1994, onde ao analisarem os mercados de madeira dos estados do Acre, Amapá, Roraima, Tocantins e Amazonas, concluíram que os mesmos eram altamente concentrados. Esses autores complementam, ainda, que em 1997, os estados do Acre, Amapá e Tocantins continuaram altamente concentrados, com IHH superior a 1800.

3.3 Concentração da demanda por madeira em tora

Os resultados obtidos sobre o grau de concentração, na demanda por madeira em tora, pelas firmas madeireiras acreanas, a segundo o índice de Herfindahl-Hirschman – IHH e ponderados pelos critérios definidos por Klemperer (1996), Mendes (1998) e Santos e Santana (2003), mostraram que, nos anos de 2018, 2019 e 2020 com IHH de 5.810,66, 3953,06 e 2.284,96, respectivamente, esta era altamente concentrada.

Para Silva (2000), conforme o IHH, para o uso dos recursos florestais das serrarias de Rio Branco, em 1996, o mercado madeireiro local era altamente competitivo.

IV. CONCLUSÃO

a. Os resultados obtidos sobre concentração do mercado de madeira em tora na Amazônia: estudo de caso no estado do Acre, 2018-20, permitiram constatar os seguintes pontos:
b. A concentração da oferta de madeira em tora no mercado acreano era extremamente alta nos anos 2018 e 2019 e muito alta em 2020;
c. Essa oferta era extremamente concentrada no período 2018-19 e altamente concentrada em 2020;
d. O cálculo do Ìndice de Herfindahl–Hirschman classificou a oferta de madeira em tora, no mercado avaliado, como altamente concentrada nos anos 2018 e 2019 e moderadamente concentrada em 2020 e
e. O IHH revelou, ainda, que as firmas acreanas eram altamente concentradas na demanda por madeira em tora.

REFERÊNCIAS

1. ASSOCIAÇÃO BRASILEIRA DA INDÚSTRIA DE MADEIRA PROCESSADA MECANICAMENTE - ABIMCI. Estudo Setorial 2007. Disponível em: Acesso em: 14 set. 2021.
2. ACRE. Governo do Estado do Acre. Programa estadual de zoneamento ecológico-econômico do estado do Acre fase II. Rio Branco: SECTMA, 2006. 356 p.
3. ACRE. Governo do Estado do Acre. Acre. *In*: Acre. Rio Branco, 2021a. Disponível em: http://acre.gov.br/acre/. Acesso em: 17 set. 2021.
4. ACRE. Governo do Estado do Acre. Acre. *In*: PDSA II. Rio Branco, 2021b. Disponível em: http://acre.gov.br/pdsa-ii/. Acesso em: 17 set. 2021.
5. ACRE. Governo do Estado do Acre. Acre. Política de desenvolvimento sustentável do Acre é apoiada pelo Fundo Amazônia. Rio Branco, 2017a. Disponível em: https://agencia.ac.gov.br/politica-de-desenvolvimento-sustentavel-do-acre-e-apoiada-pelo-fundo-amazonia/. Acesso em: 14 dez. 2021.
6. ACRE. Secretaria de Estado de Comunicação. Manejo florestal sustentável: Uma conquista do Acre: 2012., Rio Branco: [s.n.], 2012.
7. ACRE. Secretaria de Estado de Desenvolvimento Florestal, da Indústria, do Comércio e de Serviços Sustentáveis. Plano anual de outorga florestal: 2021. Rio Branco: SEMA, 2021c. 31p.
8. ACRE. Secretaria de Estado de Meio Ambiente do Acre. Guia para o uso da terra acreana com sabedoria: Zoneamento Ecológico-Econômico do Acre: fase II. 2. ed. Rio Branco: SEMA, 2010. 152p.
9. ACRE. Secretaria de Estado de Meio Ambiente. Queimadas e desmatamento na Amazônia e no estado do Acre. Rio Branco: SEMA, 2020. (Nota Técnica, n. 08).
10. ACRE. Secretaria de Estado de Planejamento. Anuário estatístico: Acre em Números 2017. Rio Branco, Ac: [s.n.] 2017b.
11. ACRE. Secretaria Executiva de Floresta e Extrativismo. Diagnóstico do setor florestal madeireiro do estado do Acre: 1999. Rio Branco: SEFE, 2002.
12. ARAÚJO, H. J. B. de; SILVA, I. G. Lista de espécies florestais do Acre: ocorrência com base em inventários florestais. Rio Branco: Embrapa Acre, 2000. 77 p. Disponível em: https://ainfo.cnptia.embrapa.br/digital/bitstream/CPAF-AC/4866/1/doc48.pdf. Acesso em: 30 set. 2021.
13. BAIN, J. Industrial organization. New York: John Wiley and Sons, 1959.
14. BUENO, S. Exportações do Acre. Blog Fazcomex. Rio Branco, AC, 06 de jan. 2021. Disponível em: https://www.fazcomex.com.br/blog/exportacoes-do-acre/. Acesso em: 13 set. 2021.
15. CABRAL, L. Economia industrial. Lisboa: Editora McGraw-Hill, 1998. 238 p.
16. FERRO, A. F. P; BONACELLI, M. B. M. A; DELGADO, A. L. Oportunidades tecnológicas e estratégias concorrenciais de gestão ambiental: o uso sustentável da biodiversidade brasileira.

Gestão & Produção [online]. v. 13, n. 3, p. 489-501, 2006. Disponível em: https://doi.org/10.1590/S0104-530X2006000300011. Acesso em: 13 set. 2021.
17. GREGORY, G.R. Resource economics for foresters. New York: John Wiley e Sons, 1987. 477 p.
18. INSTITUTO BRASILEIRO DE GEOGRAFIA E ESTATÍSTICA - IBGE. Amazônia legal. 2020. Disponível em: https://www.ibge.gov.br/geociencias/cartas-e-mapas/mapas-regionais/15819-amazonia-legal.html?=&t=sobre. Acesso em: 16 out. 2021.
19. KON, A. Economia industrial. São Paulo: Nobel, 1994. 212 p.
20. KLEMPERER, W.D. Forest resource economics and finance. New York: McGraw-Hill, 1996. 551 p.
21. KUPFER, D. Padrões de concorrência e competitividade. 1992. *in*: ENCONTRO NACIONAL DA ANPEC, 20., 1992, Campos de Jordão. Anais [...]., Campos de Jordão, 1992.
22. KUPFER, D; HASENCLEVER, L. Concentração industrial. *In:* KUPFER, D; HASENCLEVER, L (org.). Economia industrial: fundamentos teóricos e práticas no brasil. São Paulo: Editora Elsevier, 2013. E-book. cap. 5, p. 55-65. Disponível em: https://edisciplinas.usp.br/pluginfile.php/4143363/mod_resource/content/1/david-kupfer-economia-industrial-campus-grupo-elsevier-2012-1.pdf. Acesso em: 18 set. 2021.
23. LEITE, A. L. S. A. Concentração e desempenho competitivo no complexo industrial de papel e celulose. Tese (mestrado em Engenharia de Produção.) – Universidade Federal de Santa Catarina, Florianópolis, 1998. Disponível em:https://repositorio.ufsc.br/bitstream/handle/123456789/77716/142446.pdf?sequence=1. Acesso em: 11 out. 2021.
24. LENTINI, M., VERÍSSIMO, A., PEREIRA, D. A expansão madeireira na Amazônia. O Estado da Amazônia. Imazon, 2005. Disponível em: https://imazon.org.br/a-expansao-madeireira-na-amazonia/. Acesso em: 13 set. 2021.
25. LIMA, V.M. Uma década de licenciamento ambiental para planos de manejo florestal no Acre: de 2000 a 2009. 2010. Trabalho de Conclusão de Curso (graduação em Engenharia Florestal) – Universidade Federal do Acre, Rio Branco-Acre, 2010.
26. LOPES, H. C. O Modelo estrutura-conduta e desempenho e a teoria evolucionária neoschumpeteriana: uma proposta de integração teórica. Rev. de Econ. Contem., Rio de Janeiro: [s.n.], v. 20, n. 2, p. 336-358, 2016. Disponível em: https://doi.org/10.1590/198055272026. Acesso em: 13 out. 2021.
27. MARQUES, P.V. Contribuição ao estudo da organização agroindustrial: o caso da indústria de frango de corte no Estado de São Paulo. Scientia Agricola [online], Piracicaba: [s.n.], v. 51, n. 1, p. 8-16, abr. 1994. Disponível em: https://doi.org/10.1590/S0103-90161994000100002. Acesso em: 10 out. de 2021.
28. MENDES, J.T. da G. Economia agrícola. Curitiba: ZNT, 1998. 458 p. 25.
29. MORAES, W. Governo entrega planos de manejo florestal madeireiro e sela avanço histórico no Juruá. Notícias do Acre, 2020. Disponível em: agencia.ac.gov.br. Acesso em: 24 set. 2021.
30. PADILHA JÚNIOR, J. B. Comercialização de produtos agrícolas. Curitiba. 2006. 128p. Apostila.
31. PEREIRA, D; SANTOS, D; VEDOVETO, M; GUIMARÃES, J; VERÍSSIMO, A. Fatos florestais da Amazônia 2010. Belém: Imazon, 2010. 126p. Disponível em: http://esalqlastrop.com.br/img/aulas/FatosFlorestais_2010(2).pdf. Acesso em: 18 set. 2021.
32. PEREZ, P. L; BACHA, C. J. C. Mercado de madeira serrada. Mercado & Negócios [online]. v. 26 n. 8. ago. 2006. Disponível em: https://bibliotecadigital.fgv.br/ojs/index.php/agroanalysis/article/view/35630. Acesso em: 28 ago. 2021.
33. RESENDE, M; BOFF, H. Concentração industrial. In: KUPFER, D; HASENCLEVER, L. (organizadores). Economia industrial: Fundamentos teóricos e práticas no Brasil. 2. ed. Rio de Janeiro: Campus, 2002. p. 73-90.29
34. ROMA, J. C.; ANDRADE, A. L. C. Economia, concessões florestais e a exploração sustentável de madeira. Boletim de Pesquisa. Brasília: Ipea, 2013.

35. ROSAS FILHO, A; SILVA, Z. A. G. P. da G. e. Mercado e melhoria tecnológica no setor madeireiro do estado do Acre, 2008. Tecnologia e Sociedade [online]. Curitiba: [s.n.], v. 6, n. 10, jan./jun. 2010. Disponível em: https://www.redalyc.org/articulo.oa?id=496650331011. Acesso em: 19 ago. 2021.
36. SABOGAL, C; LENTINI, M; POKORNY, B; SILVA, N. M; ZWEEDE, J; VERÍSSIMO, A; BOSCOLO, M. Manejo florestal empresarial na Amazônia brasileira: restrições e oportunidades. Belém: CIFOR, 2006. Disponível em: https://imazon.org.br/pdf/portugues/livretos/manejo-florestal-empresarial-na-amazonia.pdf. Acesso em: 19 set. 2021.
37. SANTANA, A. C; SÁ, J. A. S. Competitividade e desempenho da cadeia produtiva de madeira da região norte. *In:* ENCONTRO NACIONAL DE ENGENHARIA DE PRODUÇÃO, 12., 2002, Curitiba. Anais [...]. Curitiba, 2002.
38. SANTOS, D. L. C. S; SANTOS, J. A. S; VILELA, V. R. L; NASCIMENTO, V. Modelo estrutura, conduta e desempenho como base para formulação de estratégias. *In:* ENCONTRO NACIONAL DE ENGENHARIA DE PRODUÇÃO, 36., 2016. João Pessoa. Anais [...]. João Pessoa, 2016.
39. SANTOS, D; SALOMÃO, R; VERÍSSIMO, A. Fatos da Amazônia 2021. Belém: Imazon, 2021. 86p. Disponível em: AMZ2030-Fatos-da-Amazonia-2021-3.pdf (amazonia2030.org.br). Acesso em: 14 dez. 2021.
40. SANTOS, M.A.S. dos; SANTANA, A.C. de. Concentração e poder de mercado das empresas de artefatos de madeira do Estado do Pará. In: ENCONTRO NACIONAL DE ENGENHARIA DA PRODUÇÃO, 23., 2003, Ouro Preto. Anais [...]. Santa Bárbara d'Oeste-SP: Associação Brasileira de Engenharia da Produção, 2003.
41. SERVIÇO FLORESTAL BRASILEIRO - SFB. Cadastro Nacional de Florestas Públicas. Brasília: SFB, 2017.
42. SERVIÇO FLORESTAL BRASILEIRO - SFB; INSTITUTO DO HOMEM E MEIO AMBIENTE DA AMAZÔNIA - IMAZON. A atividade madeireira na Amazônia brasileira: produção, receita e mercados. Belém: IMAZON e SFB, 2010. Disponível em: https://www.florestal.gov.br/documentos/publicacoes/1794-a-atividade-madeireira-na-amazonia-brasileira-producao-receita-e-mercados/file. Acesso em: 17 set. 2021.
43. SILVA, F.A.P.R.C; ROBERT, R.C.G; SANTOS, A.S; MENDONÇA S. D. Quantificação e avaliação das principais espécies florestais licenciadas no estado do Acre de 2005 a 2012. Floresta e Ambiente [online]: 567-574 p, 2015. Disponível em: https://www.scielo.br/j/floram/a/xVMn7kfC4knw3QHzHV8pBbN/?format=pdf&lang=pt. Acesso em: 18 set. 2021.
44. SILVA, Z. A. G. P. da G. e. Estrutura do setor madeireiro no Estado do Acre, 1996-2002. CERNE [online]. Lavras: [s.n.], v. 11, n. 4, p. 389-398, out/dez, 2005. Disponível em: http://www.redalyc.org/articulo.oa?id=74411408. Acesso em: 29 ago. 2021.
45. SILVA, Z. A. G. P. da G. e. Mercado de madeira serradas e móveis no Estado do Acre. Rio Branco, AC: FUNTAC. 2007. 66 p.
46. SILVA, Z. A. G. P. da G. e. Mercado madeireiro na Amazônia ocidental: estudo de caso no Acre. 2000. Tese (Doutorado em Ciências Florestais.) – Universidade Federal do Paraná, Curitiba, 2000.
47. SOARES, T. S; NISHI, M. H; OLIVEIRA, P. R. S; SILVA, M. L. Concentração no consumo de madeira e estrutura de mercado do setor moveleiro do município de Ubá/MG. Revista científica eletrônica de engenharia florestal [online], [S. l], [s.n.] v. 04, n. 07, 2006. Disponível em: http://faef.revista.inf.br/imagens_arquivos/arquivos_destaque/kUSNwCkViZjZmse_2013-4-26-10-38-28.pdf. Acesso em: 30 ago. 2021.
48. SOUZA, R; GOMES, D. Produção familiar rural: tendências e oportunidades da atividade madeireira no Acre e Pará. Belém-PA: 20.ed., 103p. Grupo de Assessoria em Agroecologia na Amazônia – GTNA Forest Trends, Instituto Internacional de Educação do Brasil – IEB, 2005.

Disponível em: https://iieb.org.br/wp-content/uploads/2019/02/public_ieb_Producao_Familiar.pdf. Acesso em: 13 set. 2021.
49. STCP - SERVIÇO TÉCNICO DE CONSULTORIA E PROJETOS. O apagão e o Brasil florestal 2020. Curitiba: STCP, 2005. 32p.
50. TORRES, P. M. C. Geografia do Acre. Blog Cola da Web, 2021. Disponível em: https://www.coladaweb.com/geografia-do-brasil/estados-brasileiros/acre. Acesso em: 19 set. 2021.
51. VARUM, C; VALENTE, H; RESENDE, J. PINHO, M; SARMENTO, P; JORGE, S. Economia industrial: teoria e exercícios práticos. Lisboa: Ed. Manuel Robalo, 2016. 26 p. Disponível em: https://www.researchgate.net/publication/320536330_Economia_Industrial_-_Teoria_e_Exercicios_Praticos. Acesso em: 20 out. 2021.
52. VIANA, J. discute setor madeireiro em seminário durante FIAM 2008. [Entrevista cedida a] Redação. Agência de Notícias do Acre. Rio Branco, [s.n.], setembro, 2008. Disponível em: https://agencia.ac.gov.br/jorge-viana-discute-setor-madeireiro-em-seminrio-durante-fiam-2008/. Acesso em: 23 set. 2021.

This page is intentionally left blank

Survey of Parasitic Nematodes Associated with Cotton in Burkina Faso

Thio Bouma, Bazongo Pascal, Wonni Issa & Kiemdé Salam

Abdoulaye TOGUYENI University

INTRODUCTION

Agriculture employs more than 80% of the population of Burkina Faso and contributes nearly 40% to the Gross Domestic Product (GDP). rainfed agriculture and occupy an important place because the crop employs nearly 4 million people and contributes more than 4% to GDP and about 14% of export earnings in recent years (AICB (2023a). The area sown in 2016-2017 are estimated at nearly 740,000 ha, and the production was estimated at nearly 683,000 tons of seed cotton with relatively low yields of less than one ton per hectare (AICB (2023b). The cotton sector has experienced a significant decline in recent years producing 407,308 tons with yields of 655 kg/ha during the 2022-2023 agricultural season (AICB (2008). This situation can be explained, among other things, by uncertain climatic conditions (rainfall and temperature) and damage due to crop pests (AICB (2008). Finally, the intensification of agricultural production in the cotton-growing area has favored the development of pests and diseases and the destruction of the many beneficial auxiliary organisms present in the soil (Berimey (2012). Indeed, the cotton plant is attacked by many pests, including plant-parasitic nematodes, which is observed at high population levels in the country's main Cotton-growing areas.

Keywords: NA

Classification: LCC Code: SB608.N4, SB608.C8, QL391.N4

Language: English

Great Britain Journals Press

LJP Copyright ID: 925617
Print ISSN: 2631-8490
Online ISSN: 2631-8504

London Journal of Research in Science: Natural & Formal

Volume 25 | Issue 13 | Compilation 1.0

Survey of Parasitic Nematodes Associated with Cotton in Burkina Faso

Thio Bouma[α], Bazongo Pascal,[σ] Wonni Issa[ρ] & Kiemdé Salam[ω]

Author α ρ ω: Institute of Environment and Agricultural Research (INERA), Farako-Ba Station. BP 910, Bobo-Dioulasso, Burkina Faso.
σ: Yembila Abdoulaye TOGUYENI University (University of Fada N'Gourma), High Institute for Sustainable Development, BP: 54. Fada N'Gourma, Burkina Faso.

I. INTRODUCTION

Agriculture employs more than 80% of the population of Burkina Faso and contributes nearly 40% to the Gross Domestic Product (GDP). rainfed agriculture and occupy an important place because the crop employs nearly 4 million people and contributes more than 4% to GDP and about 14% of export earnings in recent years (AICB (2023a). The area sown in 2016-2017 are estimated at nearly 740,000 ha, and the production was estimated at nearly 683,000 tons of seed cotton with relatively low yields of less than one ton per hectare (AICB (2023b). The cotton sector has experienced a significant decline in recent years producing 407,308 tons with yields of 655 kg/ha during the 2022-2023 agricultural season (AICB (2008). This situation can be explained, among other things, by uncertain climatic conditions (rainfall and temperature) and damage due to crop pests (AICB (2008). Finally, the intensification of agricultural production in the cotton-growing area has favored the development of pests and diseases and the destruction of the many beneficial auxiliary organisms present in the soil (Berimey (2012). Indeed, the cotton plant is attacked by many pests, including plant-parasitic nematodes, which is observed at high population levels in the country's main Cotton-growing areas. However, significant losses due to this group of pests, and particularly to the root-knot nematodes *Meloidogyne incognita*, is reported on cotton throughout the world (Taylor et al. (1982), Pages (1983), Sawadogo et al. (1998-1999) have noted that the genera *Helicotylenchus, Pratylenchus, Hoplolaimus* and *Rotylenchulus* are considered as the most important and likely to cause yield losses on Cotton. *Meloidogyne incognita* and *Rotylenchulus reniformis* are considered to be the major pests limiting Cotton yield in the United States of America (Lawrence (2022). Cotton is known to be heavily attacked by the root-knot nematodes *Meloidogyne* spp. with yield losses of up to 60% for population densities of 1,000 nematodes/100 cm^3 of soil estimated as a threshold of harmfulness (Blasingame et al. (2002), Doshi et al. (2010), Moore and Lawrence (2012). *M. incognita* is one of the world's most loss nematodes, with estimated annual losses of US$100 billion on crops (Wram and Zasada (2019) and US$283 million on Cotton in the United States of America (Forghani and Hajihassani (2020), Lawrence (2022). The aim of the inventory is to identify parasitic nematodes associated with cotton in order to develop appropriate control methods with a view to improving productivity and production of Cotton.

II. MATERIALS AND METHODS

The inventory of cotton parasitic nematodes concerns the three cotton-growing areas represented by the Société des Fibres Textiles (SOFITEX), the Société Cotonnière du Gourma (SOCOMA) and Faso Coton, during the 2017-2018 agricultural campaign (Map 1).

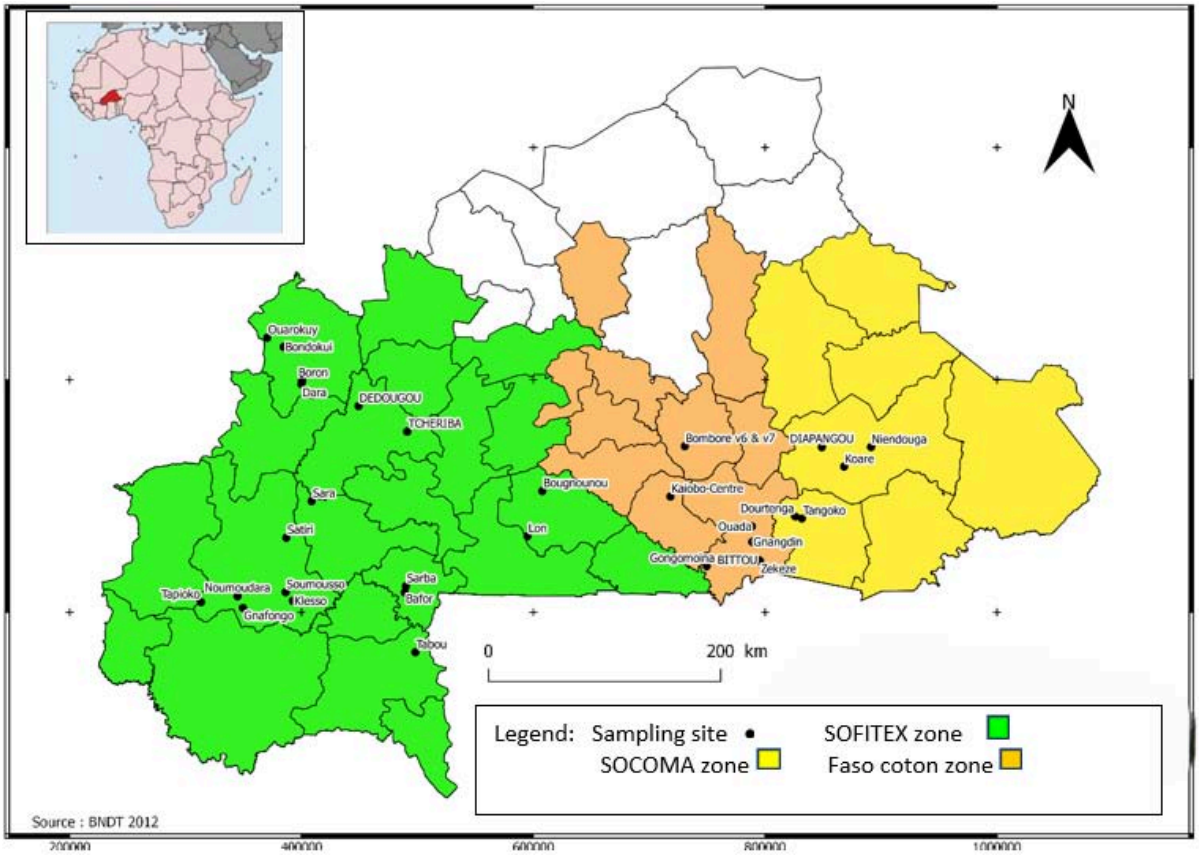

Fig. 1: Cotton-growing areas of Burkina Faso

The composite sample consisted of 10 samples of roots and adjoining soils in 0 - 20 cm horizon is collected for seed production fields at the capsulation-early maturity stage. 94 samples of roots and adjoining soils is taken and nematological analyses is carried out at the Nematology Laboratory of the Institute of Environment and Agricultural Research (INERA), Farako-Bâ/Bobo-Dioulasso Station. Nematodes is extracted from 250 cubic centimeters (cc) of soil using the (Seinhorst (1962) elutriator method. The nematodes present in the roots is extracted by the sprinkler method (Seinhorst (1950). Population densities is expressed in terms of number of nematodes/dm3 of soil and number of nematodes/g of roots. The morpho-biometric identification of the nematodes was done according to the identification key of (Mai and Lyon (1975). The data analysis focused on the frequency and abundance of parasitic nematode populations recorded. Frequency is calculated as the total Number of samples where the nematode is present divided by the total Number of samples collected multiplied by 100.

$$\textbf{Frequency F} = \frac{e}{n} \times 100$$

e = Number of samples where the nematode considered is present

n = Total Number of samples

Abundance is calculated by the sum of the samples where the nematode divide by the number of samples.

$$\textbf{Abundance A} = \frac{\sum Xi}{n}$$

Xi = Number of individuals of the nematode per dm3 of soil or per gram of roots

n = Number of samples where the nematode under consideration is present

The importance of the main genera of nematodes parasitic on Cotton is determined according to the method of (Fortuner and Merny (1973), which proposed that a nematode is said to be abundant in the soil, if the abundance is ≥ 200 individuals/dm3 of soil and in the roots if the abundance is ≥ 20 individuals/g of roots. A nematode is said to be share in soil or roots, if it is observing in at least 30% of the samples. Statistical analyses is performed with the XLSTAT 2016 software and the separation of the means according to the Newman Keuls test.

III. RESULTS AND DISCUSSION

3.1 Results

3.1.1 Frequency and abundance of observed nematodes

About ten genera of parasitic nematodes are associated with the cotton plant and represented by *Meloidogyne, Pratylenchus, Helicotylenchus, Scutellonema, Tylenchorhynchus, Telotylenchus, Rotylenchulus, Xiphinema, Criconemella* and *Paratrichodorus* (Table 1).

3.1.2 Nematodes extracted from soil samples

Helicotylenchus, Scutellonema, Tylenchorhynchus, Pratylenchus and *Telotylenchus* are frequent and abundant with frequencies between 100% and 36% for densities varying between 7,328 and 1,360 nematodes/dm^3 of soil. According to the method of (Fortuner and Merny (1973), this group of nematodes can be capitalized as the most important on Cotton and likely to cause significant damage (Frequency >30% and Abundance <200 nematodes/dm^3 of soil). *Xiphinema, Rotylenchulus* and *Meloidogyne* are infrequent (<30%) but abundant (<200 nematodes/soil dm^3) and their presence may be associated with particular environmental conditions (soil texture, humidity, etc.). *Paratrichodorus Minor* and *Criconemella onoensis* are uncommon (<30%) and not very abundant (<200 nematodes/dm^3 of soil) and can be considered as little damage to Cotton.

3.1.3 Nematodes extracted from the roots

Pratylenchus is observed in 73% of the samples with root population densities of 30 nematodes/g of roots; This nematode is viewed to be frequent and abundant (frequency >30 and abundance >30%) and can be considered as a parasite of Cotton according to the method of (Mai and Lyon (1975). The nematodes *Scutellonema* and *Helicotylenchus* are infrequent (>30%) and scarce (<20 nematodes/g of roots). This group of nematodes is considered mainly as ectoparasites and therefore little observed in the roots.

3.1.4 Nematode community densities by cotton-growing areas and prospecting localities

The nematode samples is taken in the 3 cotton-growing areas represented by the cotton companies SOFITEX (18 sites), SOCOMA (7 sites) and Faso Coton (7 sites).

The high population densities of *Pratylenchus* is observed in the SOFITEX zone with 1,029 nematodes/dm^3 of soil with the highest densities observed on the Sarba site with 2,960 nematodes/dm^3 of soil (P<0.05). Respective population densities of 350 and 187 individuals/dm^3 of soil are observed, respectively in the SOCOMA and Faso Coton zones. The cotton-growing area of SOCOMA appears to be more infested with Helicotylenchus (1,0408 individuals/dm3 soil), *Scutellonema* (1,546/dm^3 soil), *Tylenchorhynchus* (243/dm^3 soil) and Telotylenchus (264/dm^3 soil) (P<0.05), representing, with *Pratylenchus*, the group of nematodes likely to cause significant damage to cotton. The SOFITEX zone appears to be less infested for these nematodes, compared to the Faso Coton zone, except for *Helicotylenchus,* with an average density of 7,239 individuals/dm^3 of soil. The highest population

densities of Helicotylenchus were observed at the Dedougou site with 29,600 individuals/dm³ of soil in the SOFITEX zone and at the Gongongwana/Pama site with 25,280 individuals/dm³ of soil in the Faso cotton zone. The total population densities of all parasitic nematodes observed in soil samples are higher in the SOCOMA zone, with 12,911 individuals/dm³ of soil ($P<0.05$). In the SOFITEX zone, the total soil populations are estimated at 9,583 nematodes/dm3 of soil and 6,624/dm³ of soil in the Faso Coton zone. Total populations of root-extracted nematodes are relatively low across cotton-growing areas with less than 10 nematodes/g of roots.

Table 1: Frequency and densities of nematode communities observed on cotton

Nematode genera	Frequency	Minimum	Maximum	Average	standard error
Extracted from soils	(%)	Nber N/dm³	Nber N/dm³	Nber N/dm³	Nber N/dm³
Helicotylenchus	100	40	37,040	7,328	± 781
Scutellonema	100	60	4,800	1,133	± 107
Tylenchorhynchus	75	0	7,560	464	± 117
Pratylenchus	71	0	4,940	584	± 93
Telotylenchus	36	0	1,360	121	± 27
Xiphinema	26	0	380	25	± 781
Rotylenchulus	19	0	1,460	41	± 18
Meloidogyne	13	0	200	7	± 3
Paratrichodorus	9	0	120	6	± 2
Criconemella	3	0	20	1	± 0
Extracted from roots	(%)	Nber N/g	Nber N/g	Nber N/g	Nber N/g
Pratylenchus	73	0	30	3	± 1
Scutellonema	14	0	7	1	± 0
Helicotylenchus	27	0	14	1	± 0

Legend: Nber/dm³: number of nematodes/dm³ of soil; Nber/g: number of nematodes/g of roots

Table 2: Population densities of the leading parasitic nematodes according to cotton-growing areas and sampling sites

Cotton-Zone	Location	Pray/dm³	Heli/dm³	Scute/dm³	Tyle/dm³	Telo/dm³	Tot/dm³	Tot/grac.
SOFITEX	Satiri	4,680	3,360	680	560	0	9,280	12
	Sara	1,160	10,030	650	180	0	12,070	5
	Bondokuy	1,180	3,755	1,030	55	0	6,140	7
	Ouarkoye	1,193	4,267	587	67	0	6,307	5
	Dédougou	0	29,600	800	80	0	30,560	1
	Dara	847	3,167	733	207	0	4,960	1
	Boron	700	10,640	1,180	180	0	12,940	1
	Tcheriba	900	6,040	340	340	0	7,640	2
	Bognounou	380	3,180	880	100	0	4,620	3
	Lon	1,345	4,250	915	90	25	6,675	7
	Tabou	1,090	3,390	1,273	170	203	6,243	2
	Sarba	2,960	10,920	1,720	40	280	16,600	4
	Bafor	45	6,290	1,280	170	0	7,810	4
	Klesso	1,320	3,140	420	0	120	5,160	4
	Soumousso	260	5,380	1,820	180	260	7,940	7
	Gnafogo	150	8,720	1,030	60	110	10,110	1

	Noumoudara	193	5,527	733	53	20	6,600	3
	Tapoko	120	8,640	1,860	20	0	10,840	1
Average		1,029	7,239	996	142	57	9,583	4
SOCOMA	Kouaré	749	7,832	335	886	349	10,194	7
	Niendouga	270	7,410	590	80	460	8,830	26
	Gongongwana	25	25,280	2,205	45	435	28,560	1
	Diapangou	80	17,100	1,330	260	20	18,830	4
	Dourtenga	327	1,660	1,393	147	60	3,593	2
	Tangonko	7	973	3,800	173	433	5,400	9
	Koghin	990	12,600	1,170	110	90	14,970	3
Average		350	10,408	1,546	243	264	12,911	7
Faso coton	Gonbloré V6	67	1,567	247	4,793	0	6,680	1
	Gonbloré V7	0	1,560	100	4,640	0	6,300	0
	Gnangdin	0	7,707	2,107	7	0	9,820	1
	Bittou	100	3,090	870	150	70	4,280	1
	Zekeze	900	5,967	1,740	20	0	8,647	2
	Ouadav1	200	260	3,560	0	0	4,020	1
	Kaïbo Sud	45	4835	1,085	648	8	6,620	1
Everage		187	3,569	1,387	1,465	11	6,624	1

Legend: Praty: Pratylenchus; Heli: Helicotylenchus; Scute: Scutellonema

Tyle: Tylenchorhynchus; Telo: Telotylenchus; Tot: Total in soil and roots

3.2 Discussion

The results of this study, which covered all major areas of Burkina Faso, are in line with the work of (Sawadogo et al. (1998-1999) which had identified *Helicotylenchus, Pratylenchus, Hoplolaimus, Tylenchorhynchus, Rotylenchulus* and *Meloidogyne* as the main nematodes associated with the cotton-maize-sorghum cropping system in the cotton basin of the Houndé zone in western Burkina Faso. This study did not make it possible to rule on the pathogenicity of the root-knot nematodes *Meloidogyne* spp. on cotton, unlike several studies conducted in the primary production areas of the United States and South Africa where *Meloidogyne incognita* race 3, is known to cause significant damage (Starr et al. (2005). *M. incognita* (Cophoid and white), Chitwood, and *Rotylenchulus reniformis* (Linford and Oliveira) are identified as major yield-limiting pests of upland cotton (Moore and Lawrence (2013). *M. incognita* is considered to be the nematode causing yield losses on a global scale on crop plants Wram and Zasada (2019). Our research in the main cotton-growing areas of Burkina Faso shows that the root-knot nematodes *Meloidogyne* spp. do not constitute a significant problem because they are observed at low frequencies (13%) and at average densities of 7 nematodes/dm^3 of soil. Studies on the pathovars of *Meloidogyne incognita*, recognized as the dominant species, would make it possible to decide on its pathogenicity. However, *M. acronea*, known to be a parasite on cotton and, present in South Africa and Malawi, is not present in Burkina Faso CABI (2019). The present study showed a predominance of the lesion nematode *Pratylenchus brachyurus* in the SOFITEX zone, a former cotton production area in western Burkina Faso ($P<0.05$) where cotton is generally in rotation with maize, the preferred host plant of this group of nematodes. Its abundance in this area confirms its adaptation to this culture. The lesion nematode *Pratylenchus* is known to cause significant damage to cotton and (Gay and Bird (1973) have shown that the presence of *P. brachyurus* would induce a decrease in *Meloidogyne incognita* populations. Similar competition has been observed between *Meloidogyne incognita* and *Rotylenchulus reniformis*. As for the kidney-shaped nematode *Rotylenchulus reniformis*, it is known as an important pest of cotton throughout the world mainly, in soils with a high silt/clay content (Starr et al. (2005), Gordon et al. (2022). This species may pose a

danger to cotton in Burkina Faso is where it is observed in high populations but limited to a few sites with 1,460 nematodes/dm3 of soil. The species has experienced a substantial expansion in the southern United States, causing significant damage and losses to cotton (Bridge (1992), Lawrence (2022). Several ectoparasitic nematodes is identified on Cotton, mainly in the Central, Cotton-producing states of the United States of America, but their pathogenicity has not been demonstrated. These are mostly *Helicotylenchus, Paratrichodorus minor, Tylenchorhynchus* spp. but with very low population levels (less than 100 nematodes/100cm^3 of soil or less than 10/dm^3 of soil) (Bridge (1992), Wrather et al. (1992). On the other hand, other studies have shown high densities of these groups of nematodes, which are often considered secondary but likely to cause yield losses on cotton (Singh and Mishra (2016), Schumacher et al. (2020). The high populations of the nematodes H*elicotylenchus, Scutellonema, Tylenchorhynchus* and *Telotylenchus annulatus* observed on cotton can cause significant damage to this crop under the conditions of Burkina Faso (McLean and Lawrence (2003).

IV. CONCLUSION

About ten genera of parasitic nematodes are associated with cotton in Burkina Faso, seven (7) of which are likely to cause yield losses on cotton in Burkina Faso. *Meloidogyne, Pratylenchus, Helicotylenchus, Scutellonema, Rotylenchulus, Tylenchorhynchus* and *Telotylenchus*. The nematodes *Meloidogyne* and *Rotylenchulus*, known as major cotton pests throughout the world, have been observed at low frequencies but often at high population levels, suggesting their development in particular soil and soil moisture conditions. In perspective, it will be a question of identifying the existence of races of nematodes belonging to the species *Meloidogyne javanica* and *M. incognita* by molecular characterization that can attack cotton in Burkina Faso.

Competing Interests

Authors have declared that no competing interests exist.

REFERENCES

1. AICB. 2008. Note d'information sur la filière coton du Burkina. 10p.
2. AICB. 2023a. Rapport du Burkina Faso. 81ème Assemblée Plénière du Comité Consultatif International du Coton. Mumbai, 02 au 05 décembre 2023. 8p.
3. AICB. 2023b. Campagne cotonnière 2023-2024 au Burkina Faso. Ministère de l'Industrie, du Commerce et de l'Artisanat. ttps://www.commerce.gov.bf/accueil/actualites.
4. Berimey M. A., 2012. Contrôle des nématodes et des symphyles, parasites des racines de l'ananas par l'utilisation de plantes de service. Master En Sciences – Technologies –Sante, Université Des Antilles Et De La Guyane. 30p
5. Blasingame D., Gazaway W., Goodell P., Kemerait R., Kirkpatrick T., Konning S., Lawrence G. W., McClure M., Mueller J., Newman M., Overstreet C., Phipps P., Rich J., Thomas S., Wheeler T. and Wrather A. 2002. Cotton nematodes: your hidden enemies National Cotton Council, Memphis, TN.
6. Bridge, J. 1992. Nematodes.: Cotton Diseases. R. J. Hillocks, ed. CAB International. Wallingford, UK. 331-353.
7. CABI, 2019. *Meloidogyne acronea* (African cotton root nematode). datasheet on *Meloidogyne acronea* covers Identity, Overview, Distribution, Dispersal, Hosts/Species Affected, Diagnosis, Biology & Ecology, Natural Enemies. https://www.cabidigitallibrary.org ›.
8. Doshi R. A., King R. L. and Lawrence G. W.. 2010. Classification of *Rotylenchulus reniformis* numbers in cotton using remotely sensed hyperspectral data on self-organizing maps. *Journal of Nematology* 42:179–193.

9. Forghani, F., and Hajihassani, A. 2020. Recent advances in the development of environmentally benign treatments to control root-knot nematodes. *Frontiers in Plant Science* 11:1125. doi:10.3389/fpls.2020.01125.
10. Fortuner R., Merny G., 1973. Les nématodes parasites des racines associés au riz en Basse Casamance (Sénégal) et en Gambie. *Cah. ORSTOM, Sér. Biol.*, 21: 3-20.
11. Gay, C.M. and Bird, G.W. 1973. Influence of concomitant populations of *Pratylenchus brachyurus* and *Meloidogyne incognita* on root penetration and population dynamics. *Journal of Nematology* 5,212–217.
12. Gordon, K. L., Schrimsher, D. W., and Lawrence, K. S. 2022. Additional fertilizer and nematicide combinations on upland cotton to manage *Rotylenchulus reniformis* and *Meloidogyne inco*gnita in Alabama. *Journal of Nematology* 54:1-15.
13. Lawrence K., 2022. Reniform nematode (*Rotylenchulus reniformis*) and its interactions with cotton (Gossypium hirsutum) Pp. 94-99 in R. A. Sikora, J. Desaeger, and L. Molendijk, eds. Integrated nematode management: state of-the-art and visions for the future. Oxfordshire, UK: CAB International. doi:10.1079/9781789247541.0014.
14. Mai W.F. & Lyon H.H. 1975. Pictorial Key to Genera of Plant Parasitic Nematodes. 4th edition Revised. Ithaca and London, Comstock Publishing Associates, Cornell University Press. pp219.
15. McLean, K.S. and Lawrence, G.W. 2003. Efficacy of aldicarb to *Rotylenchulus reniformis* and biodegradation in cotton field soils. *Journal of Nematology* 35, 65–72.
16. Moore S. R. and Lawrence K. S. 2012. *Rotylenchulus reniformis* in cotton: current methods of management and the future of site-specific management. *Nematropica* 42:227–236.
17. Moore S. R. and Lawrence K. S. 2013. The Effect of Soil Texture and Irrigation on *Rotylenchulus reniformis* and Cotton. *J. Nematol*, 45(2):99–105.
18. Pages S.L.J., 1983. Biolgoical studies of the African cotton root nematode, *Meloidogyne acronea*. Ph.D thesis, University of London., 294 p.
19. Sawadogo A., Dakouo D., Konaté Y. A. & Thio B. 1998-1999. Les nématodes parasites associés au système de culture coton-maïs-sorgho dans la zone de Houndé (Ouest du Burkina Faso). *Sci. et Tech., Série Sciences Naturelles*, Vol. 23, n° 2 - juillet-décembre 1998 - Janvier - juin 1999.
20. Schumacher, L.A.; Grabau, Z.J.; Wright, D.L.; Small, I.M.; and Liao, H.L. 2020. Nematicide influence on cotton yield and plant-parasitic nematodes in conventional and sod-based crop rotation. *Journal of Nematology* 52: e2020-34. DOI: 10.21307/jofnem-2020-034.
21. Seinhorst J.W., 1950. De betekenis van de grond voor het optreden van aanstasting door het stengelaaltje (*Ditylenchus dipsaci*) (Kühn Filipjev). Tijdschr. *Plantenzietkten*, 56: 289-348.
22. Seinhorst J.W., 1962. Modifications of the elutriation method for extracting nematodes from soils. *Nematologica*. 8 : 117- 28.
23. Singh A.U. and Mishra, S.D. 2016. Nematode problems in cotton crop and their management Archana. *Current Nematology*, 27 (1): 103–113.
24. Starr J.L., Carneiro R.G. et Ruano O. 2005. Nematode Parasites of Cotton and other Tropical Fibre Crops. *In* Luc M., Sikora R.A. and Bridge J., eds. *Plant Parasitic Nematodes in Subtropical and Tropical Agriculture*. Wallingford, U.K: CAB International, 733-750.
25. Taylor AL., Sasser J.N. and Nelson L.A., 1982. Relationship of climatic and soi1 characteristics to geographical distribution of nematode species in agricultural soils, Raleigh, North Carolina State University and USAID, NC., 65 p.
26. Wram, C. L., and Zasada, I. A. 2019. Shortterm effects of sublethal doses of nematicides on Meloidogyne incognita. *Phytopathology* 109:1605- 1613. doi:10.1094/phyto-11-18-0420.
27. Wrather, J. A., Niblack, T. L., and Milam, M.R. 1992. Survey of plant-parasitic nematodes in Missouri cotton fields. Suppl. *J. Nematol.* 24:779-782.